UC San Diego

UC San Diego Electronic Theses and Dissertations

Title

Composite materials with integrated embedded sensing networks

Permalink

https://escholarship.org/uc/item/0gx2j946

Author

Schaaf, Kristin Leigh

Publication Date

2008

Peer reviewed|Thesis/dissertation

eScholarship.org Powered by the California Digital Library
University of California

UNIVERSITY OF CALIFORNIA, SAN DIEGO

Composite Materials with Integrated Embedded Sensing Networks

A Dissertation submitted in partial satisfaction of the requirement for the degree

Doctor of Philosophy

in

Engineering Sciences (Mechanical Engineering)

by

Kristin Leigh Schaaf

Committee in charge:

Professor Sia Nemat-Nasser, Chair
Professor Bruce Driver
Professor Vistasp Karbhari
Professor Vlado Lubarda
Professor Marc Meyers

2008

Copyright ©

Kristin Leigh Schaaf, 2008

All rights reserved.

The Dissertation of Kristin Leigh Schaaf is approved, and it is acceptable in quality and form for publication on microfilm:

_____

_____

_____

_____

_____
Chair

University of California, San Diego

2008

DEDICATION

To my family.

To my friends.

To Brandon.

To my dog, Dakota.

EPIGRAPH

Always bear in mind
that your own resolution to succeed
is more important than any one thing.

Abraham Lincoln

TABLE OF CONTENTS

Signature Page....iii

Dedication....iv

Epigraph....v

Table of Contents....vi

List of Abbreviations....ix

List of Figures....x

List of Tables....xvi

Acknowledgement....xix

Vita....xxi

Abstract....xxiii

Chapter 1 – Introduction....1

1.1 Background....1

1.2 Motivation of research....5

1.3 Objective of research....9

1.4 Overview of dissertation....11

Chapter 2 – Materials....13

2.1 Introduction....13

2.2 Composite materials....14

2.2.1 Composite processing....22

2.2.2 Ignition loss testing....25

2.2.3 Ultrasonic testing of resin....27

2.3 Sensors....31

2.3.1 Temperature sensor.....32

2.3.2 Simulated microsensor/chip resistor.....35

2.3.3 Polyvinylidene fluoride (PVDF) sensor.....36

2.3.3.1 PVDF sensor with protective coating……..38

2.3.3.2 PVDF sensor without protective coating…….39

2.4 Summary.....40

2.5 Acknowledgement……..……...41

Chapter 3 – Quasi-static tension test.....42

3.1 Introduction.....42

3.2 Specimen preparation.....43

3.2.1 Specimen layup and fabrication.....43

3.2.2 Specimen machining.....44

3.2.3 Specimen tabbing.....44

3.2.4 Thickness and width measurements.....46

3.3 Specimen configurations.....46

3.4 Testing equipment and test configuration.....47

3.5 Experimental procedure.....48

3.6 Experimental results and discussion.....51

3.7 Summary.....63

3.8 Acknowledgement.....63

Chapter 4 – Three-point bending (short-beam shear) test.....64

4.1 Introduction.....64

4.2 Specimen preparation.....69
4.2.1 Specimen layup and fabrication.....69
4.2.2 Specimen machining.....70
4.2.3 Thickness and width measurements.....71
4.3 Specimen configurations.....71
4.4 Testing equipment and test configuration.....74
4.5 Experimental procedure.....75
4.5.1 Quasi-static three-point bending (short-beam shear) test.....75
4.5.2 Fatigue three-point bending (short-beam shear) test.....76
4.6 Experimental results and discussion.....77
4.6.1 Quasi-static three-point bending (short-beam shear) test.....77
4.6.2 Fatigue three-point bending (short-beam shear) test.....96
4.7 Summary.....114
4.8 Acknowledgement.....115
References.....116

LIST OF ABBREVIATIONS

Bryte	Bryte Technologies, Inc.
CEAM	Center of Excellence for Advanced Materials
CNC	computer numerical controlled
MEMS	microelectromechanical systems
NDE	non-destructive evaluation
PCB	printed circuit board
PEEK	polyetheretherketone
PMC	polymer matrix composites
PVC	polyvinyl choloride
PVDF	polyvinylidene fluoride
SMART Layer	Stanford Multi-Actuator-Receiver Transduction Layer
VARTM	vacuum-assisted resin transfer method

LIST OF FIGURES

Figure 1.1: Flight path of American Airlines flight 587 from takeoff to impact in relation to the flight path of Japan Airlines flight 47 overlaid on a topographical map with wake direction and wake encounter. Courtesy of the National Transportation Safety Board (2004). ……6

Figure 1.2: Failed carbon fiber and epoxy resin vertical stabilizer of American Airlines flight 587. Courtesy of the National Transportation Safety Board (2004). ……7

Figure 2.1: Schematic representation of (a) thermoplastic polymer held in place by weak secondary bonds and (b) thermosetting polymer with cross-linking. ……18

Figure 2.2: Vacuum bagging sequence for embedding sensors inside S-2-glass/epoxy prepreg composite laminate. ……23

Figure 2.3: 125 ton Wabash laminating hot press at CEAM in which S-2-glass/epoxy laminates were processed. ……24

Figure 2.4: Cure cycle for S-2-glass/BT250E-1 prepreg per Bryte Technologies, Inc. ……24

Figure 2.5: (a) Muffle furnace at CEAM utilized for ignition loss testing. (b) Crucible insertion into muffle furnace for ignition loss testing during which a specimen undergoes a rigorous heating schedule that ignites and burns the resin until only fibers remain. ……25

Figure 2.6: Location of ignition loss specimen extraction from a composite panel. The mapping of the specimen location is noted for each panel in order to ensure panel uniformity. ……26

Figure 2.7: Buchi Rotovapor R-200 used to heat BT250E-1 resin in a silicone oil bath. ……28

Figure 2.8: Temperature to achieve minimum viscosity for BT250E-1 epoxy resin and duration at minimum viscosity provided by Bryte Technologies, Inc. ……28

Figure 2.9: DS18B20X digital 1-wire thermometer from Maxim/Dallas Semiconductor shown from side view, bottom view, and top view with mechanical specifications used as the initial demonstration sensor by Nemat-Nasser et al. (2005). ……33

Figure 2.10: Photograph showing substrate with fabricated traces and land pattern (below) and with sensor attached (above). Reproduced from Nemat-Nasser et al. (2005). ……..34

Figure 2.11: Aramid/epoxy composite panel with embedded network consisting of a 10 by 10 array of individually addressable thermal sensors. A hand is placed on the panel (left) generating a thermal image (right). Reproduced from Nemat-Nasser et al. (2005). ……35

Figure 2.12: Dimensions and construction of chip resistor used as simulated microsensor. Courtesy of Koa Speer Electronics, Inc. ……36

Figure 2.13: Diagram of proposed network configuration with PVDF sensor to detect acoustic emissions. The PVDF sensor requires signal conditioning and then connects to the slave which reports to the master. Diagram courtesy of Dr. Fabrizia Ghezzo. ……..37

Figure 2.14: Photograph and diagram of FDT1-028K model PVDF thin film sensor with details of construction. Courtesy of Measurement Specialties, Inc. (2006). ……38

Figure 2.15: Photograph and construction of metallized piezo film sheet. Courtesy of Measurement Specialties, Inc. (2006). ……39

Figure 2.16: Dimensions of the piezo film and metallization on the bulk sheets of the PVDF sensors which lack the problematic screen printed acrylic protective coating. ……40

Figure 3.1: Composite laminate prepreg layup sequences for creating $[0]_2$, $[90]_{12}$, $\pm[45]_{10}$, and $[0]_4$ with simulated microsensors test specimens for the quasi-static tensile tests. ....……..……43

Figure 3.2: Specimen configurations for the quasi-static tensile tests. ……46

Figure 3.3: MTS model 312.21 load frame with hydraulic wedge grips and an 88.9 kN load cell used to conduct quasi-static tensile tests at CEAM. ……48

Figure 3.4: Plot of results from quasi-static tension tests of S-2/BT250E-1 $[0]_2$ specimens from roll one material. ……..…..52

Figure 3.5: Photographs of typical failure sequence from quasi-static tension tests of S-2/BT250E-1 $[0]_2$ specimens. ……...54

Figure 3.6: Plot of results from quasi-static tension tests of S-2/BT250E-1 $[0]_2$ specimens from roll two material. ……55

Figure 3.7: Photographs of typical failure sequence from quasi-static tension tests of S-2/BT250E-1 $[90]_{12}$ specimens. ……57

Figure 3.8: Plot of results from quasi-static tension tests of S-2/BT250E-1 $[\pm45]_{10}$ specimens from roll one material. ……...58

Figure 3.9: Photographs of typical failure sequence from quasi-static tension tests of S-2/BT250E-1 $[\pm45]_{10}$ specimens. ……...59

Figure 3.10: Plot of results from quasi-static tension tests of S-2/BT250E-1 $[\pm45]_{10}$ specimens from roll two material. ……...60

Figure 3.11: Plot of results from quasi-static tension tests of S-2/BT250E-1 $[0]_4$ specimens with one embedded simulated microsensor at the midplane. ..61

Figure 3.12: Photographs of typical failure sequence from quasi-static tension tests of S-2/BT250E-1 $[0]_4$ specimens with one embedded simulated microsensor at the midplane. ……...62

Figure 4.1: Typical three-point bending (short-beam shear) test configuration used to determine the short-beam shear strength of high-modulus fiber reinforced composite materials. ……...65

Figure 4.2: Typical failure modes observed in the three-point bending (short-beam shear) test. (a) Interlaminar shear failure. (b) Flexure failure due to compressive stresses (left) and due to tensile stresses (right). (c) Inelastic deformation. …….66

Figure 4.3: Composite panel with short-beam shear specimen layout. ……70

Figure 4.4: Typical geometry of the short-beam shear specimens investigated in the quasi-static three-point bending (short-beam shear) tests. …….72

Figure 4.5: Specimen configurations for quasi-static three-point bending (short-beam shear) tests. .....…….74

Figure 4.6: Three-point bending (short-beam shear) test fixture manufactured by Wyoming Test Fixtures, Inc. ……...75

Figure 4.7: Diagram of blank specimen with photograph of interlaminar shear failure in quasi-static three-point bending (short-beam shear) blank test specimen. …….78

Figure 4.8: Diagram of G-10 specimen with photograph of interlaminar shear failure in quasi-static three-point bending (short-beam shear) G-10 test specimen. ……..79

Figure 4.9: Diagram of embedded sensor specimen with photograph of interlaminar shear failure in quasi-static three-point bending (short-beam shear) embedded sensor test specimen. ……...80

Figure 4.10: Diagram of punched sensor specimen with photograph of interlaminar shear failure in quasi-static three-point bending (short-beam shear) punched sensor test specimen made from the second composite panel. ……..83

Figure 4.11: Diagram of PVDF protective coating midplane specimen (Ag-ink) with photograph of interlaminar shear failure in quasi-static three-point bending (short-beam shear) PVDF protective coating midplane specimen (Ag-ink). ……...84

Figure 4.12: Diagram of PVDF Ag-ink sandwich specimen with photograph of interlaminar shear failure in quasi-static three-point bending (short-beam shear) PVDF Ag-ink sandwich specimen. ……...85

Figure 4.13: Diagram of PVDF Ni-Cu sandwich specimen with photograph of interlaminar shear failure in quasi-static three-point bending (short-beam shear) PVDF Ni-Cu sandwich specimen. ……86

Figure 4.14: Diagram of PVDF Ag-ink midplane specimen with photograph of interlaminar shear failure in quasi-static three-point bending (short-beam shear) PVDF Ag-ink midplane specimen. ……...87

Figure 4.15: Diagram of PVDF Ni-Cu midplane specimen with photograph of interlaminar shear failure in quasi-static three-point bending (short-beam shear) PVDF Ni-Cu midplane specimen. ……88

Figure 4.16: Diagram of PVDF Ag-ink representative area midplane specimen with photograph of interlaminar shear failure in quasi-static three-point bending (short-beam shear) PVDF Ag-ink representative area midplane specimen. ……..89

Figure 4.17: Diagram of PVDF Ni-Cu representative area midplane specimen with photograph of interlaminar shear failure in quasi-static three-point bending (short-beam shear) PVDF Ni-Cu representative area midplane specimen. ……..90

Figure 4.18: Summary of quasi-static three-point bending (short-beam shear) test results for the various specimen configurations. ……...93

Figure 4.19: Typical interlaminar failure of blank specimen subjected to fatigue three-point bending (short-beam shear) loading. ……....97

Figure 4.20: Fatigue three-point bending (short-beam shear) results for blank specimens. ……..97

Figure 4.21: Typical interlaminar failure of G-10 specimen subjected to fatigue three-point bending (short-beam shear) loading. ……....98

Figure 4.22: Fatigue three-point bending (short-beam shear) results for G-10 specimens. ……..98

Figure 4.23: Typical interlaminar failure of embedded sensor specimen subjected to fatigue three-point bending (short-beam shear) loading. ……....99

Figure 4.24: Fatigue three-point bending (short-beam shear) results for embedded sensor specimens. ……...99

Figure 4.25: Typical interlaminar failure of punched sensor specimen subjected to fatigue three-point bending (short-beam shear) loading. ……...100

Figure 4.26: Fatigue three-point bending (short-beam shear) results for punched sensor specimens. …….100

Figure 4.27: Typical interlaminar failure of PVDF Ag-ink protective coating midplane specimen subjected to fatigue three-point bending (short-beam shear) loading. ……101

Figure 4.28: Fatigue three-point bending (short-beam shear) results for PVDF Ag-ink protective coating midplane specimens. ……...101

Figure 4.29: Typical interlaminar failure of PVDF Ag-ink sandwich specimen subjected to fatigue three-point bending (short-beam shear) loading. ……...102

Figure 4.30: Fatigue three-point bending (short-beam shear) results for PVDF Ag-ink sandwich specimens. ……102

Figure 4.31: Typical interlaminar failure of PVDF Ni-Cu sandwich specimen subjected to fatigue three-point bending (short-beam shear) loading. ……...103

Figure 4.32: Fatigue three-point bending (short-beam shear) results for PVDF Ni-Cu sandwich specimens. …….103

Figure 4.33: Typical interlaminar failure of PVDF Ag-ink midplane specimen subjected to fatigue three-point bending (short-beam shear) loading. ….....104

Figure 4.34: Fatigue three-point bending (short-beam shear) results for PVDF Ag-ink midplane specimens. ……104

Figure 4.35: Typical interlaminar failure of PVDF Ni-Cu midplane specimen subjected to fatigue three-point bending (short-beam shear) loading. ……...105

Figure 4.36: Fatigue three-point bending (short-beam shear) results for PVDF Ni-Cu midplane specimens. ……..105

Figure 4.37: Typical interlaminar failure of PVDF Ag-ink representative area midplane specimen subjected to fatigue three-point bending (short-beam shear) loading. ……106

Figure 4.38: Fatigue three-point bending (short-beam shear) results for PVDF Ag-ink representative area midplane specimens. ……...106

Figure 4.39: Typical interlaminar failure of PVDF Ni-Cu representative area midplane specimen subjected to fatigue three-point bending (short-beam shear) loading. ……107

Figure 4.40: Fatigue three-point bending (short-beam shear) results for PVDF Ni-Cu representative area midplane specimens. ……...107

Figure 4.41: Resin pockets in three-point bending (short-beam shear) embedded sensor test specimen. 111

Figure 4.42: Resin pockets surrounding rectangular simulated microsensor. 111

Figure 4.43: (a) Micrograph (125X) of blank specimen. (b) Micrograph (125X) of embedded sensor specimen. (c) Micrograph (125X) of embedded sensor specimen with resin pockets highlighted in red, voids highlighted in black, and sensors highlighted in gold. (d) Micrograph (125X) of punched sensor specimen. (e) Micrograph (125X) of punched sensor specimen with resin pockets highlighted in red, voids highlighted in black, and sensors highlighted in gold. 112

LIST OF TABLES

Table 2.1: Typical mechanical properties of common fibers used in polymer matrix composites compared to monolithic materials. Reproduced from Kaw (2006). ……15

Table 2.2: Comparison of the properties of the most prevalent commercially available glass fibers in use; E-glass and S-glass. Reproduced from Kaw (2006). ……16

Table 2.3: Chemical composition of E-glass and S-glass fibers (in weight percent). Reproduced from Kaw (2006). ……17

Table 2.4: Characteristics, advantages, and disadvantages of thermosets and thermoplastics. ……19

Table 2.5: Typical properties of cast epoxy resin at ambient conditions. ……20

Table 2.6: Typical neat resin properties of BT250E-1 epoxy resin as supplied by Bryte Technologies, Inc. ……..22

Table 2.7: Dimensions of 2A or 0805 chip resistor used as simulated microsensor. Courtesy of Koa Speer Electronics, Inc. ……..36

Table 2.8: Dimensions of FDT1-028K model PVDF thin film sensor depicted in Figure 2.14. ……..39

Table 3.1: Typical mechanical properties of Techkits A-12 rigid bond epoxy adhesive at ambient laboratory conditions. ……..45

Table 3.2: Results from quasi-static tension tests of S-2/BT250E-1 $[0]_2$ specimens from roll one material. ……52

Table 3.3: Typical mechanical properties of S-2-glass/BT250E-1 epoxy prepreg with a resin content of 33 ±3% as provided by Bryte Technologies, Inc. …...53

Table 3.4: Results from quasi-static tension tests of S-2/BT250E-1 $[0]_2$ specimens from roll two material. ……54

Table 3.5: Results from quasi-static tension tests of S-2/BT250E-1 $[90]_{12}$ specimens from roll one material. ……56

Table 3.6: Results from quasi-static tension tests of S-2/BT250E-1 $[90]_{12}$ specimens from roll two material. ……56

Table 3.7: Results from quasi-static tension tests of S-2/BT250E-1 $[\pm 45]_{10}$ specimens from roll one material. ……58

Table 3.8: Results from quasi-static tension tests of S-2/BT250E-1 $[\pm 45]_{10}$ specimens from roll two material. ……59

Table 3.9: Results from quasi-static tension tests of S-2/BT250E-1 $[0]_4$ specimens with one embedded simulated microsensor at the midplane. …….61

Table 4.1: Quasi-static three-point bending (short-beam shear) test results for blank specimens from a composite panel with an average fiber volume fraction of 51.23%. ……..…78

Table 4.2: Quasi-static three-point bending (short-beam shear) test results for G-10 specimens from a composite panel with an average fiber volume fraction of 51.23%. ……..79

Table 4.3: Quasi-static three-point bending (short-beam shear) test results for embedded sensor specimens from a composite panel with an average fiber volume fraction of 51.23%. ……80

Table 4.4: Quasi-static three-point bending (short-beam shear) test results for blank specimens from the second composite panel with an average fiber volume fraction of 54.04%. ……81

Table 4.5: Quasi-static three-point bending (short-beam shear) test results for embedded sensor specimens from the second composite panel with an average fiber volume fraction of 54.04%. ……...82

Table 4.6: Quasi-static three-point bending (short-beam shear) test results for punched sensor specimens from the second composite panel with an average fiber volume fraction of 54.04%. ……...82

Table 4.7: Quasi-static three-point bending (short-beam shear) test results for PVDF protective coating midplane specimens (Ag-ink) containing the active sensor segment from the composite panel with an average fiber volume fraction of 53.19%. ……84

Table 4.8: Quasi-static three-point bending (short-beam shear) test results for PVDF protective coating midplane specimens (Ag-ink) containing the traces segment from the composite panel with an average fiber volume fraction of 53.19%. ……..84

Table 4.9: Quasi-static three-point bending (short-beam shear) test results for PVDF Ag-ink sandwich specimens from the composite panel with an average fiber volume fraction of 53.11%. ……...85

Table 4.10: Quasi-static three-point bending (short-beam shear) test results for PVDF Ni-Cu sandwich specimens from the composite panel with an average fiber volume fraction of 53.11%. ……...86

Table 4.11: Quasi-static three-point bending (short-beam shear) test results for PVDF Ag-ink midplane specimens from the composite panel with an average fiber volume fraction of 53.11%. ……...87

Table 4.12: Quasi-static three-point bending (short-beam shear) test results for PVDF Ni-Cu midplane specimens from the composite panel with an average fiber volume fraction of 53.11%. ……...88

Table 4.13: Quasi-static three-point bending (short-beam shear) test results for PVDF Ag-ink representative area midplane specimens from the composite panel with an average fiber volume fraction of 49.05%. ……89

Table 4.14: Quasi-static three-point bending (short-beam shear) test results for PVDF Ni-Cu representative area midplane specimens from the composite panel with an average fiber volume fraction of 49.05%. ……....90

Table 4.15: Summary of fatigue three-point bending (short-beam shear) test results including average fatigue life and normalized fatigue life. 108

Table 4.16: Effect of the shear stress concentration factor on the fatigue life. 109

ACKNOWLEDGEMENT

I would like to express my sincere appreciation to the many people who contributed to this work.

First of all, I would like to thank my advisor, Professor Sia Nemat-Nasser, not only for his guidance, but also for allowing me to pursue the path of my choosing and enthusiastically supporting my interests in outreach and education. I would also like to thank the other faculty members who have served on my dissertation committee; Professors Bruce Driver, Vistasp Karbhari, Vlado Lubarda, and Marc Meyers. I am particularly indebted to Professor Vlado Lubarda who endlessly employed me as his teaching assistant and served as an ideal mentor. I would also like to thank Professor Marc Meyers for going to great lengths to accommodate me.

At the Center of Excellence for Advanced Materials (CEAM), I could not have achieved much if it was not for the efforts and teamwork of Dr. Fabrizia Ghezzo, Mr. Yi Huang, and Mr. Patrick Rye. I owe a great many thanks to Mr. Jon Isaacs, Mr. Ben Cook, Mr. Dirk Vanulden, and Mrs. Lauri Jacobs-Cohantz who went to extraordinary efforts to assist me every time I looked for help and always made any problem I had their number one priority. I am also grateful to my other colleagues at CEAM including Dr. Alireza Amirkhizi, Dr. Thomas Plaisted, Dr. Mahmoud Amini, Mr. Christian Nielsen, and Mr. Yan Gao for making my work environment such an enjoyable one.

The University of California, San Diego Campus Research Machine Shop has been integral in machining the samples utilized in this research. In particular, I would especially like to thank Mr. Gary Foreman for his hard work.

Finally, I would like to acknowledge that this work was supported by the National Science Foundation CMS grant number 0330450 under the Program Director of Sensor Innovation and Systems, Dr. Shih-Chi Liu. I would like to thank Dr. Shih-Chi Liu for encouraging and supporting my participation in international conferences and workshops and exposing me to state of the art research around the world. He has always offered to assist me in any way possible, and even more notably, he has always followed through on his offer.

VITA

2003	Bachelor of Science in Mechanical Engineering, Tulane University, New Orleans, Louisiana
2005	Master of Science in Engineering Sciences, Mechanical Engineering, University of California, San Diego
2008	Doctor of Philosophy in Engineering Sciences, Mechanical Engineering, University of California, San Diego

PUBLICATIONS

PROCEEDINGS

Schaaf, K., P. Rye and S. Nemat-Nasser. 2007. Optimization of Sensor Introduction into Laminated Composites. *Proceedings of 2007 SEM Annual Conference and Exposition on Experimental and Applied Mechanics*.

Rye, P.M., Y. Huang, F. Ghezzo, K. Schaaf, and S. Nemat-Nasser. 2007. Distributed Sensing, Damage Detection, and Analysis in FRP Unidirectional Composites. *Proceedings of the 2007 SEM Annual Conf. & Expo. on Experimental & Applied Mechanics*.

Schaaf, K., P. Rye and S. Nemat-Nasser. 2007. Optimization Studies of Self-sensing Composites. *Proceedings of Sensors and Smart Structures Technologies for Civil, Mechanical, and Aerospace Systems*, *SPIE's 14th Annual International Conference on Smart Structures and Materials* **6529**: 65292X1-65292X5.

Rye, P., K. Schaaf, A. Starr, and S. Nemat-Nasser. 2006. Self-Sensing Composites. *Proceedings of the 2006 SEM Annual Conf. & Expo. on Experimental & Applied Mechanics*.

Schaaf, K., P. Rye, F. Ghezzo, A. Starr, and S. Nemat-Nasser. 2006. Optimization of the mechanical properties of composite materials with integrated embedded sensor networks. *Proceedings of Smart Structures and Materials 2006: Sensors and Smart Structures Technologies for Civil, Mechanical, and Aerospace Systems, SPIE's 13th Annual International Conference on Smart Structures and Materials* **6174**: 617443–1–617443-5.

Schaaf, K., B. Cook, F. Ghezzo, Y. Huang, P. Rye, J. Aller, K. Loewke, A. Starr, and S. Nemat-Nasser. 2005. Composite Materials with Integrated Embedded Sensor Networks. *Proceedings of the Second International Workshop on Advanced Smart Materials and Smart Structures Technology*, (ed.) C. Yun and B. F. Spencer. Techno Press, 79–88.

Rye, P., A. Starr, K. Schaaf, and S. Nemat-Nasser. 2005. Integration of Electronic Sensing in Composite Materials for Structural Health Monitoring. *Proceedings of the Fifth International Workshop on Structural Health Monitoring: Advancements and Challenges for Implementation*, 756–761.

Huang, Y., K. Loewke, K. Schaaf, and S. Nemat-Nasser. 2005. Localized SHM with Embedded Sensor Network. *Proceedings of the Fifth International Workshop on Structural Health Monitoring: Advancements and Challenges for Implementation*, 1554-1561.

Schaaf, K., B. Cook, F. Ghezzo, A. Starr, and S. Nemat-Nasser. 2005. Mechanical Properties of Composite Materials with Integrated Embedded Sensor Networks. *Proceedings of Smart Structures/NDE Joint Conference: Sensors and Smart Structures Technologies for Civil, Mechanical and Aerospace Systems*, *SPIE's 12th Annual International Conference on Smart Structures and Materials* **5765**: 781–785.

ABSTRACTS

Schaaf K., F. Ghezzo, A. Starr, and S. Nemat-Nasser. 2006. Characterization of composite materials with embedded sensors. *Proceedings of the 2006 SEM Annual Conf. & Expo. on Experimental & Applied Mechanics*.

FIELDS OF STUDY

Major Field: Engineering Sciences (Mechanical Engineering)

Studies in Mechanical Behavior of Materials
Professor Sia Nemat-Nasser

ABSTRACT OF THE DISSERTATION

Composite Materials with Integrated Embedded Sensing Networks

by

Kristin Leigh Schaaf

Doctor of Philosophy in Engineering Sciences (Mechanical Engineering)

University of California, San Diego, 2008

Professor Sia Nemat-Nasser, Chair

The increasing demand for in-service structural health monitoring has stimulated efforts to integrate self and environmental sensing capabilities into materials and structures. The present work is directed towards the development of a new means of fabricating composites that allows for integrating a high density of

small, advanced sensors into a laminated composite in a way that enables sensing without compromising the structural integrity of the host composite material.

This work presents efforts to develop structural composite materials which include networks of embedded sensors with decision-making capabilities that extend the functionality of the composite materials to be information-aware. These structurally-integrated embedded microsensors render the composite information-based, so that it can monitor and report on the local structural environment, on request or in real-time as necessary.

The integration of sensors, actuators, and their subsequent devices into a structure is vital in smart applications. Essential to the application of smart composites is the issue of the mechanical coupling of the sensor to the host composite material. Therefore, the question of the impact of such devices on the various mechanical properties of the host composite material is both relevant and important. This work characterizes the effects of introducing simulated microsensors, commonly used printed circuit board material (G-10/FR4 Garolite), and various piezo thin film sensors on the mechanical properties of the host structural composite material.

Quasi-static tension tests are conducted in order to characterize the mechanical properties of the host composite material as well as the effects the embedments have upon the host material. Quasi-static three-point bending (short-beam shear) and fatigue three-point bending (short-beam shear) tests are conducted in order to

characterize the effects of introducing the sensors and such devices on the short-beam shear strength and fatigue life of the host structural composite material. Furthermore, various embedding configurations are examined.

The thrust of the research presented here is to characterize the effects of embedding sensors and their subsequent devices on the mechanical properties of the host structural composite material in order to select a sensor and embedding configuration that can seamlessly be integrated into the host composite without compromising the integrity of the structure.

Chapter 1

Introduction

1.1 Background

In smart applications, it is essential to integrate sensors, actuators, and their subsequent devices into a structure. The primary modes of integration include surface mounting and embedding within the host structural material. Surface mounted components would offer ease of access and maintenance; however, in many applications surface mounting is not feasible due to the operating environment and system requirements. Often embedding is the only realistic way to introduce a sensor to the host structure. Embedding the sensors allows for protection from adverse environmental conditions and creates an autonomous structure. The integration of sensing into materials and structures offers significant advantages. By assimilating multiple needed properties into a single material or structure, a system that better meets the demands of its mission and operating environment can be achieved.

A number of previous efforts have sought to incorporate novel non-structural elements into composite systems to create an intelligent structure. Crawley and de Luis (1987) conducted an experimental investigation of glass/epoxy laminates with

embedded piezoceramics and showed that the ultimate strength of the tensile test coupons was reduced by 20%. Warkentin and Crawley (1991) studied the feasibility of embedding integrated circuits on silicon chips into graphite/epoxy composite laminates and investigated the effects of the embedment under static mechanical loading. Their work concluded that the presence of the device in a standard cure composite laminate had no effect on the longitudinal elastic modulus but did result in a 15% decrease in the ultimate stress. Kim et al. (1992) demonstrated that embedding thermocouples or simulated strain gauges (Kapton film) in both graphite/epoxy and graphite/polyetheretherketone (PEEK) composite laminates had little effect on the in-plane compressive and bending strengths regardless of whether the composite matrix was thermosetting or thermoplastic and whether the layup was unidirectional, cross-ply, or quasi-isotropic. In Sweden Paget and Levin (1999) studied the effect of embedded piezoelectric ceramic transducers on the structural integrity of carbon/epoxy laminates under static tensile and compressive loading. It was found that the embedded piezoelectric ceramic element along with its subsequent interconnectors did not reduce the strength of the host composite material. In both loading scenarios, the final failure did not coincide with the location of the embedded piezoelectric ceramic transducer within the laminate.

Shukla and Vizzini (1996) developed a structural tailoring technique known as interlacing in graphite/epoxy laminates. Through the use of interlacing it was shown that under quasi-static uniaxial tension the ultimate strength of the structure was substantially increased by distributing the discontinuity of the inclusion throughout the

thickness of the specimen, and the onset of damage at and near the inclusion was delayed.

Experimental work by Mall and Coleman (1998) investigated the effects of embedding piezoelectric sensors on the tensile strength and tension-tension fatigue behavior of graphite/epoxy laminates. The monotonic tensile tests yielded ultimate strength and Young's modulus results for laminates with and without sensors that were within 4% of one another. The fatigue lives with and without the embedded sensors were also close to one another, with the range of modulus reduction within 5 to 15% of each other. The work of Hansen and Vizzini (2000) focused on the tension-tension fatigue response of a host structure with interlaced embedded devices in graphite/epoxy laminates. Their results once again demonstrated that the onset of damage can be delayed and the progression of delamination impeded by distributing the material discontinuity of the inclusion throughout the thickness of the specimen in the form of interlacing.

Sirkis et al. (1992) presented important experimental observations regarding laminated graphite/epoxy composites with embedded optical fiber sensors and piezoceramics actuators. It was observed that on the macroscale the damage reduced the stiffness and strength of the host material. On the microscale the damage actually affected the function of the sensors and actuators by altering the strain or force transfer. Thus, the structural integrity of the host material was influenced.

The work of Chow and Graves (1992) investigated the three-dimensional stress and displacement fields around a rectangular embedment in a graphite/epoxy laminate. Their results indicated that the interlaminar stresses due to the embedment were nearly five times as high as the magnitude of the stress corresponding to the applied far-field load. Singh and Vizzini (1993) analytically demonstrated that it is merely the presence of the inclusion that dictates the structural integrity of the host, virtually independent of whether or not the inclusion is active.

In 2000 Varadan and Varadan addressed some of the relevant issues pertaining to the incorporation of non-structural elements into fiber reinforced composites by focusing on the design and fabrication of microelectromechanical systems (MEMS) devices and their use in engineering applications. Lin and Chang (2002) developed a manufacturing method for integrating a network of piezoceramic actuators/sensors into carbon/epoxy laminated composite structures. The method utilizes the printed circuit technique to fabricate a thin flexible layer with a network of piezoceramics referred to as the Stanford Multi-Actuator-Receiver Transduction Layer (SMART Layer). The SMART Layer can be integrated into a composite laminate via insertion between ply layers or by bonding onto the surface. In terms of quasi-static testing, tests demonstrated that the SMART Layer did not degrade the structural integrity of the host composite laminate.

For a brief overview of efforts to create materials which can respond to environmental inputs in an intelligent manner see the recent review paper on the subject of structural health monitoring by Mal (2004).

1.2 Motivation of research

A composite is an artificially constructed material system consisting of multiple components designed to attain specific properties superior to those of the individual constituents. Composites have unique advantages over monolithic materials including high strength, high stiffness, long fatigue life, low density, and adaptability to the intended function of the structure (Daniel, 1993). Because of these properties, composite materials lend themselves to a wide range of applications across numerous industries including transportation, construction, corrosion resistance, marine, and electrical and electronics.

There is a trend of increased use of composites as confirmed by Boeing. The Boeing 747, developed in the 1960s, had only one percent composites. That increased slightly to three percent with the Boeing 757 and 767 planes of the 1980s and to eleven percent on the 777 of the early 1990s. The 787 Dreamliner, which has yet to fly, has fully half of its airframe materials using composites (Wallace, 2008).

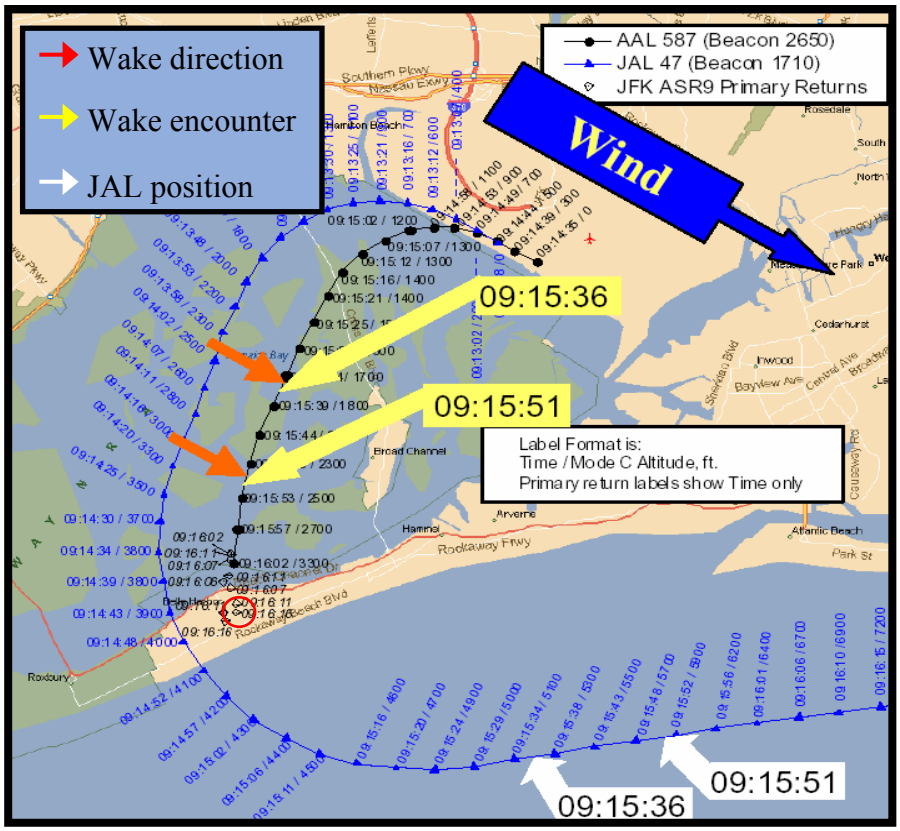

Figure 1.1: Flight path of American Airlines flight 587 from takeoff to impact in relation to the flight path of Japan Airlines flight 47 overlaid on a topographical map with wake direction and wake encounter. Courtesy of the National Transportation Safety Board (2004).

In so many of the applications, failure of the composite in service can be critical. This was clearly evident with the American Airlines flight 587 disaster. This flight departed JFK airport in New York bound for Santo Domingo in the Dominican Republic. The Airbus A300, which took off just minutes after a Japan Airlines Boeing 747 on the same runway, flew into the larger jet's wake, an area of very turbulent air; see Figure 1.1. The co-pilot attempted to keep the plane upright with the rudder. The strength of the air flowing against the moving rudder stressed the vertical stabilizer of the aircraft and eventually snapped it off entirely, causing the aircraft to lose control

and crash, resulting in the loss of 265 lives. The failed carbon fiber vertical stabilizer can be seen in Figure 1.2.

Figure 1.2: Failed carbon fiber and epoxy resin vertical stabilizer of American Airlines flight 587. Courtesy of the National Transportation Safety Board (2004).

Thus, there is a need to rapidly assess the structural health or integrity of a composite; however, detection of incipient damage is usually difficult. Expensive equipment and specialist operators are often required to perform non-destructive evaluation (NDE) techniques, such as X-ray or c-scan. These inspections require that the structure be taken out of service. In many cases the area of the composite needing inspection is inaccessible to presently available NDE interrogation methods, such as in chemical containers or the interior portions of structures. For other applications such as satellites, inspection is simply impossible (Lin and Chang, 2002).

More importantly, the inspection takes place *after* the damage has already occurred, leaving the inspection process to look for residual signs of the overload or failure condition. In order to compensate for these difficulties, design engineers frequently resort to over designing, building in redundancy, or avoiding the use of composites altogether; thus leading to inefficient solutions.

This work seeks to add properties to the composite itself that are *information-based* without compromising the structural integrity of the host composite material. This information takes the form of structurally integrated microsensors that can monitor and report on the local structural environment on request or in real-time as necessary. The envisioned sensors could read such structural health related parameters as temperature, load, strain, acceleration, or acoustic emissions.

This increased knowledge of the structure, based on *actual* data rather than statistical assumptions and extrapolations, will allow for greater flexibility in composite design. The development of a reliable means of ascertaining the status of the composite structure will allow for more high performance designs while minimizing over designing and building in redundancy.

"The problem of embedding electronic components in structural materials involves both the concerns of the structural engineer interested in ensuring mechanical performance in the presence of inclusions, and those of the electrical engineer regarding the mechanical, electrical, and chemical effects of the surrounding structure

on the electronic devices," as noted by Warkentin and Crawley (1991). This work addresses the principal concern that the embedded sensors and subsequent devices act as inclusions and have the potential to degrade the structural integrity of the host composite material. These inclusions function as discontinuities in transferring stress within the material, leading to matrix cracking, debonding, delamination, and ultimately the mechanical failure of such materials. Previous efforts to integrate sensors and MEMS devices into fiber-reinforced composites have often required that such a device be placed between the fiber layers of a composite as it is being fabricated. As a result, the device is usually surrounded by the matrix phase, typically a polymer, which is generally the weaker phase within the composite. This weak region surrounding the sensor becomes a highly probable region for failure. Additionally, device failure can be caused by the presence of high stresses in the device as a result of poor laminate design or defects resulting from the manufacture process. Therefore, it is necessary to characterize the effects of embedding sensors and their subsequent devices on the mechanical properties of the host structural composite material.

1.3 Objective of research

The primary goal of this research is to ultimately extend the functionality of the composite material beyond that of simply load-bearing. This work seeks to enable *in situ* sensing, without compromising the structural integrity of the host composite material. The thrust of the research presented here is to characterize the effects of embedding sensors and their subsequent devices on the mechanical properties of the

host structural composite material in order to select a sensor and embedding configuration that can seamlessly be integrated into the host composite without compromising the integrity of the structure.

Aspects of the research include:

- Characterizing the virgin composite material in terms of ultimate tensile strength, Young's modulus, ultimate transverse tensile strength, transverse Young's modulus, and maximum in-plane shear strength
- Investigating the effect of the embedment on the strength of the host composite material and the failure mechanism under quasi-static tensile loading
- Characterizing the short beam shear strength of the virgin composite material
- Investigating the effect of the various embedments on the short-beam shear strength and failure mechanism
- Investigating the effect of the various embedding configurations on the short-beam shear strength and failure mechanism
- Characterizing the three-point bending (short-beam shear) fatigue life of the virgin composite material
- Investigating the effect of the various embedments on the three-point bending (short-beam shear) fatigue behavior and the failure mechanism

- Investigating the effect of the various embedding configurations on the three-point bending (short-beam shear) fatigue behavior and failure mechanism

Based upon these studies, an optimum sensor and embedding configuration are suggested such that the structural integrity of the host composite material is not compromised.

1.4 Overview of dissertation

Most of the chapters presented in this dissertation are designed to be stand-alone entities. Therefore, some of the fundamentals are repeated for the sake of independence. The remainder of the dissertation is organized as follows:

- Chapter 2 discusses the material selections for this research. The rationale for utilizing S-2-glass/epoxy composites is discussed. The method of composite fabrication is detailed along with the means of quality assurance measurements in the form of ignition loss testing. The range of sensors and simulated sensors investigated in this work is also presented along with the motivation for their use.
- Chapter 3 focuses on the quasi-static tensile tests. Characterization tests are conducted on the virgin composite material to determine the mechanical properties and failure mechanisms. Subsequent characterization tests are performed on samples containing simulated microsensors in order to ascertain

the effect the embedment has on the mechanical properties and failure mechanisms.

- Chapter 4 presents the three-point bending (short-beam shear) tests. The quasi-static tests are conducted in order to characterize the short-beam shear strength of the virgin composite material and the effect of the various embedments and embedding configurations on the mechanical properties and failure mechanisms. The short-beam shear strength results provide necessary baseline information for the fatigue three-point bending (short-beam shear) tests. Fatigue three-point bending (short-beam shear) tests, which more accurately represent potential in-service loading conditions, are conducted in order to characterize the fatigue behavior of the composite material in virgin form and with the various embedments and embedding configurations under three-point bending (short-beam shear) loading conditions. To understand the mechanical response, the microstructure is analyzed using a metallograph.

Chapter 2

Materials

2.1 Introduction

Compatibility and survivability are relevant issues when considering integrating sensors, actuators, and their subsequent devices into composite materials. Silicon based electronic devices typically have a temperature limit ranging from 220 to 235 degrees Celsius, beyond which damage to the device can occur (McFarland, 2006). The temperature range for piezoelectric thin films is more conservative, with the temperature limit ranging from merely 100 to 135 degrees Celsius (Measurement Specialties, Inc., 2006). Therefore, the thermal processing of the composite must not exceed these limits or the sensing elements may be damaged. The selection of the polymer matrix is an important consideration in designing the composite, as it needs to be cured and solidified below the indicated limiting temperatures. Thermosetting polymers, such as conventional epoxies and polyesters, are well suited for such applications. The temperature restriction does not limit the selection of the fiber phase of the composite. Rather, the fiber type, be it aramid, carbon, or glass, will be selected for optimal mechanical properties, compatibility with the matrix phase, and such that

it does not interfere with the sensing and signal processing of the functioning composite.

2.2 Composite materials

Fiber reinforced composite materials consist of a fiber reinforcing phase embedded in a matrix phase. In general, the fibers are the principal load-bearing members. The matrix phase serves several functions, including keeping the fibers in the desired location and orientation, transferring load between fibers, and protecting the fibers from adverse environmental conditions (Mallick, 1993).

Elements of low atomic number, namely carbon, boron, aluminum, and silicon, can be utilized to create stiff, low density materials due to their strong directional interatomic bonds. The materials can be made solely of the elements themselves, from their compounds, or from the elements in combination with oxygen or nitrogen (Baker et al., 2004). Plastic flow is inhibited by the strong interatomic bonds. When these materials are unable to relieve stress concentrations through plastic flow, they are weakened by submicroscopic flaws, particularly on the surface (Kelly, 1986). Therefore, it is only in the fiber form that these materials exhibit their inherent high strength (Chawla, 1987). This is because the probability per unit length of a flaw being present is inversely related to the volume of the material. Thus a fiber with very low volume per unit length is on average much stronger than the bulk material. Aramid, carbon, and glass fibers are the principal fibers in commercial use. The

typical mechanical properties of these fibers compared with traditional monolithic metals of steel and aluminum are given in Table 2.1

Table 2.1: Typical mechanical properties of common fibers used in polymer matrix composites compared to monolithic materials. Reproduced from Kaw (2006).

Property	Units	Carbon	Aramid	Glass	Steel	Aluminum
Specific gravity	-	1.8	1.4	2.5	7.8	2.6
Young's modulus	GPa	230.0	124.0	85.0	206.8	69.0
Ultimate tensile strength	MPa	2067.0	1379.0	1550.0	648.1	275.8
Axial coefficient of thermal expansion	μm/m/°C	-1.3	-5.0	5.0	11.7	23.0

Aramid fibers are organic compounds composed of carbon, hydrogen, oxygen, and nitrogen. They are advantageous due to their low density, high tensile strength, relatively low cost, and high impact resistance (Kaw, 2006). A major advantage is their ability to absorb a large amount of energy during fracture; hence, they are commonly used for ballistic protection. Some of the drawbacks include low compressive properties, a high tendency to absorb moisture, and degradation in strength due to prolonged exposure to ultraviolet radiation (Baker et al., 2004).

Carbon fibers are made from organic precursor materials by a process of carbonization. Carbon fibers are advantageous due to their exceptionally high tensile strength to weight ratios, high tensile modulus to weight ratios, low coefficient of linear thermal expansion, and high fatigue strengths. Their drawbacks include low impact resistance, high electrical conductivity, and high cost (Mallick, 1993). While

the terms carbon and graphite are often used interchangeably for these fibers, they are different. Carbon fibers contain 93 to 95% carbon, while graphite contains more than 99% carbon (Schwartz, 1984).

Glass fibers are the most commonly used fibers in polymer matrix composites (PMC) largely due to their high tensile strength, low cost, high chemical resistance, and good insulating properties. Their disadvantages include low tensile modulus, high specific gravity, sensitivity to abrasion, and relatively low fatigue strength.

While there are numerous types of glass fibers commercially available, the mainstays include E-glass and S-glass. E-glass was designed for electrical applications and has the lowest cost. S-glass is used primarily for more structurally demanding applications, such as those in the aerospace industry. S-glass retains its strength at significantly higher temperatures and also has higher fatigue strength when compared to E-glass. The typical mechanical properties of the two fiber types are compared in Table 2.2.

Table 2.2: Comparison of the properties of the most prevalent commercially available glass fibers in use; E-glass and S-glass. Reproduced from Kaw (2006).

Property	Units	E-Glass	S-Glass
Specific gravity	-	2.54	2.49
Young's modulus	GPa	72.40	85.50
Ultimate tensile strength	MPa	3447.00	4585.00
Coefficient of thermal expansion	μm/m/˚C	5.04	5.58

The variation in the properties can be attributed to the differences in composition; see Table 2.3. The compositional difference combined with a higher manufacturing cost make S-glass a more expensive fiber. S-2-glass, a lower cost version of S-glass has been developed. S-2-glass is made to less stringent nonmilitary specifications but maintains a tensile strength and modulus similar to that of S-glass (Mallick, 1993).

Table 2.3: Chemical composition of E-glass and S-glass fibers (in weight percent). Reproduced from Kaw (2006).

	% Weight	
Material	**E-glass**	**S-glass**
Silicon oxide	54.00	64.00
Aluminum oxide	15.00	25.00
Calcium oxide	17.00	0.01
Magnesium oxide	4.50	10.00
Boron oxide	8.00	0.01
Others	1.50	0.80

As mentioned previously, the matrix phase of the composite serves multiple functions. The matrix transfers stresses between fibers, provides a barrier for the fibers from adverse environmental conditions, and protects the fiber surface from mechanical abrasion. While the matrix plays a minor role in the longitudinal tensile load-carrying capability of a composite structure, the matrix significantly affects the *matrix-dominated properties* including the longitudinal compression strength, the transverse tensile strength, the interlaminar shear strength, and in-plane shear strength. The interaction between the fibers and the matrix is important in designing damage-

tolerant structures. The physical and thermal characteristics of the matrix heavily influence the ability to process a composite as well as the defects in a composite structure.

Matrix materials include polymers, metals, and ceramics, with polymers being the most prevalent in advanced composites. Polymers can be divided into two broad categories: thermoplastics and thermosets. The molecules in a thermoplastic polymer are linear in structure and lack chemical linking between them; see Figure 2.1(a). Instead they are held in place by weak secondary bonds, and when heat and pressure are applied these intermolecular bonds can be temporarily broken. When these bonds are broken, the molecules can move relative to one another. Once cooled, the molecules restore the secondary bonds and form a new shape. Quite simply, a thermoplastic can be heat softened, melted, and reshaped as often as desired.

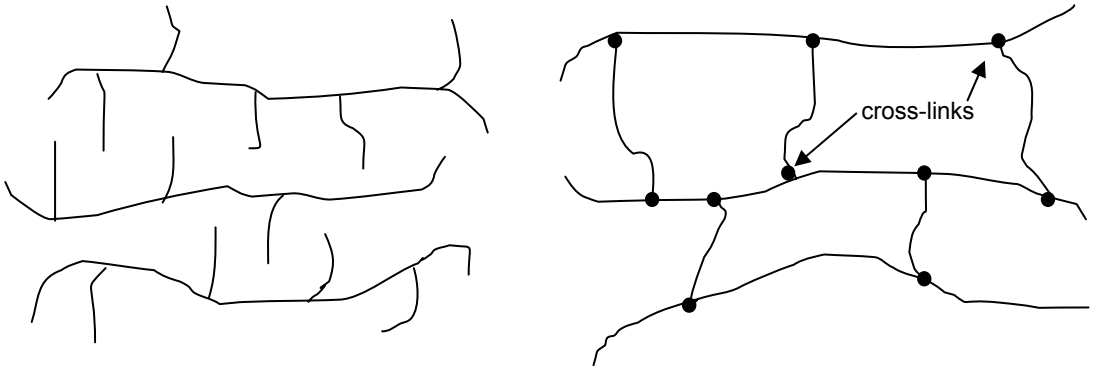

Figure 2.1: Schematic representation of (a) thermoplastic polymer held in place by weak secondary bonds and (b) thermosetting polymer with cross-linking.

Thermosetting polymers are insoluble and infusible because they are joined with strong covalent bonds. After cure the molecules are chemically connected by cross-links, forming a rigid three-dimensional network, depicted in Figure 2.1(b). Once the polymerization reaction has occurred, the cross-links have been formed, and the thermoset cannot be melted and reshaped. In certain thermosetting polymers with low instances of cross-linking, it may be possible to soften the polymer at elevated temperatures (Mallick, 1993).

Table 2.4: Characteristics, advantages, and disadvantages of thermosets and thermoplastics.

Thermoset	Thermoplastic
Primary Characteristics	
▪ Chemical reaction, cured	▪ Non-reacting, no cure required
▪ Low strain to failure	▪ High strain to failure
▪ Low fracture energy	▪ High fracture energy
▪ Irreversible processing	▪ Very high viscosity
▪ Very low viscosity possible	▪ Reversible processing
▪ Absorbs moisture	▪ Absorbs little moisture
▪ Excellent solvent resistance	▪ Fair solvent resistance
Advantages	
▪ Low processing temperature	▪ Short processing time possible
▪ Good fiber wetting	▪ Can be recycled
▪ Formable into complex shapes	▪ Can be reprocessed
▪ Liquid-resin manufacturing feasible	▪ Rapid processing
▪ Resistant to creep	▪ Unlimited shelf life
	▪ High delamination resistance
Disadvantages	
▪ Long processing time	▪ Lower resistance to solvents
▪ Long cure cycle	▪ Can be prone to creep
▪ Limited storage life	▪ Poor drapability and tack
▪ Cannot be reprocessed	▪ High temperature and pressure processing required

The relative properties of thermosets and thermoplastics polymers as well as their advantages and disadvantages are summarized in Table 2.4. The selection of the matrix materials is primarily based on its basic mechanical properties. It is desirable to have a matrix with high tensile modulus, which influences the compressive strength. Intraply cracking is controlled by high tensile strength, and ply delamination and crack growth are inhibited by high fracture toughness (Mallick, 1993).

While there are obvious distinct advantages to using a thermoplastic matrix, thermosets have traditionally been favored in fiber reinforced composites. The thermoset epoxy is the most common type of matrix material, with more than two-thirds of the polymer matrices used in aerospace applications being epoxy based (Kaw, 2006). The range of typical properties of epoxy resins are provided in Table 2.5.

Table 2.5: Typical properties of cast epoxy resin at ambient conditions.

Property	Units	Value
Specific gravity	-	1.2-1.3
Tensile strength	MPa	55-130
Tensile modulus	GPa	2.75-4.10
Poisson's ratio	-	0.2-0.33
Cure shrinkage	%	1-5
Coefficient of thermal expansion	μm/m/˚C	50-80

The principal disadvantages to epoxies are its relatively high cost and long cure time, but there are numerous advantages to epoxy matrices including:

- High strength
- Low volatility during cure
- Low shrinkage during cure
- Low viscosity and flow rates
- Excellent resistance to chemicals and solvents
- Excellent adhesion to a variety of fillers, fibers, and substrates
- Available in a variety of grades to meet specific property and processing requirements

In structural applications, fiber reinforced composites are commonly used in the form of a laminate. The laminate is created by stacking thin layers of fibers and matrix until a desired thickness is obtained. The fiber orientation and stacking sequence can be controlled to meet the demands of the operating environment. Thin sheets of fibers impregnated with predetermined amount of uniformly distributed polymeric matrix are available in the form of prepreg. Epoxy is the primary matrix material used in prepregs. The fibers are preimpregnated with liquid resin which is then partially cured in a controlled manner in a heating chamber. The prepreg can then be placed in a desired mold to be processed to undergo its final stage of curing.

For this study, a unidirectional glass/epoxy prepreg tape supplied by Bryte Technologies, Inc. (Bryte) was selected. A prepreg was chosen due to the manner in

which it lends itself to strategic sensor placement and varying sensor configurations. Instances of sensor migration were minimized. The prepreg system consisted of S-2-glass and BT250E-1 epoxy resin. The fiber aerial weight was 284 g/m^2. The uncured resin content was 35% by weight. The BT250E-1 epoxy resin system was selected for its combination of toughness and strength. The resin system is MIL-R-9300 qualified and ideal for applications in the low to medium service temperature range. The S-2-glass fiber was selected for its high strength, high modulus, and cost effectiveness. The typical neat resin properties as supplied by Bryte are detailed in Table 2.6 (refer to section 2.2.3 on the ultrasonic testing of the resin for verification of these properties).

Table 2.6: Typical neat resin properties of BT250E-1 epoxy resin as supplied by Bryte Technologies, Inc.

Property	Unit	Value
Density	g/cc	1.17
Tensile Strength	MPa	75.15
Tensile Modulus	GPa	3.03

2.2.1 Composite processing

In order to ensure the quality of the S-2-glass/epoxy prepreg, the material was either stored in an airtight bag with desiccant and kept frozen below zero degrees Celsius or stored in a vacuum chamber which maintained vacuum at 5 mm Hg. While very resistant to moisture absorption after cure, epoxies can be adversely affected by moisture uptake prior to cure. For this reason, the prepreg material was thoroughly thawed in its airtight bag prior to opening to avoid condensation on the material.

Flat panels measuring 305 mm by 305 mm were created using an aluminum mold. The mold consisted of a base tool plate made of aluminum covered in a Teflon film. Silicone rubber was placed along the edges of the material coinciding with the fiber direction to dam the material. Bleeder material was placed along the material edges perpendicular to the fiber direction to absorb excess resin. A second layer of Teflon film covered the entire setup. Aluminum rails, coinciding with the fiber direction, secured the Teflon and silicone rubber dams in place via screws. The two ends containing bleeder material each had a Teflon tube which attached to vacuum valves to draw vacuum in parallel. A 305 mm by 305 mm, 12.7 mm thick piece of aluminum, or caul plate, was placed directly on top of the Teflon sheet covering the prepreg to keep the surface of the laminate flat during cure (Lin and Chang, 2002). The entire layup was sealed in vacuum bagging. Due to symmetry, half of the schematic of the layup sequence is depicted in Figure 2.2.

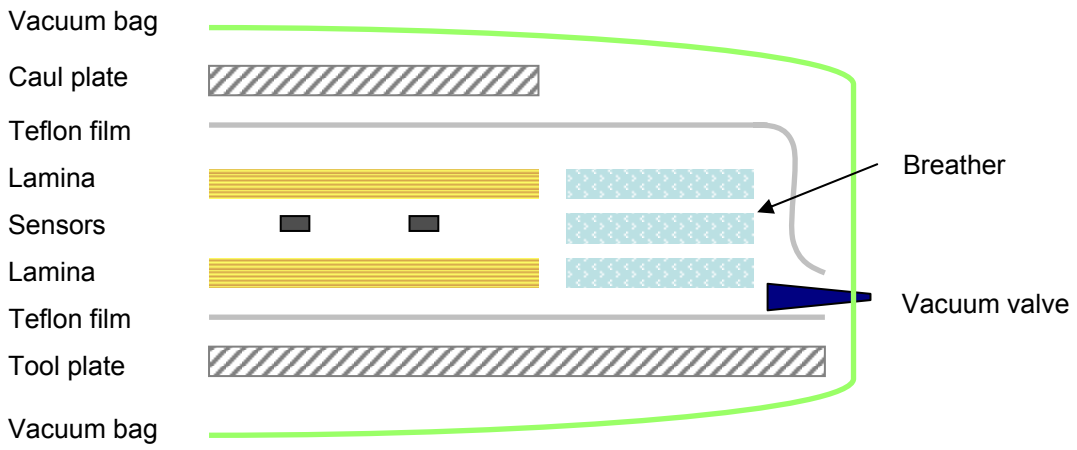

Figure 2.2: Vacuum bagging sequence for embedding sensors inside S-2-glass/epoxy prepreg composite laminate.

Figure 2.3: 125 ton Wabash laminating hot press at CEAM in which S-2-glass/epoxy laminates were processed.

While a minimum vacuum of 635 mm Hg (typically less than 10 mm Hg vacuum was achieved) and 0.35 MPa pressure were applied, the layup was placed in a 125 ton Wabash laminating hot press seen in Figure 2.3.

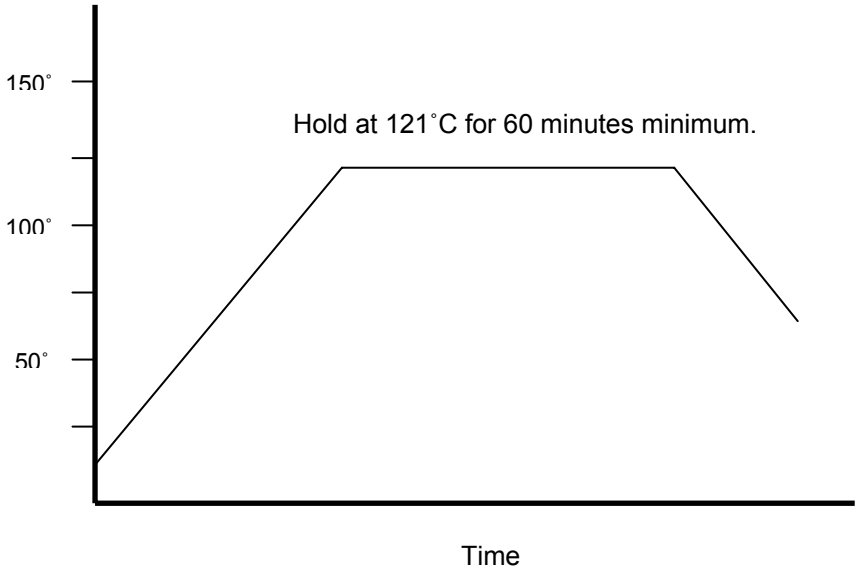

Figure 2.4: Cure cycle for S-2-glass/BT250E-1 prepreg per Bryte Technologies, Inc.

The composite panels were processed in accordance with Bryte's recommendations; see Figure 2.4. Flat panels were cured using a 3˚C/min heating rate. The panels were ramped up to a final temperature of 121˚C and were allowed to dwell at this temperature for 1.5 hours. The setup remained in the hot press under pressure until it cooled to room temperature.

2.2.2 Ignition loss testing

Samples from all composite panels were subjected to ignition loss testing in order to determine the fiber volume fraction. Thus, it was insured that the composite panels were uniform within reason and suitable for comparison to one another. The ignition loss tests were conducted in accordance with ASTM D 2584-02. The tests were performed in the muffle furnace as seen in Figures 2.5 (a) and (b).

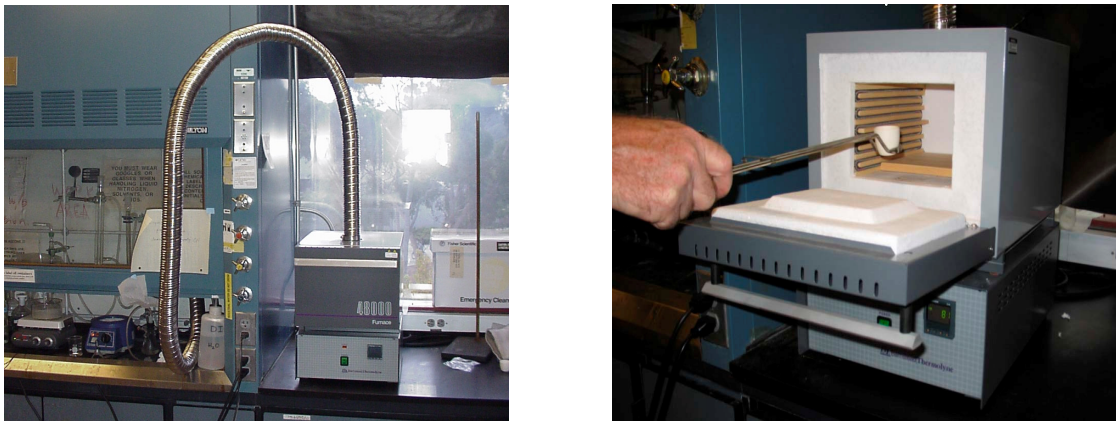

Figure 2.5: (a) Muffle furnace at CEAM utilized for ignition loss testing. (b) Crucible insertion into muffle furnace for ignition loss testing during which a specimen undergoes a rigorous heating schedule that ignites and burns the resin until only fibers remain.

The outer 25.4 mm perimeter was discarded as it was not necessarily representative of the general composition of the composite panel. Ignition loss specimens measuring 12.7 mm by 12.7 mm were extracted from the composite panels in the approximate locations depicted in Figure 2.6 using a computer numerical controlled (CNC) 3-axis milling machine.

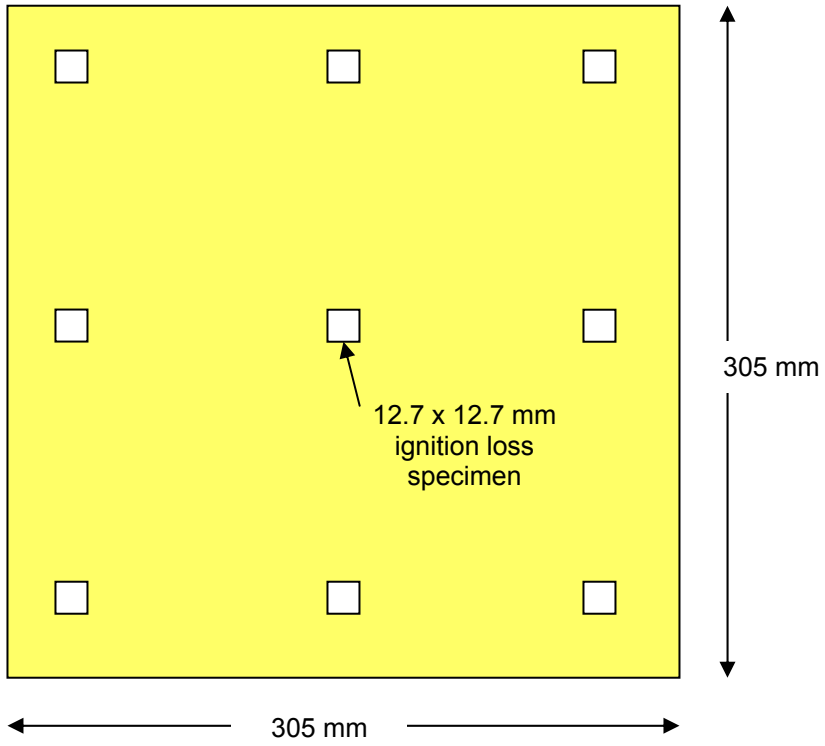

Figure 2.6: Location of ignition loss specimen extraction from a composite panel. The mapping of the specimen location is noted for each panel in order to ensure panel uniformity.

The ignition loss specimens were placed in porcelain crucibles and then positioned in the muffle furnace where they were subjected to the following heating schedule: 350°C for 30 minutes, 400°C for 30 minutes, 450°C for 30 minutes, and finally 565°C for 150 minutes. Glass fibers were all that remained in the crucibles

after being subjected to the rigorous heating schedule. The crucibles were cooled to room temperature in a desiccator and then weighed. The fiber volume fraction was determined using the following equation:

$$v_f = \frac{\rho_m W_f}{\rho_f W_m + \rho_m W_f} \tag{2.1}$$

where v_f is the volume fraction of fibers, W_f is the weight of the fibers, W_m is the weight of matrix, ρ_f is the density of fibers, and ρ_m is the density of matrix.

The ignition loss tests determined the average fiber volume fraction for the panels. The values can be found in the respective results section of this work.

2.2.3 Ultrasonic testing of resin

Additional testing, in the form of ultrasonic testing of the resin was performed in order to more accurately determine the properties of the resin, or matrix constituent, of the prepreg being used throughout the experimental testing needed for accurate simulations being conducted by Mr. Yi Huang.

A pure resin sample was created from partially cured BT250E-1 resin provided by Bryte. The semi-solid resin was placed in a glass beaker and then connected to a Buchi Rotovapor R-200 (see Figure 2.7) and partially submerged in a silicone oil bath. The resin was heated at a rate of 3°C per minute until it reached its minimum viscosity at 112°C; see Figure 2.8. The resin was then poured into a Teflon film coated

aluminum mold. The mold was then placed in the 125 ton hot press for 1.5 hours at 121°C and under 0.35 MPa pressure to allow the resin to fully cure.

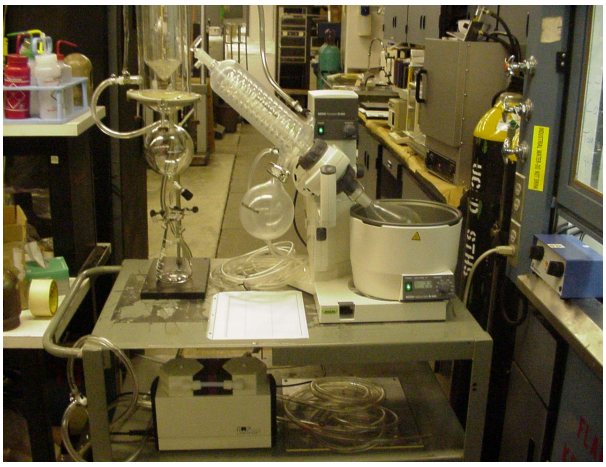

Figure 2.7: Buchi Rotovapor R-200 used to heat BT250E-1 resin in a silicone oil bath.

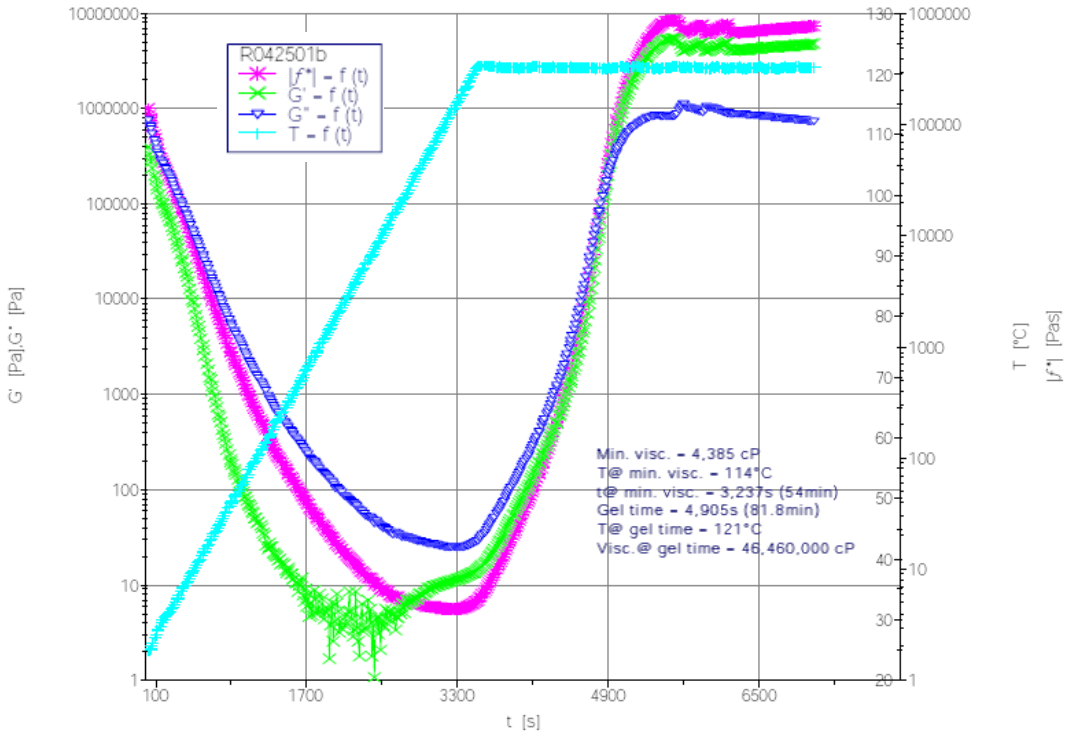

Figure 2.8: Temperature to achieve minimum viscosity for BT250E-1 epoxy resin and duration at minimum viscosity provided by Bryte Technologies, Inc.

The resulting resin specimen was machined by a mill to create an even surface on both sides. The thickness of the resin specimen was determined to be 5.38 mm (+/- 0.005 mm).

Essentially, time of flight measurements through the thickness of the sample were used to measure the properties of the resin. The equipment included two Panametrics V155 (5 MHz resonance) and V153 (1 MHz resonance) shear transducers, two Panametrics V112 (10 MHz resonance) and V213BB (30 MHz resonance) delay line transducers (longitudinal), and a Matec TB 1000 pulse generator.

When the generated shear wave enters the material it is only partially transmitted as a shear wave. It also produces a longitudinal wave. Since the longitudinal wave travels faster, it can be separated from the complimentary shear wave and both times of flight can be measured.

Due to the given resonance frequencies of the respective transducers, the measurements made with the shear transducers were performed at 500 kHz with a pulse width of 10 μs. For the compression transducers 5MHz was used with a pulse width of 1 μs.

Both the transmitter and receiver signals were connected to an oscilloscope (Gage-scope and Tektronix TDS2014) and the time shift in signals was taken.

The density of the material (ρ) was 1.17 g/cm^3 as given in the manufacturer specification sheet and confirmed with mass and water displacement volume measurements.

The transverse wavespeed (v_t) was determined to be 1090 km/s and the longitudinal wavespeed (v_l) was determined to be 2560 km/s. Using these experimentally determined values, the shear modulus (G) can be calculated as follows (given that it is a plane strain regime):

$$G = \rho(v_t)^2 \tag{2.2}$$

Based upon the above equation, the shear modulus is 1.39 GPa. Similarly, the Young's modulus (E) was calculated by combining the following two equations and solving for Poisson's ratio (ν):

$$E = \rho(v_l)^2(1+\nu)\frac{(1-2\nu)}{(1-\nu)} \tag{2.3}$$

$$E = 2G(1+\nu) \tag{2.4}$$

Thus, the Poisson's ratio is equal to 0.39, and the Young's modulus is 3.86 GPa for the BT250E-1 resin system.

Additional mechanical testing was conducted on a pure BT250E-1 resin specimen. Unfortunately, the specimen had a slight edge flaw due to machining that acted as a stress concentration. Despite the flaw, the testing determined that the tensile strength of the resin was 68 MPa. The manufacturer, Brtye, specifies that the tensile strength is 75 MPa. Therefore, taking into account the small machining flaw, the tensile strength of the BT250E-1 resin is taken to be 75 MPa.

2.3 Sensors

Previous efforts to integrate sensors into composite materials have often focused on fiber optic sensors due to the fact that the sensor itself is a fiber that can commingle with the other reinforcing fibers of the material as evidenced in the review paper by Zhou and Sim (2002). MEMS and other microprocessors offer a much more diverse sensing potential than fiber optic sensors. Furthermore, fiber optic sensors do not present a networking option within the structure itself, which is integral to a truly *sensing* composite material (Nemat-Nasser et al., 2005).

Advances in the microelectronics industry are clearly showing progress towards achieving smaller chip and package sizes, consuming less power, while also steadily increasing the processing and functionality. This work anticipates the continued push for smaller and more powerful microprocessors, which will assist in mitigating mechanical degradation when integrated into structural composite materials.

The envisioned sensors could potentially measure such structural health related parameters including temperature, load, strain, acceleration, or acoustic emissions. An initial feasibility study was conducted using a digital thermometer as the demonstration sensor (see section 2.3.1). Based upon the success of this preliminary work, mechanical testing focused on integrating a simulated microsensor in the form of a chip resistor (see section 2.3.2). Further efforts to minimize the impact of the sensor on the mechanical properties of the host composite led to the investigation of polyvinylidene fluoride (PVDF) thin film sensors (see section 2.3.3).

2.3.1 Temperature sensor

Preliminary work to demonstrate the feasibility of embedding sensors in composite materials was undertaken by Nemat-Nasser et al. (2005). In this initial stage a DS18B20X digital 1-wire thermometer from Maxim/Dallas Semiconductor was utilized. The dimensions of the DS18B20X are detailed in Figure 2.9 showing its footprint of 1.32 mm by 1.93 mm with a height of 0.69 mm. It also has a unique 64-bit address in ROM, and can draw power and communicate via a single wire. The communications interface supports a multi-drop network, enabling many such devices to operate on the same conductor pair. A microprocessor was programmed to communicate over the network and a more robust configuration with separate power and communications lines which share a common ground line was implemented.

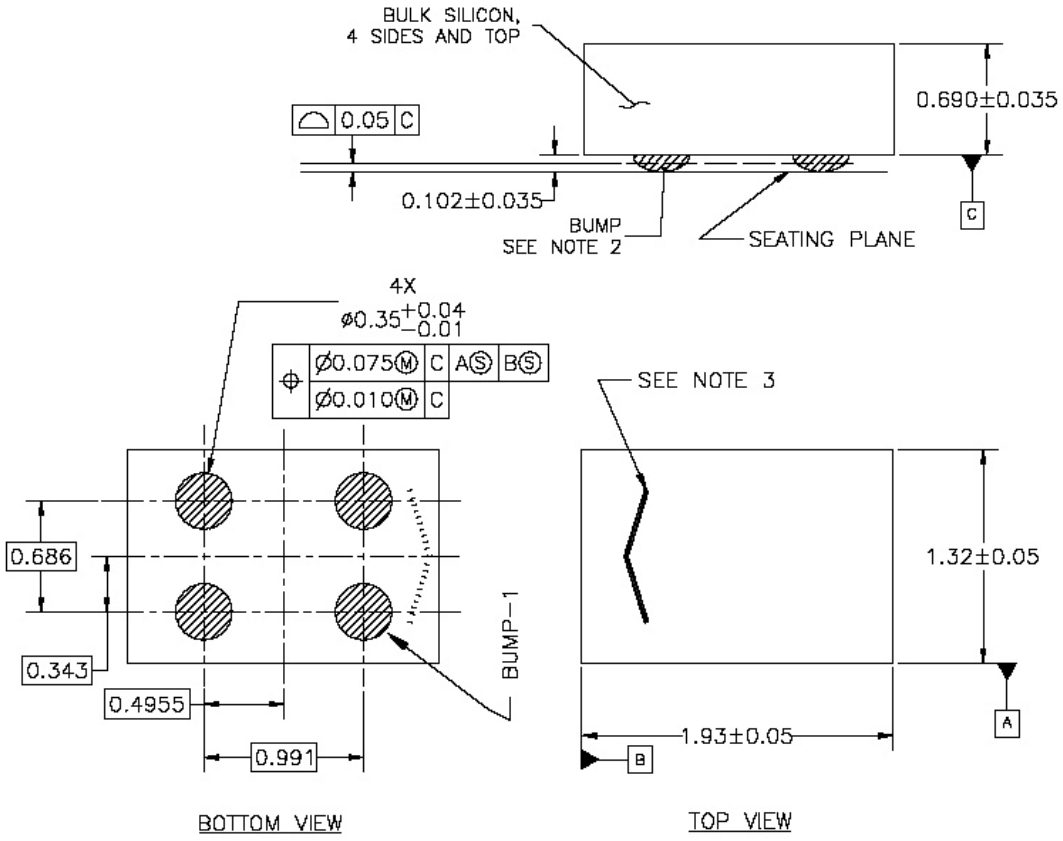

Figure 2.9: DS18B20X digital 1-wire thermometer from Maxim/Dallas Semiconductor shown from side view, bottom view, and top view with mechanical specifications used as the initial demonstration sensor by Nemat-Nasser et al. (2005).

The initial demonstration utilized a conventional fiberglass based printed circuit board (PCB) substrate. The substrate, FR4, measured 0.254 mm thick, 2.03 mm wide, and 152.4 mm long with a 0.5 oz. copper foil overlay. A rapid PCB prototyping numerical controlled milling machine was used to create the device land pattern seen in Figure 2.10. The DS18B20X was attached to the substrate a using convection hot gas solder reflow technique.

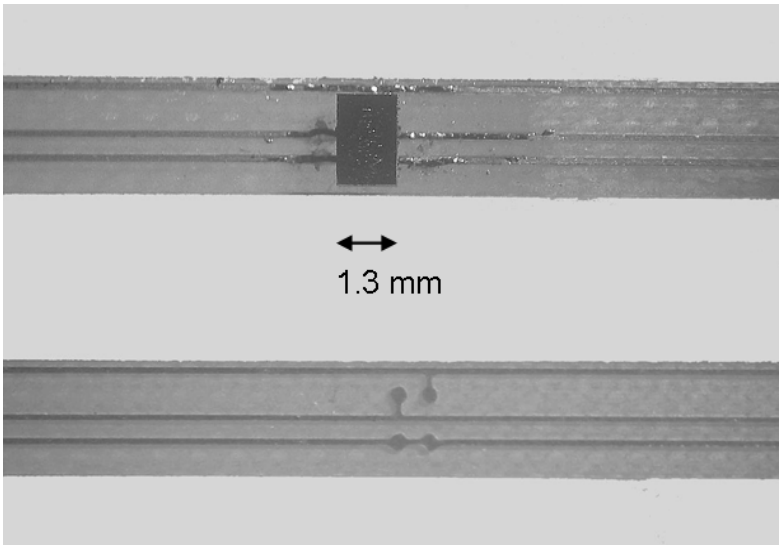

Figure 2.10: Photograph showing substrate with fabricated traces and land pattern (below) and with sensor attached (above). Reproduced from Nemat-Nasser et al. (2005).

After electronic testing, the substrate with attached sensor was embedded in a glass/epoxy prepreg composed of E-glass and BT-250 epoxy resin as provided by Bryte. The substrate and sensor were placed at the midplane of eight layers of prepreg and underwent processing at 121°C with 0.35 MPa of pressure applied for one hour as indicated in the manufacturer's processing specifications.

Once it was determined that the embedded sensor successfully survived processing, a ten by ten array of the sensors was fabricated on similar printed circuit board material. The substrate and sensors were embedded in an aramid/epoxy composite via vacuum-assisted resin transfer molding (VARTM). The resulting panel and its temperature sensing ability are shown in Figure 2.11. Refer to Nemat-Nasser et al. (2005) for further details on the preliminary feasibility studies.

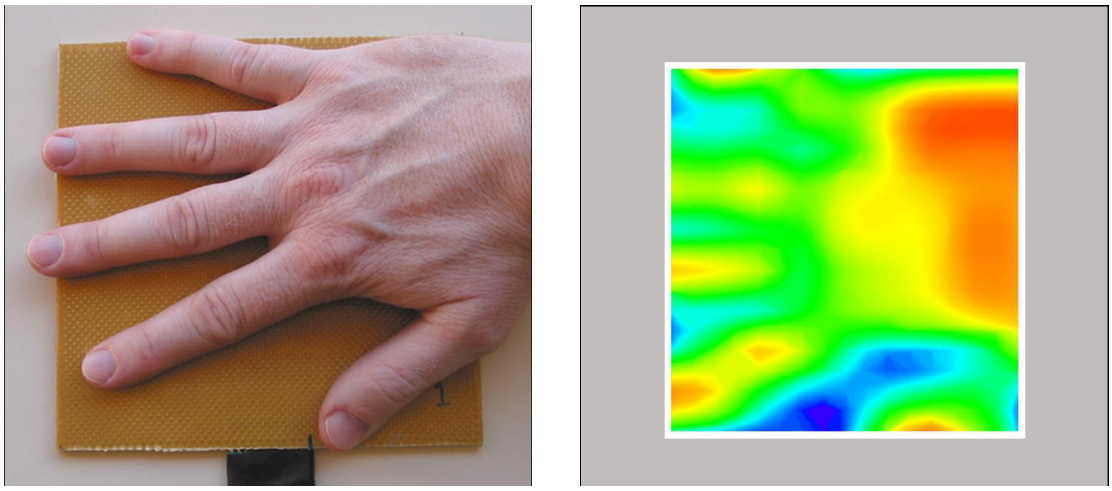

Figure 2.11: Aramid/epoxy composite panel with embedded network consisting of a 10 by 10 array of individually addressable thermal sensors. A hand is placed on the panel (left) generating a thermal image (right). Reproduced from Nemat-Nasser et al. (2005).

2.3.2 Simulated microsensor/chip resistor

With the success of the feasibility study came interest in how the microsensor affected the mechanical performance of the composite material. Due to the high cost associated with the DS18B20X digital 1-wire thermometer demonstration sensor, a suitable simulated microsensor was chosen in the form of a chip resistor. A 2A or 0805 chip resistor was selected to mimic the DS18B20X sensor in both size and material for the mechanical testing. During the mechanical testing to determine the effects on the structural integrity of the host composite material, the embedded sensor will not be actively sensing, further supporting the use of a simulated microsensor. The mechanical construction and dimensions of the chip resistor are shown in Figure 2.12 and Table 2.7.

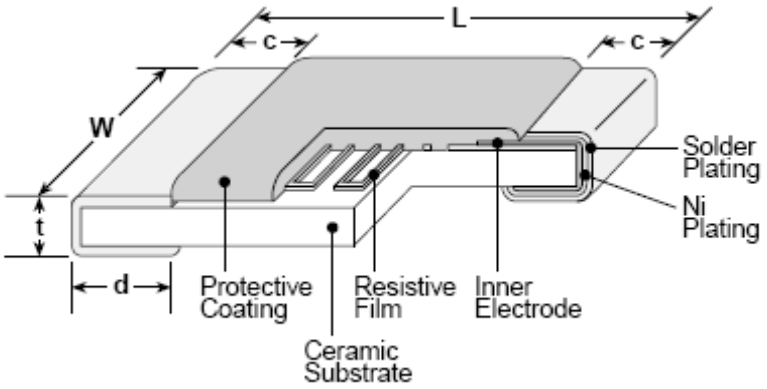

Figure 2.12: Dimensions and construction of chip resistor used as simulated microsensor. Courtesy of Koa Speer Electronics, Inc.

Table 2.7: Dimensions of 2A or 0805 chip resistor used as simulated microsensor. Courtesy of Koa Speer Electronics, Inc.

Type (Inch Size Code)	Dimensions inches (mm) L	W	c	d	t
1E (0402)	.039 +.004 -.002 (1.0 +0.1 -0.05)	.02±.002 (0.5±0.05)	.008±.004 (0.2±0.1)	.01 +.002 -.004 (0.25 +0.05 -0.1)	.014±.002 (0.35±0.05)
1J (0603)	.063±.008 (1.6±0.2)	.031±.004 (0.8±0.1)	.012±.004 (0.3±0.1)	.012±.004 (0.3±0.1)	.018±.004 (0.45±0.1)
2A (0805)	.079±.008 (2.0±0.2)	.049±.004 (1.25±0.1)	.016±.008 (0.4±0.2)	.012 +.008 -.004 (0.3 +0.2 -0.1)	.02±.004 (0.5±0.1)
2B (1206)	.126±.008 (3.2±0.2)	.063±.008 (1.6±0.2)	.02±.012 (0.5±0.3)	.016 +.008 -.004 (0.4 +0.2 -0.1)	.024±.004 (0.6±0.1)
2E (1210)		.098±.008 (2.5±0.2)			

2.3.3 Polyvinylidene fluoride (PVDF) sensor

The detection of acoustic emissions indicative of events such as matrix cracking, matrix/fiber debonding, and fiber breakage would provide a valuable indication of the health of a structure. As this study became interested in detecting acoustic emissions, piezoelectric sensors in the form of polyvinylidene fluoride

(PVDF) thin film sensors presented themselves as very viable options. Figure 2.13 depicts PVDF sensors with signal conditioning in a slave/master network configuration. While other materials exhibit a piezoelectric effect, none are as highly piezoelectric as PVDF and its copolymers. The recent development of new copolymers of PVDF permits its use at higher temperature around 135˚C (Measurement Specialities, Inc., 2006). Piezofilms are desirable due to their excellent sensitivity and mechanical toughness (Gautschi, 2002). Several configurations of PVDF thin film sensors were investigated in this study. They are detailed in the following sections.

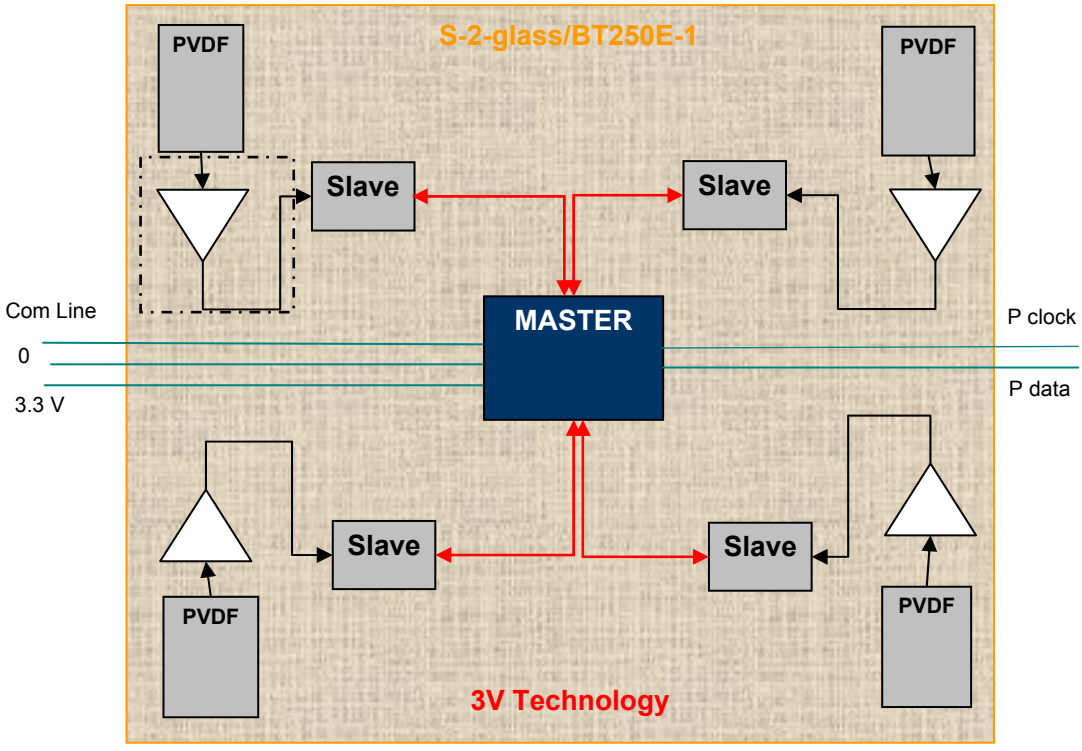

Figure 2.13: Diagram of proposed network configuration with PVDF sensor to detect acoustic emissions. The PVDF sensor requires signal conditioning and then connects to the slave which reports to the master. Diagram courtesy of Dr. Fabrizia Ghezzo.

2.3.3.1 PVDF sensor with protective coating

This study initially investigated 55 μm thick PVDF sensors with flexible leads as depicted in Figure 2.14. The FDT1-028K model PVDF sensor supplied by Measurement Specialties, Inc. consisted of a rectangular element of piezofilm with silver ink metallization and a piezo polymer tail that extends from the active sensor area as flex circuit material with offset traces all of which was covered with a screen printed acrylic protective coating. The dimensions of the PVDF sensor are detailed in Table 2.8. With the exception of the connector pins, the whole PVDF sensor with flexible leads was embedded in the composite material with test specimens extracted from the entire length. The results of the specimens that contained the electrode versus the offset traces are given in the respective results sections of this work.

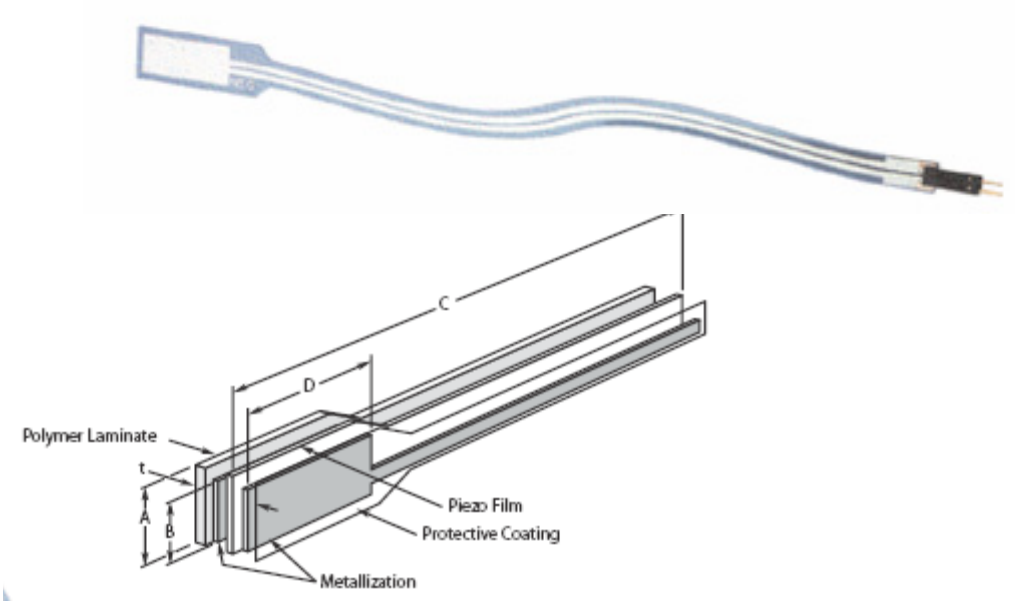

Figure 2.14: Photograph and diagram of FDT1-028K model PVDF thin film sensor with details of construction. Courtesy of Measurement Specialties, Inc. (2006).

Table 2.8: Dimensions of FDT1-028K model PVDF thin film sensor depicted in Figure 2.14.

	A	B	C	D
Description	**Film**	**Electrode**	**Film**	**Electrode**
FDT1-028K	16 mm	12 mm	235 mm	30 mm

2.3.3.2 PVDF sensor without protective coating

Bonding issues between the screen printed acrylic protective coating on the FDT1-028K model PVDF sensors and the epoxy arose during the initial mechanical testing. Subsequent tests focused on PVDF sensors consisting strictly of the piezo film and metallization as depicted in Figure 2.15.

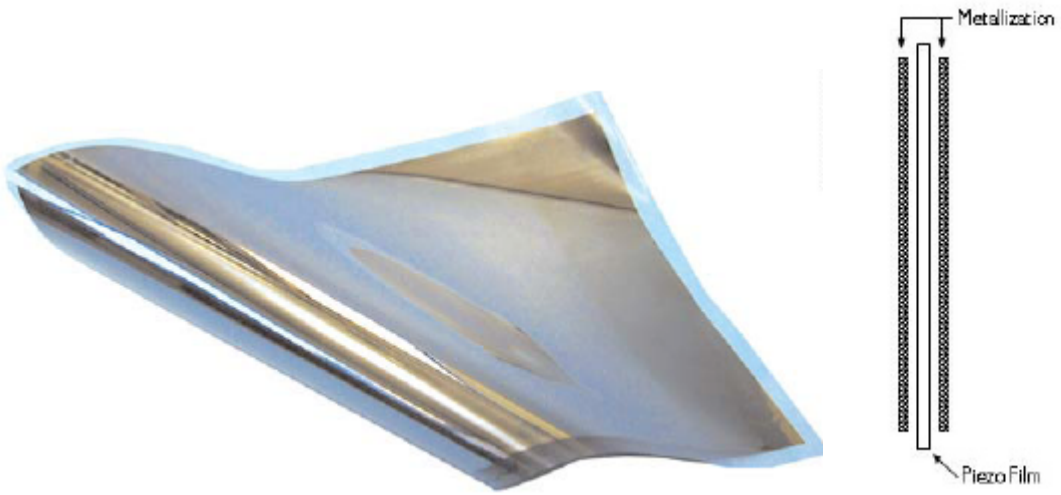

Figure 2.15: Photograph and construction of metallized piezo film sheet. Courtesy of Measurement Specialties, Inc. (2006).

Two types of metallized piezo film sheets were investigated; silver ink metallization and a nickel copper alloy metallization. Silver ink is recommended for

applications where mechanical stress is being applied, whereas the nickel copper alloy has good conductivity and is resistant to oxidation. The metallized piezo film sheets were nominally 28 μm thick; however, only the nickel copper alloy measured 28 μm thick. The silver ink had an actual thickness of 40 μm. The areal dimensions of the bulk sheets are shown in Figure 2.16.

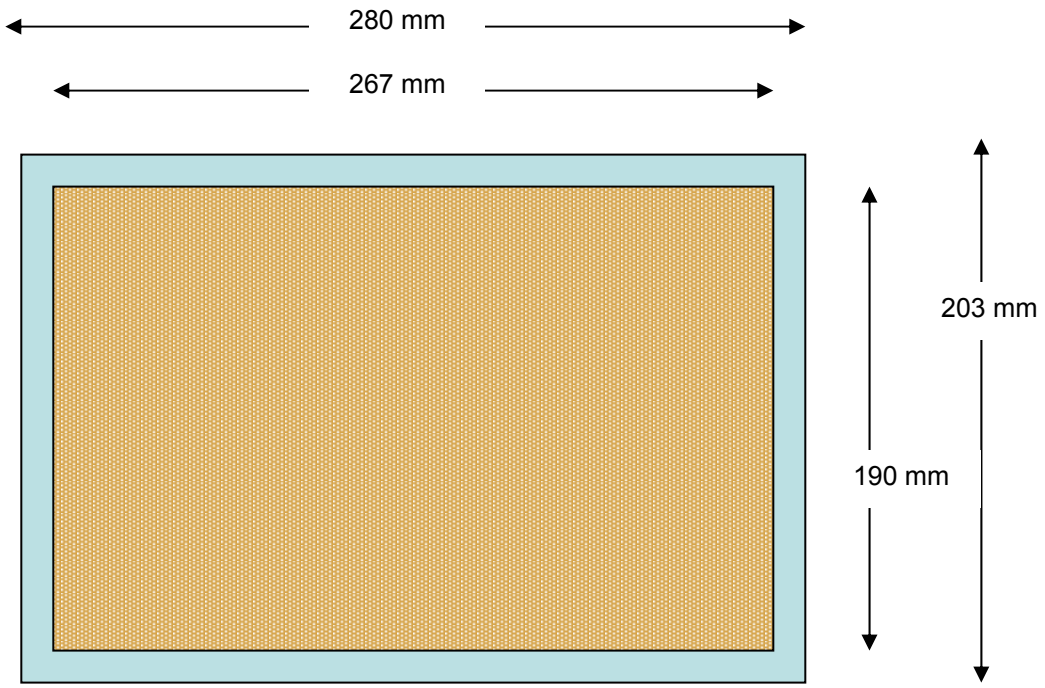

Figure 2.16: Dimensions of the piezo film and metallization on the bulk sheets of the PVDF sensors which lack the problematic screen printed acrylic protective coating.

2.4 Summary

The selected composite system and its rationale for use were presented along with the composite processing and quality assurance procedures used in this study. An initial feasibility study by Nemat-Nasser et al. (2005) demonstrated the ability to

detect thermal changes in a composite material via embedded sensors. The types of sensors investigated in this work, including simulated microsensors in the form of 2A or 0805 chip resistors and PVDF thin film sensors were introduced.

2.5 Acknowledgement

I would like to thank Mr. Patrick Rye for his assistance with creating the pure resin samples. Mr. Jon Isaacs and Mr. Patrick Rye were integral in utilizing the ultrasonic equipment for the material property extraction of the neat resin.

Chapter 3

Quasi-static tension test

3.1 Introduction

When introducing elements to create an intelligent structure, the principal concern is the effect of the embedments on the load carrying capability, structural life, and effective elastic modulus of the host composite material. These issues can be addressed by selecting a compatible sensor with minimal size such that it presents the smallest interruption to the fewest number of plies in the laminate (Warkentin and Crawley, 1991).

The quasi-static tensile tests were conducted in order to characterize the ultimate tensile strength, Young's modulus, ultimate transverse tensile strength, transverse Young's modulus, and maximum in-plane shear strength of the virgin host composite material. Furthermore, the tests were utilized to characterize the effects of the simulated microsensor on the strength of the host composite material and the failure mechanism. The tests were conducted in accordance with ASTM 3039 and ASTM 3518 standards.

3.2 Specimen preparation

3.2.1 Specimen layup and fabrication

All of the composite panels utilized in this study were processed in a 125 ton Wabash laminating hot press according to the general manufacturer specifications detailed in Section 2.2.1 with the bagging sequence provided in Figure 2.2. More specifically, the quasi-static tensile tests investigated specimens created from four layup scenarios detailed in Figure 3.1.

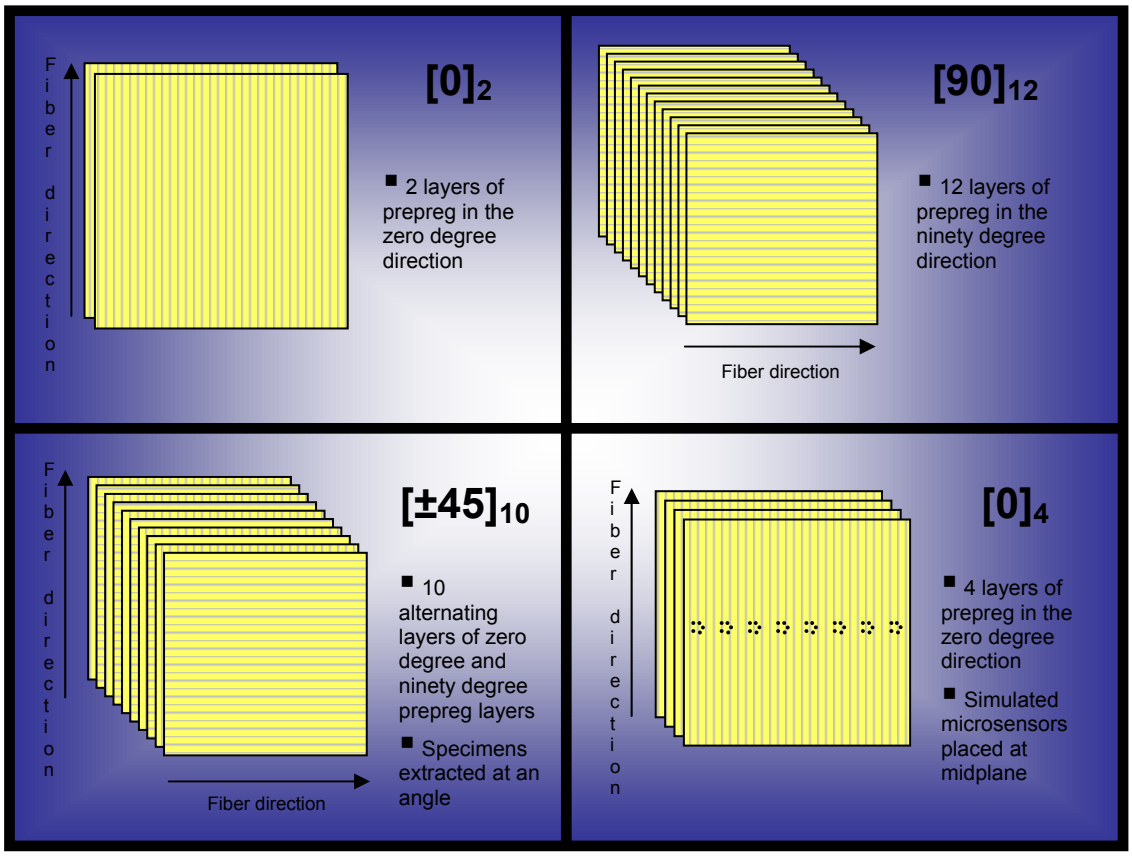

Figure 3.1: Composite laminate prepreg layup sequences for creating $[0]_2$, $[90]_{12}$, $[\pm45]_{10}$, and $[0]_4$ with simulated microsensors test specimens for the quasi-static tensile tests in order to characterize the ultimate tensile strength, Young's modulus, ultimate transverse tensile strength, transverse Young's modulus, and maximum in-plane shear strength of the virgin material as well as to characterize the effect of the embedment.

3.2.2 Specimen machining

For the quasi-static tension test specimens, a preliminary cut using a band saw was made in order to cut the composite panel down from a size of 305 mm by 305 mm to a size of 254 mm by 254 mm, thus eliminating the undesirable edges of the outer perimeter of the composite panel. The panel was then clamped to a polyvinyl chloride (PVC) platen and covered with a 1.6 mm thick PVC sheet in order to obtain a clean cut edge without any fiber fraying. A 3.175 mm (1/8 inch) four flute aluminum titanium nitride coated end mill was used to cut the samples using a CNC 3-axis milling machine. The cuts were made at a speed of 1500 rpm with a feed rate of 101.6 mm per minute. Throughout the machining process, the composite panels were flooded with a coolant which was composed of water and a rust inhibitor. The samples were then cleaned with water and thoroughly dried.

3.2.3 Specimen tabbing

Tabs are highly recommended when testing unidirectional materials to failure in the fiber directions as described in ASTM 3039. Based upon this, tabs were used when testing the $[0]_2$ specimens and the $[0]_4$ specimens with one simulated microsensor at the mid-plane between layers of prepreg. Tabs are also strongly recommended when testing unidirectional materials in the matrix direction in order to prevent gripping damage, and thus tabs were used on the $[90]_{12}$ specimens.

All tabs were created using the same Bryte prepreg used to create the test specimens. The tabs were machined using the CNC 3-axis milling machine. The tab dimensions were 25.4 mm wide and 50.8 mm in length. The tabs maintained a low beveled edge in order to successfully transition into the gage section of the specimen.

For alignment purposes, tabs of matched thickness were always used. The tabs were bonded to the individual test specimens using Techkits A-12 rigid bond epoxy adhesive consisting of a two-part resin and catalyst. The Techkits epoxy was applied to the clean surfaces of the tab and test specimen. After twenty-four hours at room temperature with contact pressure applied, the epoxy cure was complete. The mechanical properties of the Techkits epoxy at ambient conditions are supplied in Table 3.1.

Table 3.1: Typical mechanical properties of Techkits A-12 rigid bond epoxy adhesive at ambient laboratory conditions.

Property	Units	Techkits A-12 Epoxy
Tensile strength	MPa	62.05
Shear strength	MPa	41.37
Compressive strength	MPa	110.32
Flexural strength	MPa	103.42
Coefficient of thermal expansion	μm/m/˚C	28

Multidirectional laminates can be successfully tested without the use of tabs, as was the case with the $[\pm 45]_{10}$ specimens tested here.

3.2.4 Thickness and width measurements

The tension test specimen width was measured at the central gage location, while the thickness measurements were taken at three points along the specimen length using flat nose digital calipers. The average of these measurements was determined and used in calculations.

3.3 Specimen configurations

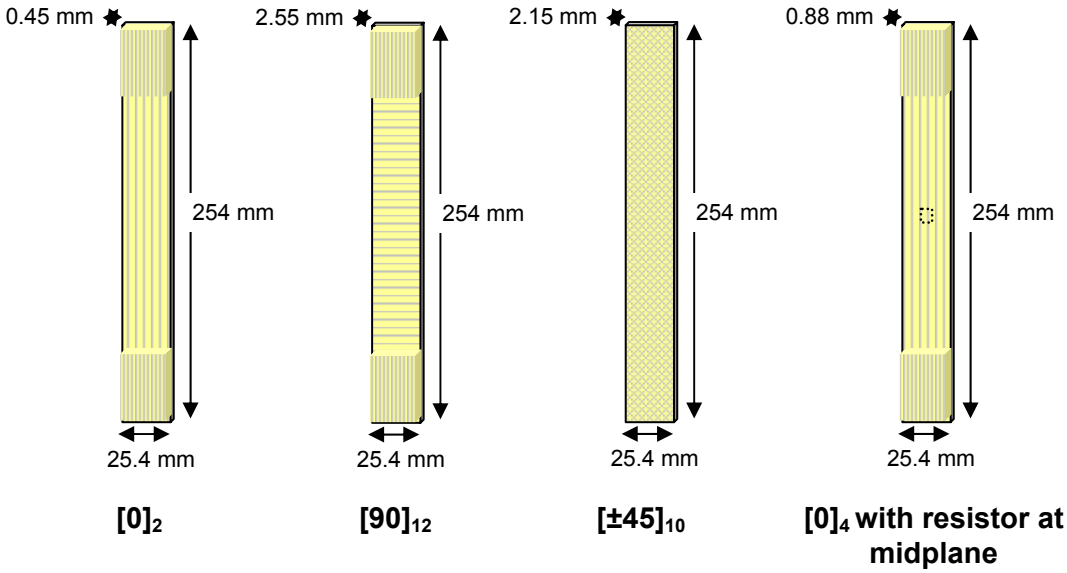

Figure 3.2: Specimen configurations for the quasi-static tensile tests.

Four specimen configurations were tested in this study as depicted in Figure 3.2. $[0]_2$ specimens were created to characterize the ultimate tensile strength and Young's modulus of the material. $[90]_{12}$ specimens were created to characterize the ultimate transverse strength and transverse Young's modulus of the material. $[\pm45]_{10}$

specimens were created to characterize the in-plane shear response of the material. Finally $[0]_4$ specimens with one simulated microsensor at the midplane were created to determine the effect an embedment would have on the ultimate tensile strength and Young's modulus.

The specimens maintained a length of 254 mm and were 25.4 mm wide with the respective thicknesses shown in Figure 3.2. The addition of the simulated microsensor to the midplane of the $[0]_4$ specimens still allowed for a completely smooth surface finish. The specimens which had tabs applied had a central gage section measuring 152.4 mm in length.

3.4 Testing equipment and test configuration

The quasi-static tension tests were performed using an MTS model 312.21 load frame with an MTS model 407 load unit controller. The load frame was equipped with an 88.9 kN (20000 lb) load cell (model 661.21A-03). Additionally, the load frame was equipped with model 647.10 hydraulic wedge grips as shown in Figure 3.3.

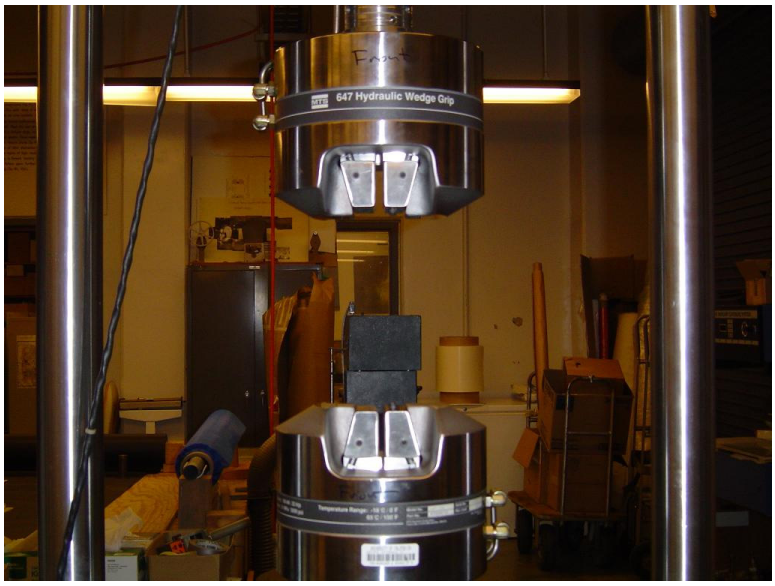

Figure 3.3: MTS model 312.21 load frame with hydraulic wedge grips and an 88.9 kN load cell used to conduct quasi-static tensile tests at CEAM.

3.5 Experimental procedure

The quasi-static tension tests were performed in displacement control, at ambient laboratory conditions. The crosshead movement was at a rate of 0.020 mm/s. The specimens were centrally aligned within the wedge grips. The test proceeded at the specified rate until failure. A minimum of three test specimens of each configuration were tested. The tests conducted on the $[0]_2$ specimens were performed in accordance with ASTM 3039 to determine the ultimate tensile strength and Young's modulus of the unidirectional composite material. The ultimate tensile strength was determined using the following:

$$F^{tu} = P^{\max} / A \tag{3.1}$$

where F^{tu} is the ultimate tensile strength (MPa), $P^{\max}$ is the maximum load before failure (N), and A is the average cross-sectional area (mm^2). Strain gages were applied to select specimens and the Young's modulus was determined using:

$$E = \frac{\Delta\sigma}{\Delta\varepsilon} \tag{3.2}$$

where E is the Young's modulus (GPa), $\Delta\sigma$ is the stress difference (MPa), and $\Delta\varepsilon$ is the strain difference.

The tests conducted on the $[90]_{12}$ were completed in order to determine the transverse Young's modulus and the ultimate transverse strength. Transverse tensile loading represents the most critical loading scenario for a unidirectional composite material. In this case, the matrix stresses and strains are the governing failure criteria (Daniel, 1993). The ultimate transverse tensile strength was determined using:

$$F_t^{tu} = P^{\max} / A \tag{3.3}$$

where F_t^{tu} is the ultimate transverse tensile strength (MPa), $P^{\max}$ is the maximum load before failure (N), and A is the average cross-sectional area (mm^2). Strain gages were applied to select specimens and the transverse Young's modulus was determined using:

$$E_t = \frac{\Delta\sigma}{\Delta\varepsilon} \tag{3.4}$$

where E_t is the transverse Young's modulus (GPa), $\Delta\sigma$ is the stress difference (MPa), and $\Delta\varepsilon$ is the strain difference.

The quasi-static tension tests on the $[\pm 45]_{10}$ were performed in order to determine the in-plane shear response of the laminates according to ASTM 3518. The maximum in-plane shear stress was determined as follows:

$$\tau_{12}^{m} = \frac{P^{m}}{2A} \tag{3.5}$$

where τ_{12}^{m} is the maximum in-plane shear stress (MPa), P^{m} is the maximum load at or below 5% shear strain (N), and A is the cross-sectional area (mm^2). The shear modulus was calculated using:

$$G_{12} = \frac{\Delta\tau_{12}}{\Delta\gamma_{12}} \tag{3.6}$$

where G_{12} is the shear modulus of elasticity (GPa), $\Delta\tau_{12}$ is the difference in applied shear stress (MPa), and $\Delta\gamma_{12}$ is the difference in shear strain.

During the tensile loading of the $[\pm 45]_{10}$ test specimens, the first ply failures consist primarily of the normal stress failures rather than pure shear failures. The surface plies which are being constrained only by one neighboring ply (as opposed to interior plies, which are constrained by two plies, one on each side) represent the weakest link. It is because of this that the actual material shear strength cannot be

determined through this test. Instead, the shear stress at failure is believed to underestimate the actual material shear strength except for the case of materials capable of sustaining large axial strains (greater than 3%).

Through these tension tests the fundamental properties of the S-2-glass/epoxy composite material are characterized. The results from tests on samples containing embedded simulated microsensors can be compared to these characteristic values to determine the effect of the embedment on the mechanical properties of the host composite material under quasi-static loading.

3.6 Experimental results and discussion

In the results for the quasi-static tension tests described below, there are results given for two materials: roll one material and roll two material. The names simply refer to two different rolls of composite prepreg material, one purchased after the other had been completely used. The two different rolls are noted because different rolls can vary slightly in composition, and the results from testing panels created from the two different rolls can be compared to see how uniform they are since numerous rolls of material will be required throughout the duration of the mechanical testing process.

The results of the $[0]_2$ specimens created from the roll one material are given in Table 3.2 and shown in Figure 3.4. Photographs of the typical failure sequence are shown in Figure 3.5. The tests concluded that the average ultimate tensile strength was 1635.09 MPa which is in agreement with the values of the properties as provided

by Bryte; see Table 3.3. Using data gathered through the use of strain gages, the Young's Modulus was determined to be 46.51 GPa, which is also in agreement with the values published by Bryte. The average fiber volume fraction of the panel used to create the test specimens was 51%.

Table 3.2: Results from quasi-static tension tests of S-2/BT250E-1 $[0]_2$ specimens from roll one material.

Sample	Ultimate Tensile Strength (MPa)	Average Ultimate Tensile Strength (MPa)	Standard Deviation	Coefficient of Variation (%)	E (GPa)	Max Deformation (%)
2	1692.258					
3	1598.519					
4	1665.651					
5	1583.925					
		1635.09	52.15	3.19	46.51	4.89

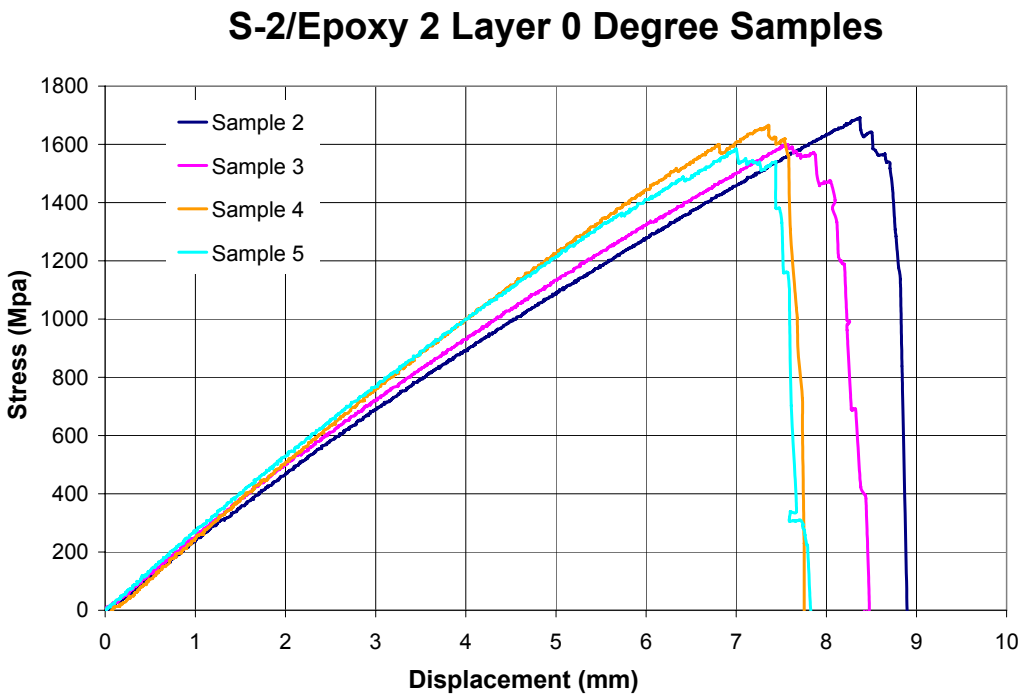

Figure 3.4: Plot of results from quasi-static tension tests of S-2/BT250E-1 $[0]_2$ specimens from roll one material.

Table 3.3: Typical mechanical properties of S-2-glass/BT250E-1 epoxy prepreg with a resin content of 33 ±3% as provided by Bryte Technologies, Inc.

PROPERTY	TENSILE STRENGTH (ksi)	TENSILE MODULUS (Msi)	COMPRESSION STRENGTH (ksi)	COMPRESSION MODULUS (Msi)	FLEXURAL STRENGTH (ksi)	FLEXURAL MODULUS (Msi)	ILSS (ksi)
AVERAGE	223.6	6.20	130.8	6.58	130.2	5.93	8.44
STD DEV	6.5	0.57	3.2	0.05	7.4	0.43	0.56
MINIMUM	210.2	3.19	125.6	6.51	111.3	5.20	7.57
MAXIMUM	234.5	6.97	133.0	6.64	141.7	6.66	9.78
RANGE	24.3	3.78	7.4	0.13	30.4	1.46	2.21
AVG-1SIGMA	217.1	5.63	127.6	6.53	122.8	5.50	7.89
AVG+1SIGMA	230.2	6.76	134.0	6.62	137.6	6.36	9.00
AVG-2SIGMA	210.6	5.06	124.4	6.48	115.5	5.07	7.33
AVG+2SIGMA	236.7	7.33	137.2	6.67	145.0	6.79	9.56
COUNT	32	32	5	5	40	40	32
LOTS	32	32	1	1	8	8	32
k VALUE (OST)	1.758	1.758	3.408	3.408	1.698	1.698	1.768
B-BASIS (OST)**	212.1	5.20	119.8	6.42	117.7	5.20	7.57

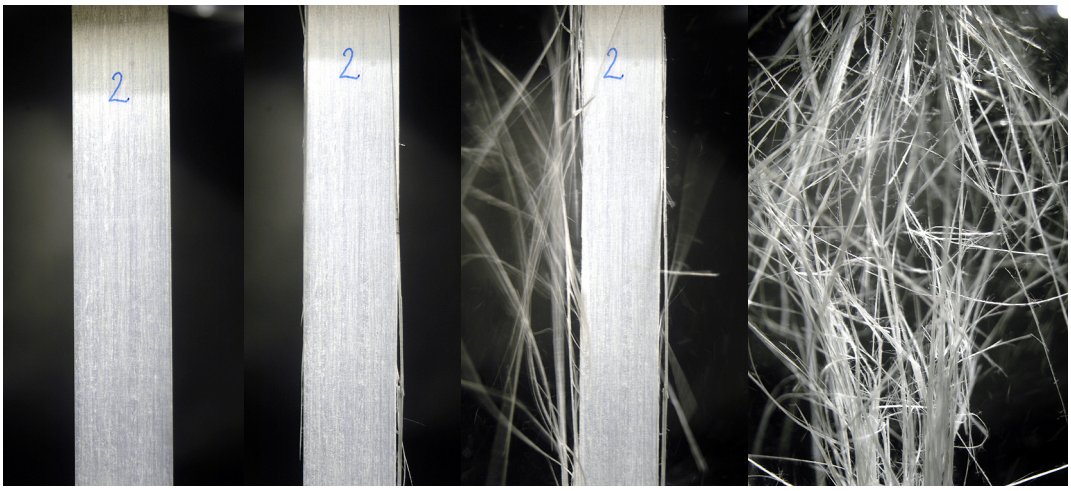

Figure 3.5: Photographs of typical failure sequence from quasi-static tension tests of S-2/BT250E-1 $[0]_2$ specimens.

The same tension tests were conducted on $[0]_2$ specimens created from material from roll two as well. The results are provided in Table 3.4 and Figure 3.6. The tests concluded that the average ultimate tensile strength was 1621.50 MPa, and the Young's Modulus was 47.80 GPa. These values once again are in agreement with those provided by Bryte. The average fiber volume fraction of the panel used to create the test specimens was 52%.

Table 3.4: Results from quasi-static tension tests of S-2/BT250E-1 $[0]_2$ specimens from roll two material.

Sample	Max Tensile Stress (MPa)	Average Max Tensile Stress (MPa)	Standard Deviation	Coefficient of Variation (%)	E (GPa)	Max Deformation (%)
1	1605					
2	1638					
		1621.5	23.33	1.44	47.80	5.2

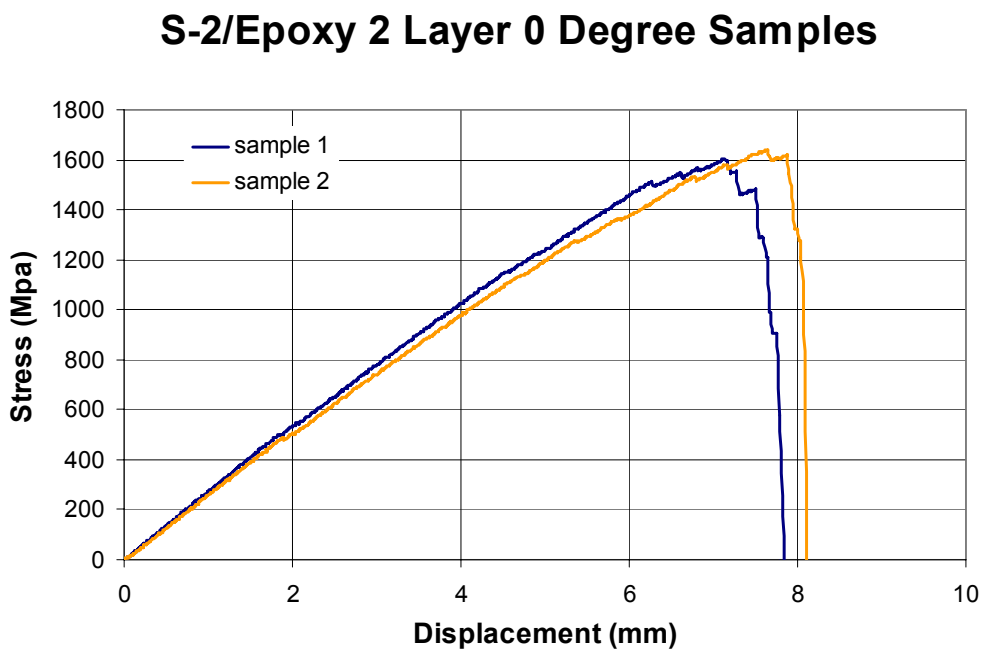

Figure 3.6: Plot of results from quasi-static tension tests of S-2/BT250E-1 $[0]_2$ specimens from roll two material.

The results from the two rolls of prepreg material are quite close. In comparing the results from the tension tests on the two rolls, the ultimate tensile strength of specimens from roll two differed by 0.83% from specimens from roll one. The Young's modulus of the specimens from roll two differed by 2.78% from the specimens from roll one. These results bode quite well for the mechanical testing as the manufactured rolls prove to be made quite uniformly from roll to roll.

Similar tests were conducted on $[90]_{12}$ specimens made from roll one material. The results are given in Table 3.5 with photographs of the typical failure sequence shown in Figure 3.7. The average maximum transverse stress was determined to be

58.17 MPa. The average fiber volume fraction of the panel used to create the test specimens was 50%.

Table 3.5: Results from quasi-static tension tests of S-2/BT250E-1 $[90]_{12}$ specimens from roll one material.

Sample	Failure Stress (MPa)	Average Failure Stress (MPa)	Standard Deviation	Coefficient of Variation (%)	Deformation (%)
4	57.7				
5	60				
6	56.8				
		58.17	1.65	2.84	0.62

Similar tests were also conducted on $[90]_{12}$ specimens made from roll two material. The results are summarized in Table 3.6. The average maximum transverse stress was determined to be 62.27 MPa. The average fiber volume fraction of the panel used to create the test specimens was 52%.

Table 3.6: Results from quasi-static tension tests of S-2/BT250E-1 $[90]_{12}$ specimens from roll two material.

Sample	Max Transverse Stress (MPa)	Average Max Transverse Stress (MPa)	Standard Deviation	Coefficient of Variation (%)	Deformation (%)
1	61.72				
3	61.53				
6	65.18				
7	61.83				
10	61.11				
		62.27	1.65	2.65	0.79

Experimentally, the transverse Young's modulus was determined to be 11.00 GPa. Theoretically, the transverse Young's modulus was determined to be 10.70 GPa.

Thus, the experimental value has a difference of merely 2.8% from the theoretical value.

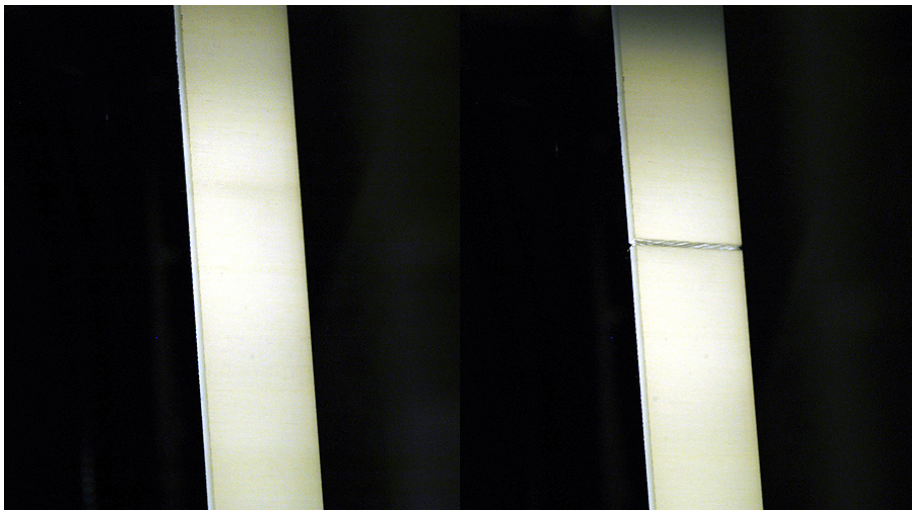

Figure 3.7: Photographs of typical failure sequence from quasi-static tension tests of S-2/BT250E-1 $[90]_{12}$ specimens.

Comparing the results from the tests involving the roll one material versus the roll two material, it is evident that the results from the roll two material are 7.04% higher when compared to the results from the roll one material.

Tension tests were also performed on $[\pm 45]_{10}$ specimens in order to determine the in-plane shear response, or the maximum in-plane shear stress, and the shear modulus. The results of the tests on the $[\pm 45]_{10}$ specimens made from the roll one material are displayed in Table 3.7 and Figure 3.8. Photographs of the typical failure sequence are shown in Figure 3.9. The specimens had an average maximum in-plane shear stress of 52.25 MPa. Through the use of strain gages, the shear modulus was

determined to be 5.40 GPa. The average fiber volume fraction of the panel used to create the test specimens was 51%.

Table 3.7: Results from quasi-static tension tests of S-2/BT250E-1 $[\pm 45]_{10}$ specimens from roll one material.

Sample	Max Tensile Stress (MPa)	Average Maximum Tensile Stress (MPa)	Standard Deviation	Coefficient of Variation (%)	Tau Max (MPa)	Average Tau Max (MPa)
1	190.08				52.41	
2	188.82				52.00	
3	190.75				52.35	
		189.88	0.98	0.52		52.25

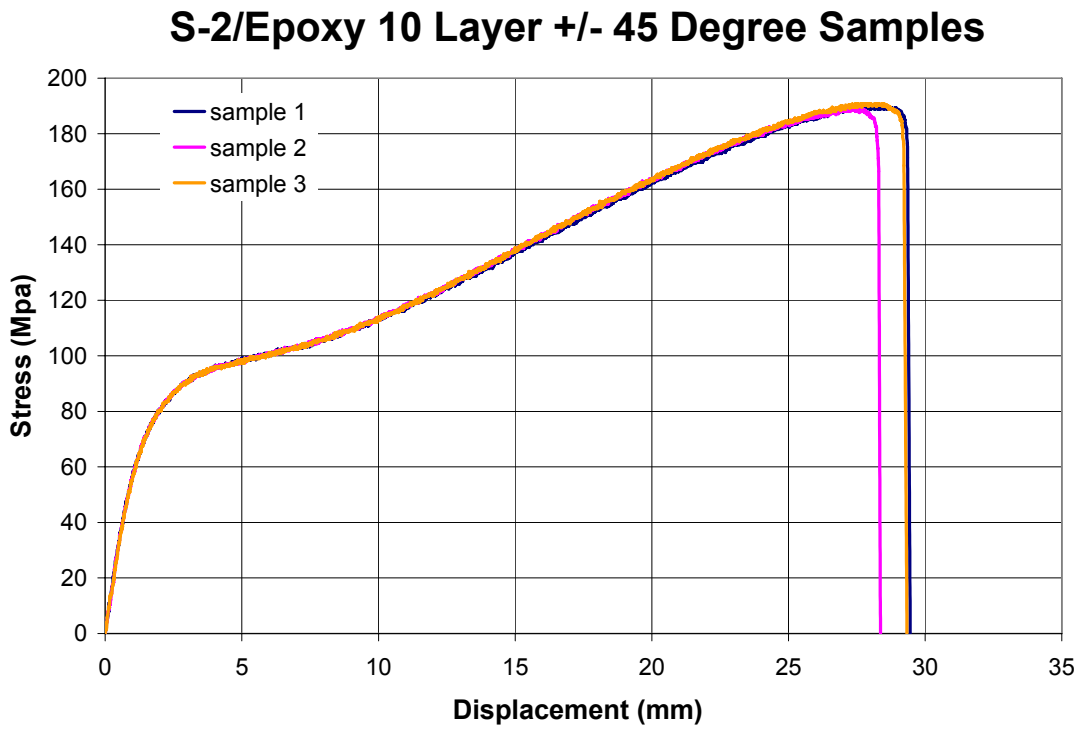

Figure 3.8: Plot of results from quasi-static tension tests of S-2/BT250E-1 $[\pm 45]_{10}$ specimens from roll one material.

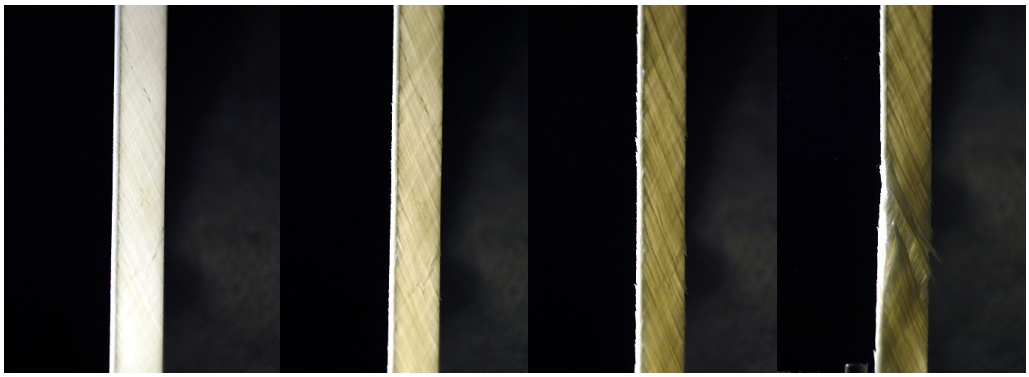

Figure 3.9: Photographs of typical failure sequence from quasi-static tension tests of S-2/BT250E-1 $[\pm 45]_{10}$ specimens.

Once again, tension tests were also performed on $[\pm 45]_{10}$ specimens made from roll two material in order to determine the in-plane shear response, or the maximum in-plane shear stress, and the shear modulus. The results of the tests on the $[\pm 45]_{10}$ specimens made from the roll two material are displayed in Table 3.8 and Figure 3.10. The specimens had an average maximum in-plane shear stress of 52.25 MPa. Through the use of strain gages, the shear modulus was determined to be 5.70 GPa. The average fiber volume fraction of the panel used to create the test specimens was 52%.

Table 3.8: Results from quasi-static tension tests of S-2/BT250E-1 $[\pm 45]_{10}$ specimens from roll two material.

Sample	Max Tensile Stress (MPa)	Average Max Tensile Stress (MPa)	Standard Deviation	Coefficient of Variation (%)	Tau Max (MPa)	Average Tau Max (MPa)
1	205.05				56.21	
2	205.31				55.77	
3	203.23				52.77	
4	206.5				56.07	
		205.02	1.35	0.66		55.20

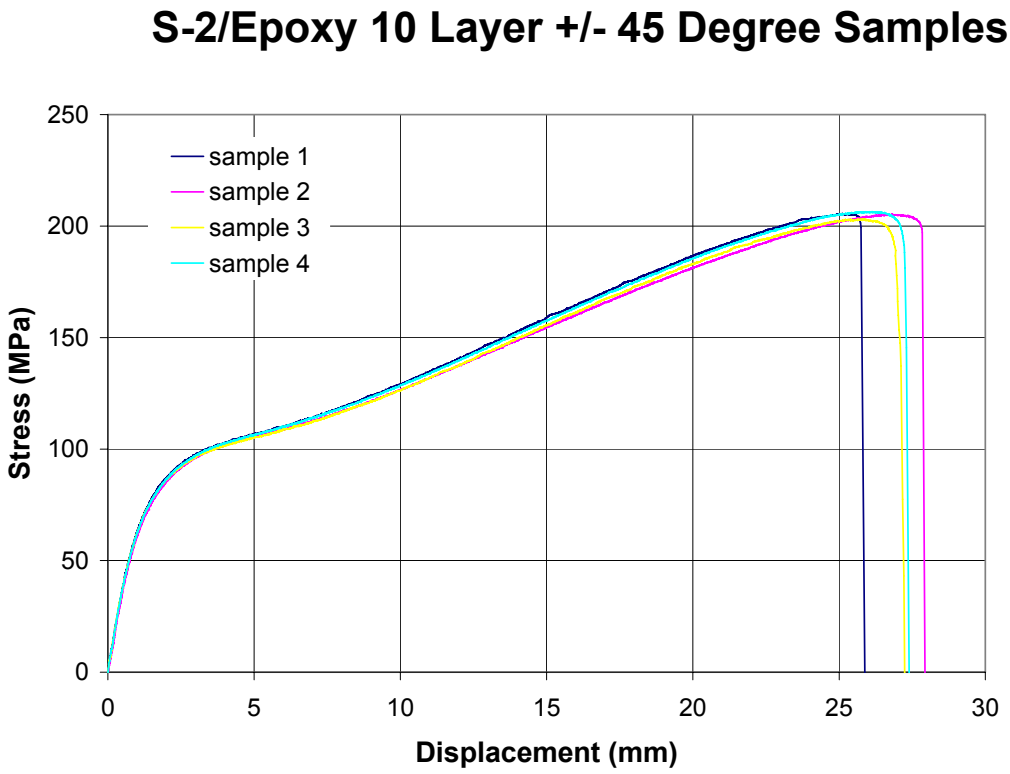

Figure 3.10: Plot of results from quasi-static tension tests of S-2/BT250E-1 $[\pm 45]_{10}$ specimens from roll two material.

In comparing the results from the tests on the roll one material and the roll two material, it can be noted that the average maximum in-plane shear stress differs by 5.6% from the roll two material as compared to the roll one material. The shear modulus also differs by 5.5% from the roll two material when it is compared to the results from the roll one material. Again, the general results between the tests on the specimens from the two different rolls are very much in agreement.

Tests were also conducted on samples with an embedded simulated microsensor placed at the midplane between layers of prepreg in a four layer test

specimen. The $[0]_4$ test specimens with the simulated microsensors embedded at the midplane were tested in the same manner as the $[0]_2$ blank test specimens. The samples were designed to be fabricated using four layers of prepreg versus the two layers used in the blank samples due to the thickness of the simulated microsensor. The results of the tension tests on the $[0]_4$ are detailed in Table 3.9 and Figure 3.11.

Table 3.9: Results from quasi-static tension tests of S-2/BT250E-1 $[0]_4$ specimens with one embedded simulated microsensor at the midplane.

Sample	Max Tensile Stress (MPa)	Average Max Tensile Stress (MPa)	Standard Deviation	Coefficient of Variation (%)
3	1570			
4	1635			
		1602.50	45.96	2.87

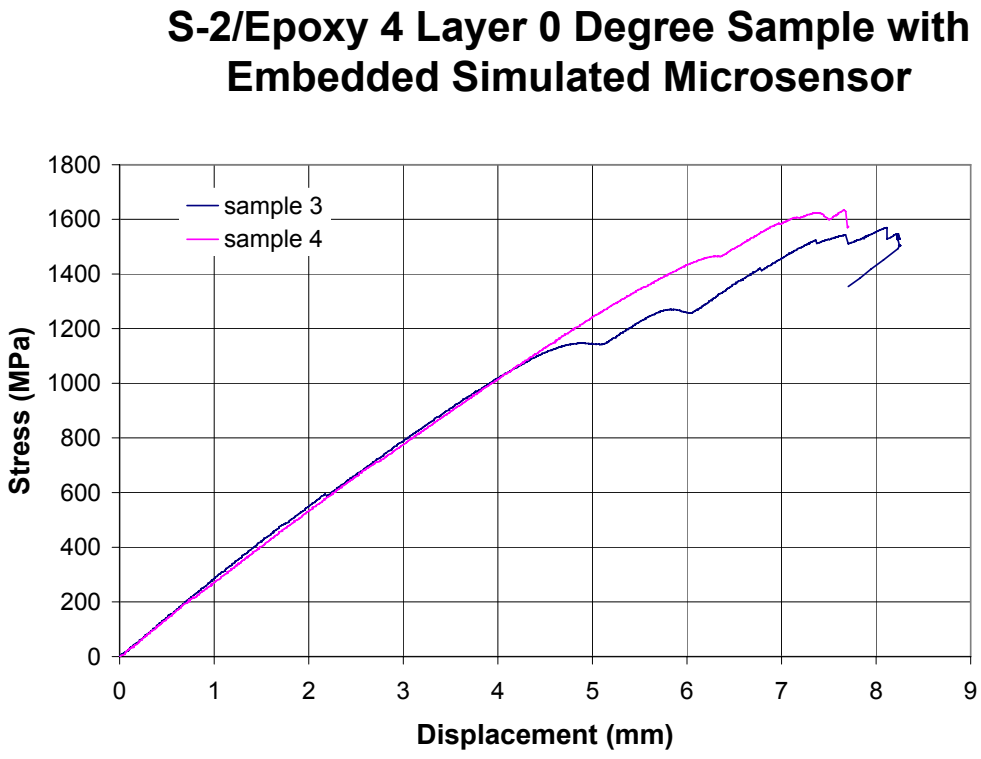

Figure 3.11: Plot of results from quasi-static tension tests of S-2/BT250E-1 $[0]_4$ specimens with one embedded simulated microsensor at the midplane.

In comparing the results from the blank $[0]_2$ specimens with the results from the $[0]_4$ with the embedded simulate microsensor it is obvious that the addition of the embedded simulated microsensor has a negligible effect upon the ultimate tensile strength of the host composite laminate. The average ultimate tensile strength of the $[0]_4$ specimen with the embedded 0805 chip resistor is well within the standard deviation of the blank specimens as evidenced by comparing the values in Table 3.9 to those of Tables 3.2 and 3.4. Photographs of the typical failure sequence of the $[0]_4$ specimen with the embedded simulate microsensor at the midplane are shown in Figure 3.12.

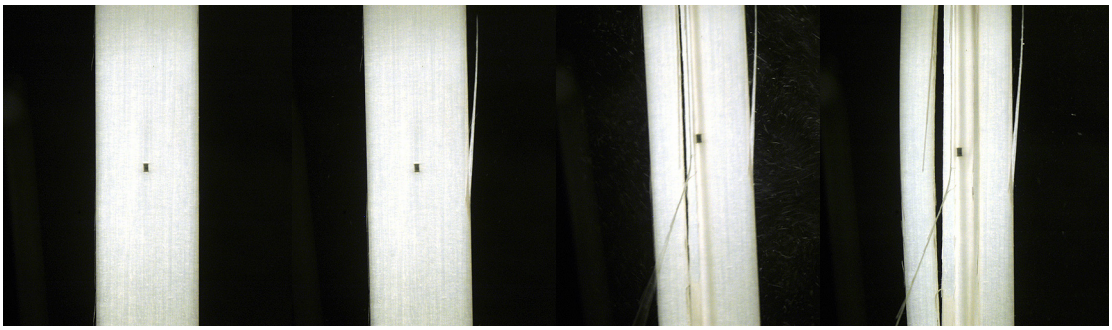

Figure 3.12: Photographs of typical failure sequence from quasi-static tension tests of S-2/BT250E-1 $[0]_4$ specimens with one embedded simulated microsensor at the midplane.

The above results indicate that in a quasi-static testing regime, the addition of the embedded sensor does not affect the longitudinal tensile strength properties, which is consistent with the literature. However, as evidenced in the photographs, the integration of the simulated microsensor did affect the failure mechanism.

Further quasi-static tests have been completed by Dr. Fabrizia Ghezzo which are not discussed here. Moreover, it is important to recognize that further testing, namely fatigue tension-tension testing which more realistically portrays an in-service loading scenario, is required in order to more fully understand the impact that the embedded microsensors may have upon the host composite material.

3.7 Summary

The results of the quasi-static tension tests provide valuable baseline values of the characteristic properties of the host composite material. The test results are consistent with the values published by the prepreg manufacturer, Bryte. The preliminary results indicate that the introduction of the simulated microsensor (0805 chip resistor) had a negligible effect upon the ultimate tensile strength of the composite material. While this result is promising, it is critical that further testing that more accurately simulates in-service loading be conducted.

3.8 Acknowledgement

I would like to express my deep gratitude to Dr. Fabrizia Ghezzo for her incredible contributions to these tensile tests. She provided an immense amount of leadership and direction. Her contributions to composite fabrication, specimen preparation, and the actual mechanical testing were critical.

Chapter 4

Three-point bending (short-beam shear) test

4.1 Introduction

In most fibrous composites, the interlaminar shear strength is considerably lower than that of the longitudinal tensile strength (Shindo et al., 2001). It is the interlaminar shear strength that often is the critical parameter. It follows that with laminated composite structures, the delamination failure mode has the potential for being the major life-limiting failure process. Thus, delamination is a fundamental issue in the evaluation of laminated composite structures for durability and damage tolerance (Whitney, 1989).

With the introduction of sensing elements into the host composite material, interlaminar stresses arise at or near the inclusions. The interlaminar stresses could result in delamination. The occurrence of delamination is problematic for several reasons. Delamination could lead to a reduction in the load carrying capability. A delamination failure between the embedded sensor and the host composite material

could cause a sensor to lose its ability to detect its surrounding environment (Shukla and Vizzini, 1996).

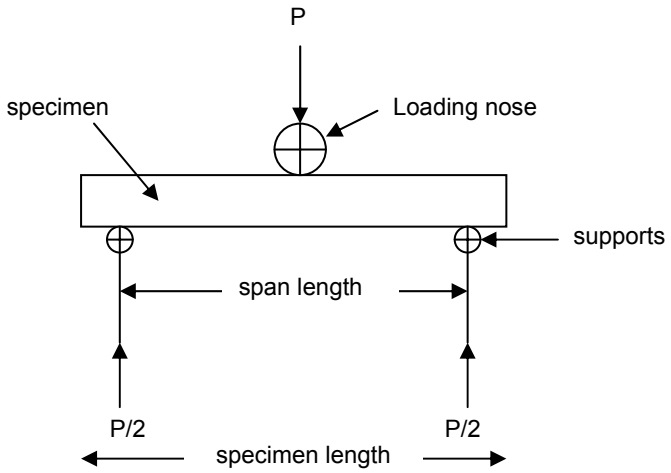

Figure 4.1: Typical three-point bending (short-beam shear) test configuration used to determine the short-beam shear strength of high-modulus fiber reinforced composite materials.

The short-beam shear test method based upon ASTM D2344 has become a widely used method for characterizing the interlaminar failure resistance of fiber reinforced composites (Shindo et al., 2001). The typical test configuration is shown in Figure 4.1.

Although editorially corrected in 2000, ASTM historically referred to it as the "apparent" interlaminar shear strength due to the highly complex stress state that exists in the short-beam shear specimen. With the complex internal stresses, although shear is the dominant applied loading, several failure modes can occur. Complications arise due to the stress distributions near the loading nose and supports which are not

predictable by classical beam theory. However, Adams and Lewis (1995) observed that the local compressive damage under the loading cylinder was a minor secondary event, if it occurred at all, and that shear (interlaminar) failure modes were typically observed in three-point bending tests. Stress analysis by Shindo et al. (2001) revealed that maximum pure shear is present on the midplane. Thus, under maximum shear stress interlaminar shear failure will initiate at the midplane. It is critical to note that unless midplane interlaminar failure has been clearly observed, the short-beam shear strength determined from this test method cannot be attributed to a shear property. Typical interlaminar failures can be seen in Figure 4.2 along with other possible failure modes including those due to flexure and inelastic deformation.

(a) Interlaminar shear failure.

(b) Flexure failure due to compressive stresses (left) and due to tensile stresses (right).

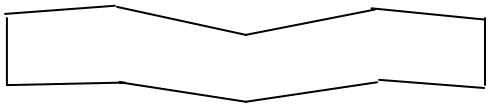

(c) Inelastic deformation.

Figure 4.2: Typical failure modes observed in the three-point bending (short-beam shear) test. (a) Interlaminar shear failure. (b) Flexure failure due to compressive stresses (left) and due to tensile stresses (right). (c) Inelastic deformation.

The classic interlaminar shear failure is defined as a shear crack at the mid-thickness of the beam propagating parallel to the axis of the beam (Adams and Lewis, 1995). The interlaminar shear strength can be defined as the resistance of a layered composite to internal forces that tend to induce relative motion parallel to, and between, the layers (Shindo et al., 2001).

Owing to the complexity of internal stresses and the variety of possible failure modes, it is generally not possible to relate the short-beam shear strength to any one material property. However, the failures are typically dominated by the resin and interlaminar properties. The test results have been found to be highly repeatable for a given specimen geometry, material system, and stacking sequence as evidenced in the results section of this work (ASTM, 2000).

In accordance with ASTM D 2344, the quasi-static three-point bending (short-beam shear) tests were conducted to characterize the short-beam shear strength of the host composite material as well as to characterize the subsequent effects of the various embedments and their embedding configurations on the short-beam shear strength.

Glass/epoxy composite materials are widely used throughout the automotive, aerospace, and aeronautic industries due to their high strength and relatively low cost. These glass/epoxy composites are routinely subjected to bending fatigue (Roudet et al., 2002). For composite structures that experience bending, the formation of matrix cracks may lead to catastrophic delamination formation and growth (O'Brien et al.,

2002). It follows that with laminated composite structures, the delamination failure mode has the potential for being the major life-limiting failure process. Thus, delamination is a fundamental issue in the evaluation of laminated composite structures for durability and damage tolerance (Whitney, 1989).

The introduction of an advanced sensing network into the composite material could prove very useful in monitoring the health of the composite. The network could provide information on the integrity of the composite material, thus preventing catastrophic failure. However, a sensor must be chosen such that it does not degrade the host composite material.

Fatigue three-point bending (short-beam shear) tests have been conducted in order to more wholly understand the in-service effects of the embedded elements on the mechanical properties of the host structural composite material. Although bending fatigue tests are not widely accepted as a standard, they are useful for research purposes because bending loads often occur with in-service loading conditions (Paepegem et al., 2004).

Based upon these studies, an optimum sensor and embedding configuration are selected for the purpose of creating a composite material with an integrated embedded sensing network to allow for structural health monitoring.

4.2 Specimen preparation

4.2.1 Specimen layup and fabrication

All of the composite panels utilized in this study were processed in a 125 ton Wabash laminating hot press according to the general manufacturer specifications detailed in Section 2.2.1 with the bagging sequence provided in Figure 2.2. More specifically, each panel consisted of twenty layers of unidirectional S-2-glass/epoxy prepreg with some containing the additional embedments of sensors or simulated sensors. Due to the small nature of the short-beam shear specimen and in order to increase specimen uniformity, multiple specimen types were fabricated within the same composite panel as depicted in Figure 4.3. The quasi-static and fatigue three-point bending (short-beam shear) test specimens were created from the same composite panel. That is to say, all of sample type 1 test specimens for both the quasi-static and fatigue three-point bending (short-beam shear) tests were created within the same panel in an effort to minimize specimen variation.

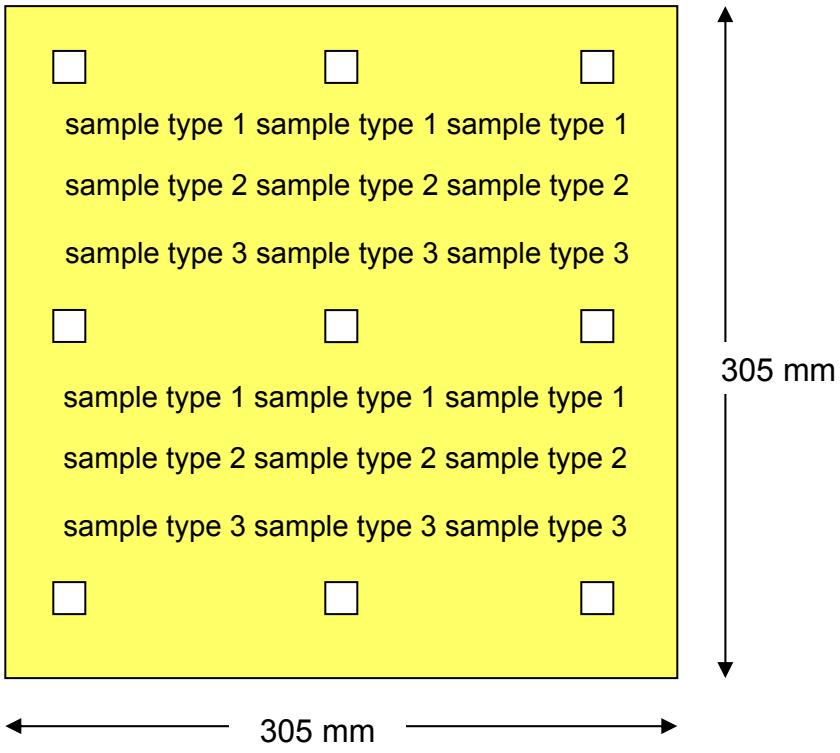

Figure 4.3: Composite panel with short-beam shear specimen layout.

4.2.2 Specimen machining

The three-point bending (short-beam shear) test specimens were extracted from the composite panels using a CNC 3-axis milling machine. The embedments were targeted and marked. The unidirectional composite panel was then clamped to an aluminum plate mounted in a vise. The panel was flooded or submerged in water in order to contain the harmful dust created by cutting the material. The specimens were machined by side milling with a 3.175 mm (0.125 in) diameter titanium nitride coated carbide four flute cutter specifically designed for cutting glass/epoxy composite materials. The cutter speed was 1200 rpm, with a feed of 203 mm per minute for rough cuts and 101.5 mm per minute for finish cuts. All cuts were done at full depth,

the thickness of the composite panel. Finally, the specimens were deburred, rinsed with water, and thoroughly dried.

4.2.3 Thickness and width measurements

The thickness of each three-point bending (short-beam shear) specimen was measured at three points along the length of the specimen using flat nose digital calipers. The average of these measurements was determined and used in calculations.

4.3 Specimen configurations

Each specimen consisted of twenty layers of S-2-glass/epoxy prepreg, with the fiber direction of each ply coinciding with the span direction of the beam, thus far exceeding the ASTM prescribed 10% fiber minimum in the span direction. Being purely unidirectional laminates, the specimens were both balanced and symmetric with respect to the span direction of the beam. The specimen geometry is governed by the following equations:

$$Specimen\ length = thickness \times 6 \tag{4.1}$$

$$Specimen\ width = thickness \times 2.0 \tag{4.2}$$

Per ASTM, the test method is limited to test specimens maintaining a minimum thickness of 2.0 mm, but not exceeding 6.0 mm. Analysis by Adams and Lewis (1994) indicated that using a width-to-thickness ratio that exceeds a factor of

2.0 can result in a significant shear stress variation along the width of the specimen. The typical geometry of the specimens tested in this study is detailed in Figure 4.4.

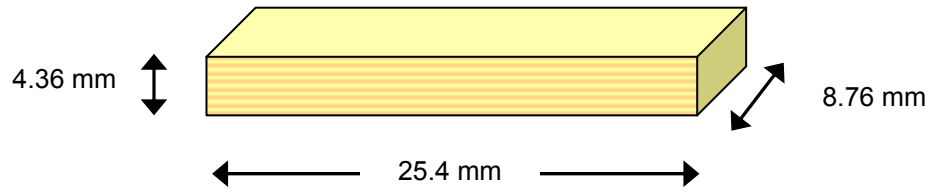

Figure 4.4: Typical geometry of the short-beam shear specimens investigated in the quasi-static three-point bending (short-beam shear) tests.

The three-point bending (short-beam shear) tests investigated eleven different specimen configurations. Independent of whether the specimen contained an embedment, all of the specimens maintained a smooth surface finish. The various specimen configurations are depicted in Figure 4.5. The blank specimens consisted solely of the unidirectional S-2-glass/epoxy prepreg. The G-10 specimens consisted of an entire layer of the commonly used printed circuit board material G-10/FR4 Garolite (0.18 mm thick) at the midplane. Specimens that contained two 0805 chip resistors to simulate embedded microsensors at the mid-plane placed between the layers of prepreg (hereafter referred to as **embedded sensor specimen**) were also created. Specimens that contained two 0805 chip resistors to simulate embedded microsensors at the mid-plane placed within precision punched layers of prepreg (hereafter referred to as **punched sensor specimen**) were created in order to avoid the eye shaped resin pockets and fiber distortion associated with the embedded sensor

specimens. In both sensor specimen configurations, the simulated microsensors were located equidistant from the loading nose and supports.

The first type of PVDF specimen consisted of an entire layer of PVDF sensor with silver ink metallization and an acrylic screen printed protective coating (hereafter referred to as **PVDF protective coating midplane specimen**). Due to lackluster results caused by poor bonding between the epoxy and the protective coating all successive PVDF specimen configurations utilized PVDF consisting solely of the piezo film and metallization. New specimens were fabricated that contained entire layers of PVDF sensors with silver ink and nickel copper alloy metallization at the midplane (hereafter referred to as **PVDF Ag-ink/Ni-Cu midplane specimen**). The PVDF sensors were placed in a sandwich configuration between the first and second as well as the nineteenth and twentieth layers of prepreg (hereafter referred to as **PVDF Ag-ink/Ni-Cu sandwich specimens**). Finally, a PVDF sensor specimen was created that contained a more representative area of the PVDF sensor placed at the midplane of the specimen (hereafter referred to as **PVDF Ag-ink/Ni-Cu representative area midplane specimen**). The PVDF sensor at the midplane of the representative area specimens measured 12.7 mm long by 6.35 mm wide.

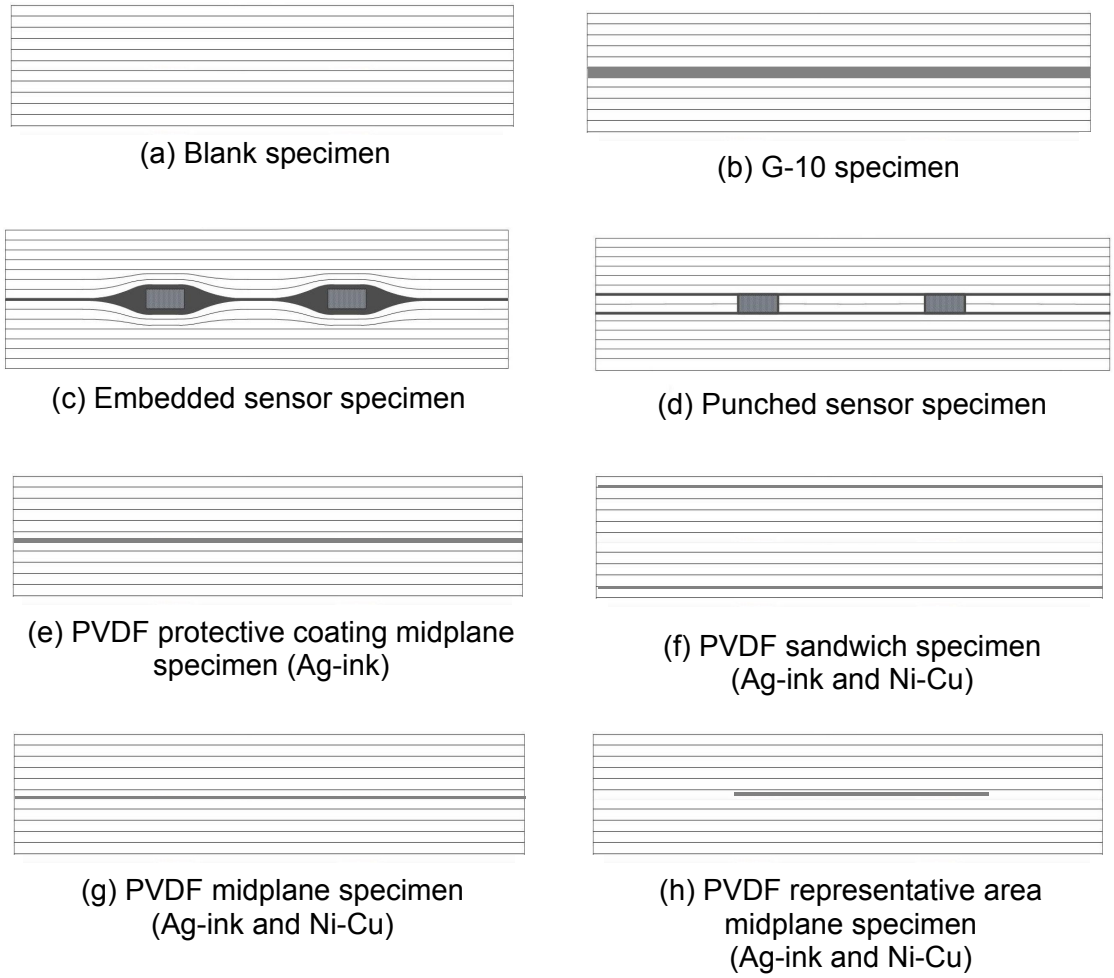

Figure 4.5: Specimen configurations for three-point bending (short-beam shear) tests. (a) Blank specimen. (b) G-10 specimen. (c) Embedded sensor specimen. (d) Punched sensor specimen. (e) PVDF protective coating midplane specimen (Ag-ink). (f) PVDF sandwich specimen (Ag-ink and Ni-Cu). (g) PVDF midplane specimen (Ag-ink and Ni-Cu). (h) PVDF representative area midplane specimen (Ag-ink and Ni-Cu).

4.4 Testing equipment and test configuration

The three-point bending (short-beam shear) tests were performed using an MTS model 309.20 load frame with an MTS model 490.05B unit controller. The load frame was equipped with a 22.2 kN (5000 lb) load cell. Additionally, the load frame

was outfitted with a three-point bending fixture, shown in Figure 4.6, manufactured by Wyoming Test Fixtures, Inc. The test fixture consists of individual upper and lower supports kept in proper alignment through two linear bearings. The loading nose cylinder has a 6.00 mm diameter, while the support cylinders each maintain a 3.00 mm diameter. All cylinders had a hardness within the range of 60 to 62 HRC and were free to rotate. The three-point bending (short-beam shear) tests were performed with a bottom span length of 17.42 mm, with a span-to-specimen thickness ratio of 4.0, all in accordance with ASTM D 2344.

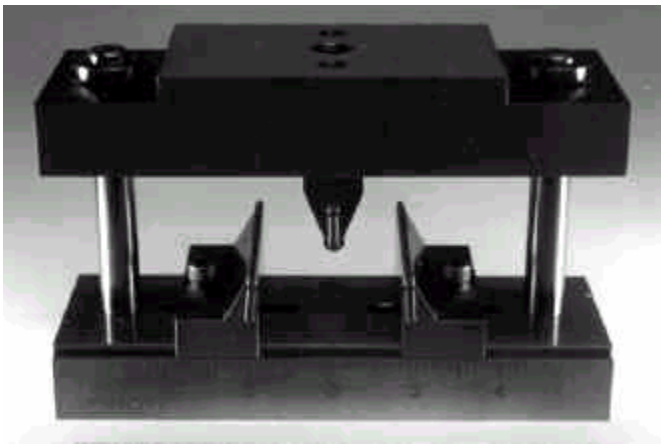

Figure 4.6: Three-point bending (short-beam shear) test fixture manufactured by Wyoming Test Fixtures, Inc.

4.5 Experimental procedure

4.5.1 Quasi-static three-point bending (short-beam shear)

The quasi-static three-point bending (short-beam shear) tests were performed in displacement control, at ambient laboratory conditions. The crosshead movement

was at a rate of 1.25 mm/min (0.05 in/min). The specimens were centrally aligned on the supports using a custom machined specimen alignment guide. The test proceeded until one of the following events occurred: a load drop-off of 30%, complete two-piece specimen failure, or travel of the loading head exceeding the nominal specimen thickness. Per ASTM, a minimum of five specimens, but typically six specimens of each configuration, were tested.

The short beam shear strength is determined using the following equation, as given in ASTM D 2344:

$$F_{SBS} = \frac{0.75P_m}{bh} \tag{4.3}$$

where F_{SBS} (MPa) is the short-beam shear strength, P_m (N) is the maximum load observed during test, b (mm) is the measured specimen width, and h (mm) is the measured specimen thickness.

4.5.2 Fatigue three-point bending (short-beam shear) test

The fatigue three-point bending (short-beam shear) tests have been conducted in order to more wholly understand the in-service effects of the embedded elements on the mechanical properties of the host structural composite material. Each specimen configuration had a complete sampling of twelve specimens tested. The tests were performed in the same MTS universal testing machine as the quasi-static tests, under

load control and at ambient laboratory conditions. The specimens were centrally aligned on the supports using a custom machined specimen alignment guide.

The specimens were cyclically loaded between 222 N (50 lb) and 2224 N (500 lb) using a sinusoidal input wave function at a frequency of 10 Hz. The cyclic loads correspond to 6% and 60% of the short beam shear strength of the blank specimens, respectively. Thus, the stress ratio was equal to 0.1 which is typical of aircraft component fatigue testing. This frequency led to a temperature increase of less than 5˚C, which is significantly lower than the maximum of 10˚C recommended by Sims and Gladman (1982) for not disrupting the material behavior.

With the fatigue three-point bending (short-beam shear) test specimen constantly under load, specimen chatter or drifting was not problematic. Furthermore, with the loading nose constantly in contact with the test specimen, any impact reaction during the fatigue testing was eliminated (Chen and Matthews, 1994). The specimens were centrally aligned on the supports and such that the unidirectional fibers were oriented along the span of the fixture. The fatigue tests were carried out until specimen failure, indicated by interlaminar cracks and the modulus of the specimen decreasing to the point that specimen triggered displacement interlocks at 2.54 mm.

4.6 Experimental results and discussion

4.6.1 Quasi-static three-point bending (short-beam shear) test

The blank specimens, G-10 specimens, and embedded sensors specimens were created in the same composite panel in order to promote specimen uniformity. That panel had an average fiber volume fraction of 51.23%.

The quasi-static three-point bending (short-beam shear) tests concluded that the average short-beam shear strength of the blank specimens was 72.96 MPa. The results from the blank specimens are detailed in Table 4.1. Photographic results indicating classic interlaminar shear failure are shown in Figure 4.7.

Table 4.1: Quasi-static three-point bending (short-beam shear) test results for blank specimens from a composite panel with an average fiber volume fraction of 51.23%.

Sample	Short Beam Shear Strength (MPa)	Average Short Beam Shear Strength (MPa)	Standard Deviation	Coefficient of Variation (%)
SBSB1	72.70			
SBSB2	73.68			
SBSB3	72.90			
SBSB4	72.66			
SBSB5	72.75			
SBSB6	73.08			
		72.96	0.38	0.53

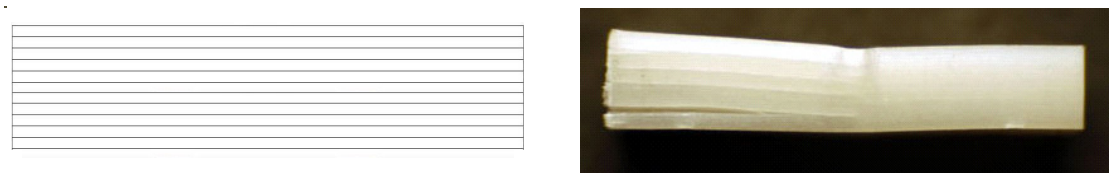

Figure 4.7: Diagram of blank specimen with photograph of interlaminar shear failure in quasi-static three-point bending (short-beam shear) blank test specimen.

The quasi-static three-point bending (short-beam shear) tests concluded that the average short-beam shear strength of the G-10 specimens was 73.67 MPa. The results from the G-10 specimens are detailed in Table 4.2. Photographic results indicating classic interlaminar shear failure are shown in Figure 4.8.

Table 4.2: Quasi-static three-point bending (short-beam shear) test results for G-10 specimens from a composite panel with an average fiber volume fraction of 51.23%.

Sample	Short Beam Shear Strength (MPa)	Average Short Beam Shear Strength (MPa)	Standard Deviation	Coefficient of Variation (%)
SBSG1	73.71			
SBSG2	73.91			
SBSG3	73.75			
SBSG4	73.11			
SBSG5	73.63			
SBSG6	73.91			
		73.67	0.30	0.40

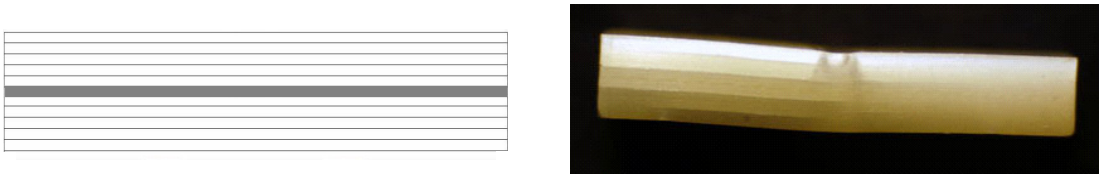

Figure 4.8: Diagram of G-10 specimen with photograph of interlaminar shear failure in quasi-static three-point bending (short-beam shear) G-10 test specimen.

The quasi-static three-point bending (short-beam shear) tests concluded that the average short-beam shear strength of the embedded sensor specimens was 71.45 MPa. The results from the embedded sensor specimens are detailed in Table 4.3.

Photographic results indicating classic interlaminar shear failure are shown in Figure 4.9.

Table 4.3: Quasi-static three-point bending (short-beam shear) test results for embedded sensor specimens from a composite panel with an average fiber volume fraction of 51.23%.

Sample	Short Beam Shear Strength (MPa)	Average Short Beam Shear Strength (MPa)	Standard Deviation	Coefficient of Variation (%)
SBSS1	71.00			
SBSS2	71.78			
SBSS3	70.53			
SBSS4	71.70			
SBSS5	71.07			
SBSS6	72.61			
		71.45	0.74	1.03

.

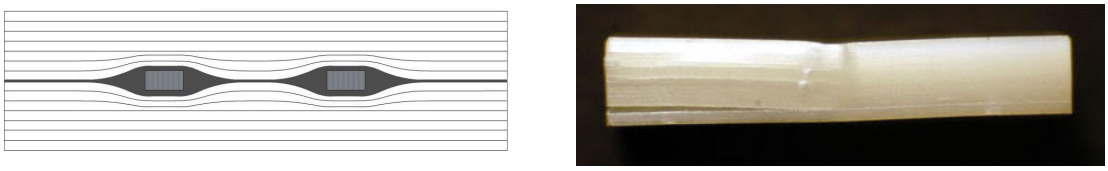

Figure 4.9: Diagram of embedded sensor specimen with photograph of interlaminar shear failure in quasi-static three-point bending (short-beam shear) embedded sensor test specimen.

A second panel containing the punched sensor specimens was created. This second panel also contained blank specimens and embedded sensor specimens in order to compare the results obtained from panel to panel and to note any distinct variations. The second panel had an average fiber volume fraction of 54.04%.

The quasi-static three-point bending (short-beam shear) tests concluded that the average short-beam shear strength of the blank specimens from the second panel was 73.50 MPa. The results from the blank specimens from the second composite panel are detailed in Table 4.4.

Table 4.4: Quasi-static three-point bending (short-beam shear) test results for blank specimens from the second composite panel with an average fiber volume fraction of 54.04%.

Sample	Short Beam Shear Strength (MPa)	Average Short Beam Shear Strength (MPa)	Standard Deviation	Coefficient of Variation (%)
SBSB2_1	73.61			
SBSB2_2	74.07			
SBSB2_3	73.51			
SBSB2_4	73.10			
SBSB2_5	73.22			
SBSB2_6	73.50			
		73.50	0.34	0.46

The quasi-static three-point bending (short-beam shear) tests concluded that the average short-beam shear strength of the embedded sensor specimens from the second panel was 73.63 MPa. The results from the embedded sensor specimens from the second composite panel are detailed in Table 4.5.

Table 4.5: Quasi-static three-point bending (short-beam shear) test results for embedded sensor specimens from the second composite panel with an average fiber volume fraction of 54.04%.

Sample	Short Beam Shear Strength (MPa)	Average Short Beam Shear Strength (MPa)	Standard Deviation	Coefficient of Variation (%)
SBSE1	74.01			
SBSE2	74.64			
SBSE3	73.13			
SBSE4	73.56			
SBSE5	71.45			
SBSE6	74.96			
		73.63	1.26	1.71

The quasi-static three-point bending (short-beam shear) tests concluded that the average short-beam shear strength of the punched sensor specimens from the second panel was 73.69 MPa. The results from the punched sensor specimens from the second composite panel are detailed in Table 4.6. Photographic results indicating classic interlaminar shear failure are shown in Figure 4.10.

Table 4.6: Quasi-static three-point bending (short-beam shear) test results for punched sensor specimens from the second composite panel with an average fiber volume fraction of 54.04%.

Sample	Short Beam Shear Strength (MPa)	Average Short Beam Shear Strength (MPa)	Standard Deviation	Coefficient of Variation (%)
SBSP1	73.67			
SBSP2	74.25			
SBSP3	72.63			
SBSP4	74.71			
SBSP5	74.20			
SBSP6	72.66			
		73.69	0.87	1.18

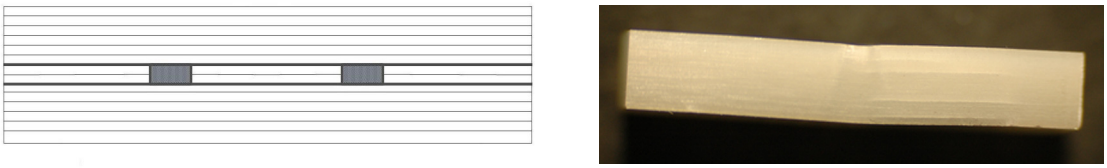

Figure 4.10: Diagram of punched sensor specimen with photograph of interlaminar shear failure in quasi-static three-point bending (short-beam shear) punched sensor test specimen made from the second composite panel.

Another composite panel containing PVDF protective coating midplane specimens (Ag-ink) had an average fiber volume fraction of 53.19%. The quasi-static three-point bending (short-beam shear) tests concluded that the average short-beam shear strength of the PVDF protective coating midplane specimens (Ag-ink) was 67.67 MPa, when considering only specimens containing the segment with the active sensing area. These results are detailed in Table 4.7. The quasi-static three-point bending (short-beam shear) tests concluded that the average short-beam shear strength of the PVDF protective coating midplane specimens (Ag-ink) was 66.44 MPa, when considering only specimens containing the segment with the offset traces. These results are detailed in Table 4.8. Photographic results indicating classic interlaminar shear failure are shown in Figure 4.11.

Table 4.7: Quasi-static three-point bending (short-beam shear) test results for PVDF protective coating midplane specimens (Ag-ink) containing the active sensor segment from the composite panel with an average fiber volume fraction of 53.19%.

Sample	Short Beam Shear Strength (MPa)	Average Short Beam Shear Strength (MPa)	Standard Deviation	Coefficient of Variation (%)
SBSVE1	64.38			
SBSVE2	69.00			
SBSVE3	69.63			
		67.67	2.87	4.24

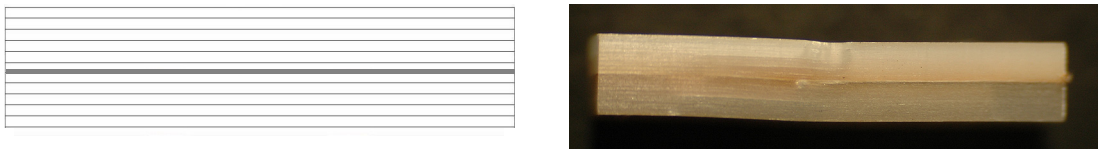

Figure 4.11: Diagram of PVDF protective coating midplane specimen (Ag-ink) with photograph of interlaminar shear failure in quasi-static three-point bending (short-beam shear) PVDF protective coating midplane specimen (Ag-ink).

Table 4.8: Quasi-static three-point bending (short-beam shear) test results for PVDF protective coating midplane specimens (Ag-ink) containing the traces segment from the composite panel with an average fiber volume fraction of 53.19%.

Sample	Short Beam Shear Strength (MPa)	Average Short Beam Shear Strength (MPa)	Standard Deviation	Coefficient of Variation (%)
SBSV1	69.44			
SBSV2	67.60			
SBSV3	65.59			
SBSV4	68.28			
SBSV5	67.69			
SBSV6	60.03			
		66.44	3.38	5.09

Another panel containing PVDF sandwich specimens (Ag-ink and Ni-Cu) and PVDF midplane specimens (Ag-ink and Ni-Cu) had an average fiber volume fraction of 53.11%. The quasi-static three-point bending (short-beam shear) tests concluded that the average short-beam shear strength of the PVDF Ag-ink sandwich specimens was 67.29 MPa. The results from the PVDF Ag-ink sandwich specimens are detailed in Table 4.9. Photographic results indicating classic interlaminar shear failure are shown in Figure 4.12.

Table 4.9: Quasi-static three-point bending (short-beam shear) test results for PVDF Ag-ink sandwich specimens from the composite panel with an average fiber volume fraction of 53.11%.

Sample	Short Beam Shear Strength (MPa)	Average Short Beam Shear Strength (MPa)	Standard Deviation	Coefficient of Variation (%)
SBSAgS1	67.41			
SBSAgS2	69.34			
SBSAgS3	67.61			
SBSAgS4	64.73			
SBSAgS5	68.52			
SBSAgS6	66.12			
		67.29	1.66	2.47

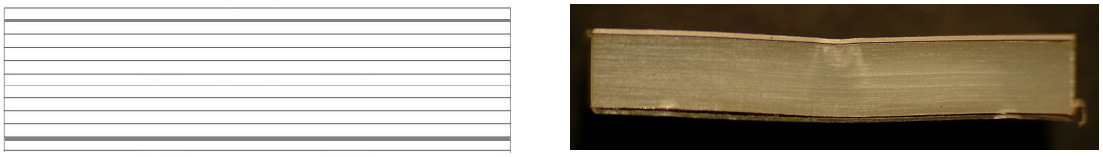

Figure 4.12: Diagram of PVDF Ag-ink sandwich specimen with photograph of interlaminar shear failure in quasi-static three-point bending (short-beam shear) PVDF Ag-ink sandwich specimen.

The quasi-static three-point bending (short-beam shear) tests concluded that the average short-beam shear strength of the PVDF Ni-Cu sandwich specimens was 68.30 MPa. The results from the PVDF Ni-Cu sandwich specimens are detailed in Table 4.10. Photographic results indicating classic interlaminar shear failure are shown in Figure 4.13.

Table 4.10: Quasi-static three-point bending (short-beam shear) test results for PVDF Ni-Cu sandwich specimens from the composite panel with an average fiber volume fraction of 53.11%.

Sample	Short Beam Shear Strength (MPa)	Average Short Beam Shear Strength (MPa)	Standard Deviation	Coefficient of Variation (%)
SBSNCS1	68.40			
SBSNCS2	66.68			
SBSNCS3	70.36			
SBSNCS4	68.26			
SBSNCS5	68.25			
SBSNCS6	67.84			
		68.30	1.19	1.75

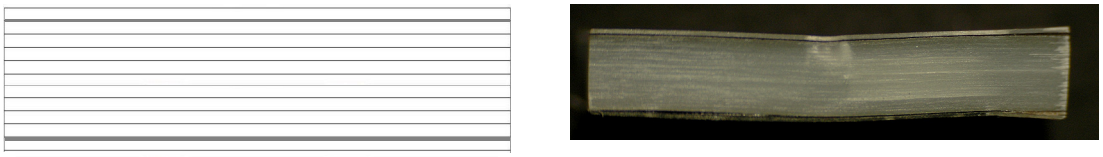

Figure 4.13: Diagram of PVDF Ni-Cu sandwich specimen with photograph of interlaminar shear failure in quasi-static three-point bending (short-beam shear) PVDF Ni-Cu sandwich specimen.

The quasi-static three-point bending (short-beam shear) tests concluded that the average short-beam shear strength of the PVDF Ag-ink midplane specimens was 64.58 MPa. The results from the PVDF Ag-ink midplane specimens are detailed in Table 4.11. Photographic results indicating classic interlaminar shear failure are shown in Figure 4.14.

Table 4.11: Quasi-static three-point bending (short-beam shear) test results for PVDF Ag-ink midplane specimens from the composite panel with an average fiber volume fraction of 53.11%.

Sample	Short Beam Shear Strength (MPa)	Average Short Beam Shear Strength (MPa)	Standard Deviation	Coefficient of Variation (%)
SBSAgM1	65.06			
SBSAgM2	63.07			
SBSAgM3	65.88			
SBSAgM4	65.77			
SBSAgM5	64.78			
SBSAgM6	62.92			
		64.58	1.30	2.01

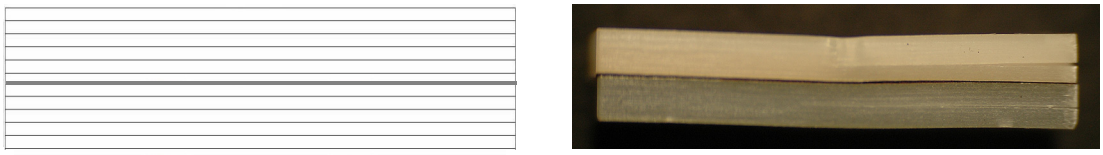

Figure 4.14: Diagram of PVDF Ag-ink midplane specimen with photograph of interlaminar shear failure in quasi-static three-point bending (short-beam shear) PVDF Ag-ink midplane specimen.

The quasi-static three-point bending (short-beam shear) tests concluded that the average short-beam shear strength of the PVDF Ni-Cu midplane specimens was 64.64 MPa. The results from the PVDF Ni-Cu midplane specimens are detailed in Table 4.12. Photographic results indicating classic interlaminar shear failure are shown in Figure 4.15.

Table 4.12: Quasi-static three-point bending (short-beam shear) test results for PVDF Ni-Cu midplane specimens from the composite panel with an average fiber volume fraction of 53.11%.

Sample	Short Beam Shear Strength (MPa)	Average Short Beam Shear Strength (MPa)	Standard Deviation	Coefficient of Variation (%)
SBSNCM1	65.29			
SBSNCM2	66.67			
SBSNCM3	63.29			
SBSNCM4	64.07			
SBSNCM5	63.87			
		64.64	1.35	2.09

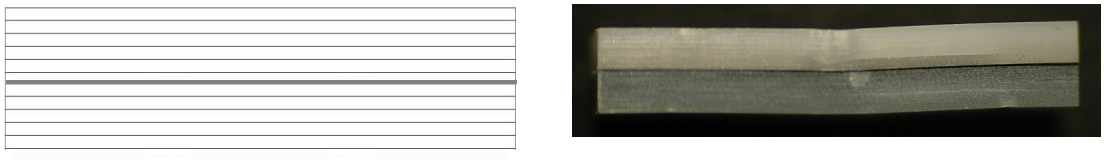

Figure 4.15: Diagram of PVDF Ni-Cu midplane specimen with photograph of interlaminar shear failure in quasi-static three-point bending (short-beam shear) PVDF Ni-Cu midplane specimen.

A final panel containing the PVDF representative area midplane specimens (Ag-ink and Ni-Cu) was fabricated and had an average fiber volume fraction of 49.05%. The quasi-static three-point bending (short-beam shear) tests concluded that the average short-beam shear strength of the PVDF Ag-ink representative area midplane specimens was 66.39 MPa. The results from the PVDF Ag-ink representative area midplane specimens are detailed in Table 4.13. Photographic results indicating classic interlaminar shear failure are shown in Figure 4.16.

Table 4.13: Quasi-static three-point bending (short-beam shear) test results for PVDF Ag-ink representative area midplane specimens from the composite panel with an average fiber volume fraction of 49.05%.

Sample	Short Beam Shear Strength (MPa)	Average Short Beam Shear Strength (MPa)	Standard Deviation	Coefficient of Variation (%)
SBSRAg1	66.81			
SBSRAg2	66.27			
SBSRAg3	66.75			
SBSRAg4	63.71			
SBSRAg5	66.64			
SBSRAg6	68.19			
		66.39	1.47	2.21

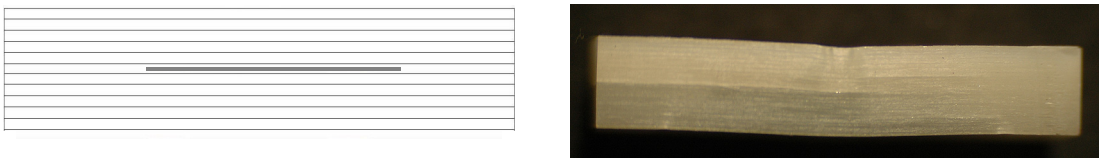

Figure 4.16: Diagram of PVDF Ag-ink representative area midplane specimen with photograph of interlaminar shear failure in quasi-static three-point bending (short-beam shear) PVDF Ag-ink representative area midplane specimen.

The quasi-static three-point bending (short-beam shear) tests concluded that the average short-beam shear strength of the PVDF Ni-Cu representative area midplane specimens was 69.51 MPa. The results from the PVDF Ni-Cu sandwich specimens are detailed in Table 4.14. Photographic results indicating classic interlaminar shear failure are shown in Figure 4.17.

Table 4.14: Quasi-static three-point bending (short-beam shear) test results for PVDF Ni-Cu representative area midplane specimens from the composite panel with an average fiber volume fraction of 49.05%.

Sample	Short Beam Shear Strength (MPa)	Average Short Beam Shear Strength (MPa)	Standard Deviation	Coefficient of Variation (%)
SBSRNC1	69.03			
SBSRNC2	69.71			
SBSRNC3	68.15			
SBSRNC4	70.58			
SBSRNC5	69.53			
SBSRNC6	70.07			
		69.51	0.85	1.22

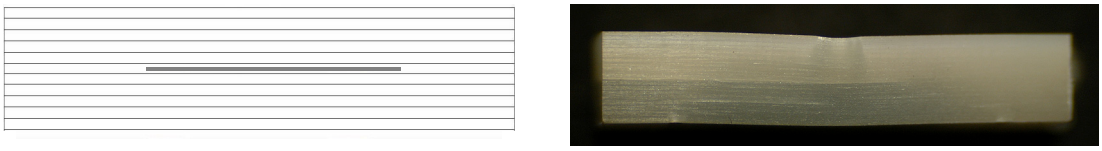

Figure 4.17: Diagram of PVDF Ni-Cu representative area midplane specimen with photograph of interlaminar shear failure in quasi-static three-point bending (short-beam shear) PVDF Ni-Cu representative area midplane specimen.

The results of the quasi-static three-point bending (short-beam shear) tests on the various specimen configurations are summarized in a plot shown in Figure 4.18, be sure to note the scale for short-beam shear strength.

Figure 4.18: Summary of quasi-static three-point bending (short-beam shear) test results for the various specimen configurations.

Quasi-static Short Beam Shear Tests

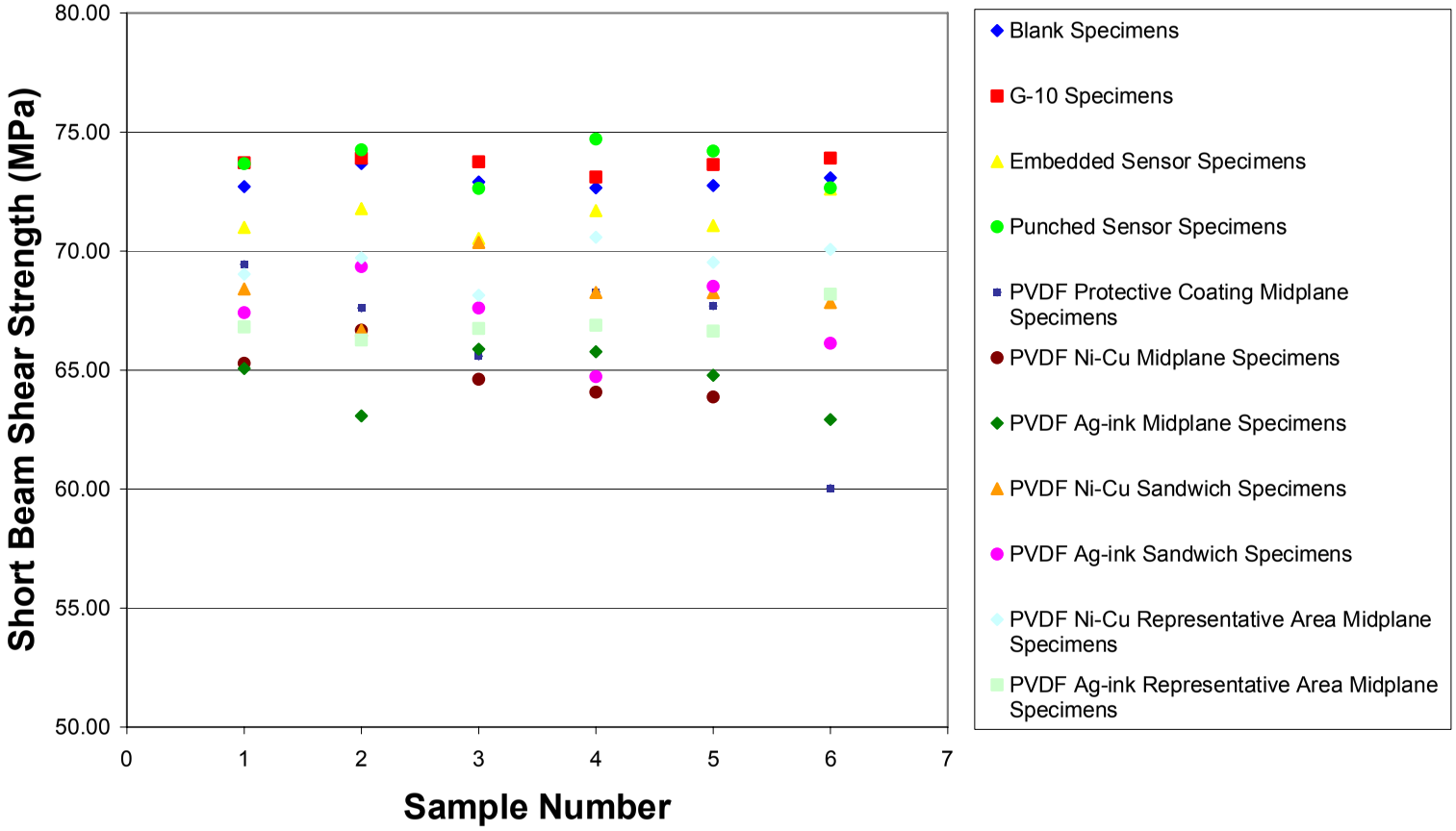

The test results have been found to be highly repeatable for a given specimen geometry, material system, and stacking sequence. Comparing the results of the blank specimens from the two different panels, it is evident that there is a great deal of uniformity from panel to panel as the difference in the average short beam shear strength is very close and nearly within the standard deviation. The slightly higher values in the blank specimens from the second panel can be attributed to the fact that the composite panel had a slightly higher fiber volume fraction by approximately 2.8%. Although the end user's fabrication process is the same for the two panels, the slight difference in fiber volume fractions is likely due to the slight variations in the rolls due to the manufacturing process. As noted on the manufacturer's certification, the percentage of resin by weight can vary up to 3% from roll to roll.

The results from the embedded sensor specimens from the two different panels were also in close agreement. The slight variations in short beam shear strength could also be attributed to the differences in the average fiber volume fraction of the composite panels.

The introduction of the entire layer of G-10 at the midplane did not affect the short beam shear strength of the host composite material. The average short beam shear strength of the G-10 specimen was within the standard deviation of the blank specimens.

When the simulated microsensors were integrated in the punched sensor specimen configuration in which the middle two plies of prepreg were precision punched, the simulated microsensors did not have an effect on the short beam shear strength.

The integration of the PVDF sensors in all configurations did slightly lower the average short beam shear strength of the test specimens, although the values were still within 10% of the short beam shear strength of the blank specimens. As previously stated, there were bonding issues between the screen printed acrylic protective coating on the original PVDF sensors and the epoxy of the host prepreg. This poor bonding could contribute to the lower average short beam shear strength that was observed. However, even in the sandwich configuration, both the Ag-ink and Ni-Cu metallizations resulted in lower average short beam shear strengths. The average short beam shear strengths were lowest for the PVDF midplane specimens, both Ag-ink and Ni-Cu. The varying coefficients of thermal expansion of the partially cured prepreg and the fully cured PVDF piezo film sensor can induce stresses along the bond site, which could results in interlaminar failure at a lower stress. Finally, the PVDF representative area specimens, both Ag-ink and Ni-Cu metallizations, displayed higher average short beam shear strengths than the PVDF midplane specimens, but were still noticeably lower than the blank specimens. The composite panel from which the PVDF representative area specimens were extracted had an average fiber volume fraction that was lower than both of the panels from which blank specimens were extracted.

The results of the quasi-static three-point bending (short-beam) tests concluded that the embedded layer of G-10/FR4 Garolite, the two 0805 chip resistors simulating microsensors embedded between layers of prepreg, and the two 0805 chip resistors simulating microsensors embedded within precision punched cut-outs in the prepreg had a negligible effect on the short beam shear strength. In general, it can be stated that all test configurations had nearly the same short beam shear strength. Therefore, further testing, namely three-point bending (short beam) fatigue tests were conducted in order in order to more conclusively understand the effect of the embedded elements on the mechanical properties of the host structural composite material.

4.6.2 Fatigue three-point bending (short-beam shear) test

As is common in fatigue testing, in all cases the scatter in fatigue lives was greater than one order of magnitude consistent with other bending fatigue testing as noted by O'Brien et al. (2002).

The results of the fatigue three-point bending (short-beam shear) tests concluded that the blank specimens had an average fatigue life of 1.71 x 10^6 cycles with a coefficient of variation of 49.20%. Interlaminar failure typical of the blank specimens is depicted in the photographic result of Figure 4.19 with the complete results given in Figure 4.20.

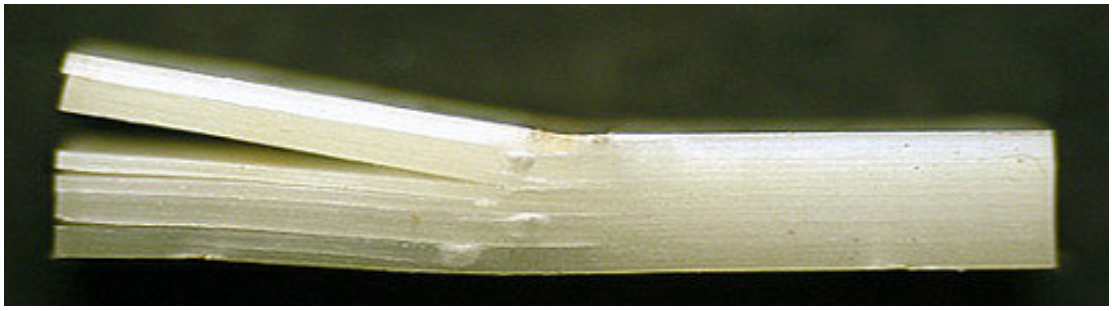

Figure 4.19: Typical interlaminar failure of blank specimen subjected to fatigue three-point bending (short-beam shear) loading.

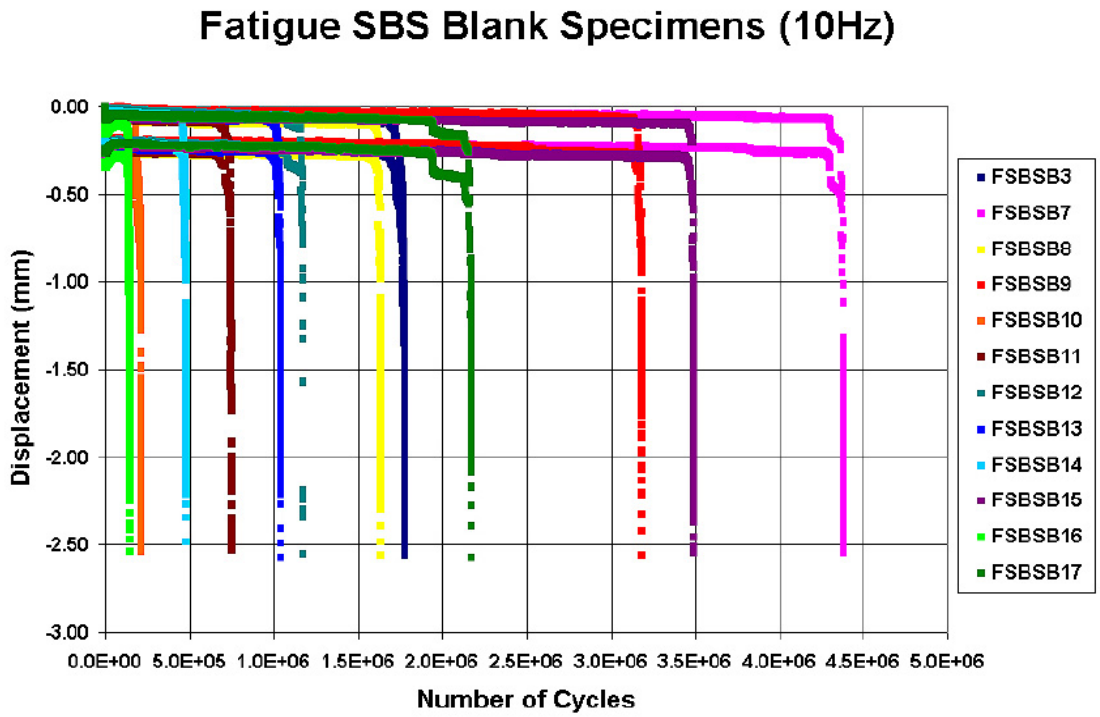

Figure 4.20: Fatigue three-point bending (short-beam shear) results for blank specimens.

The results of the fatigue three-point bending (short-beam shear) tests concluded that the G-10 specimens had an average fatigue life of 0.76 x 10^6 cycles with a coefficient of variation of 40.67%. Interlaminar failure typical of the G-10 specimens is depicted in the photographic result of Figure 4.21 with the complete results given in Figure 4.22.

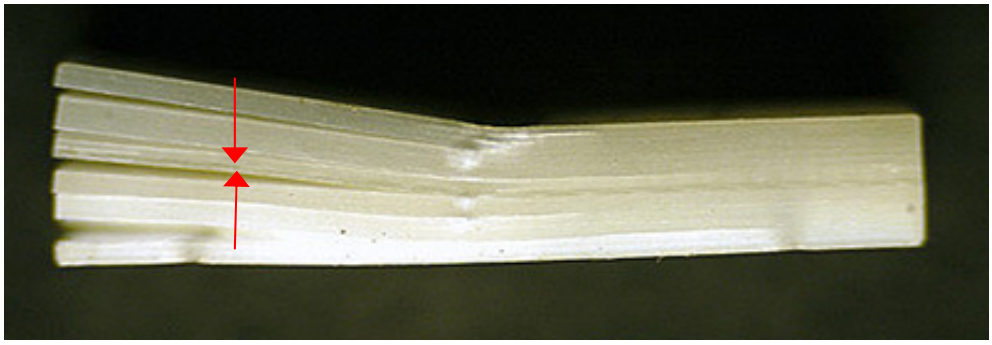

Figure 4.21: Typical interlaminar failure of G-10 specimen subjected to fatigue three-point bending (short-beam shear) loading.

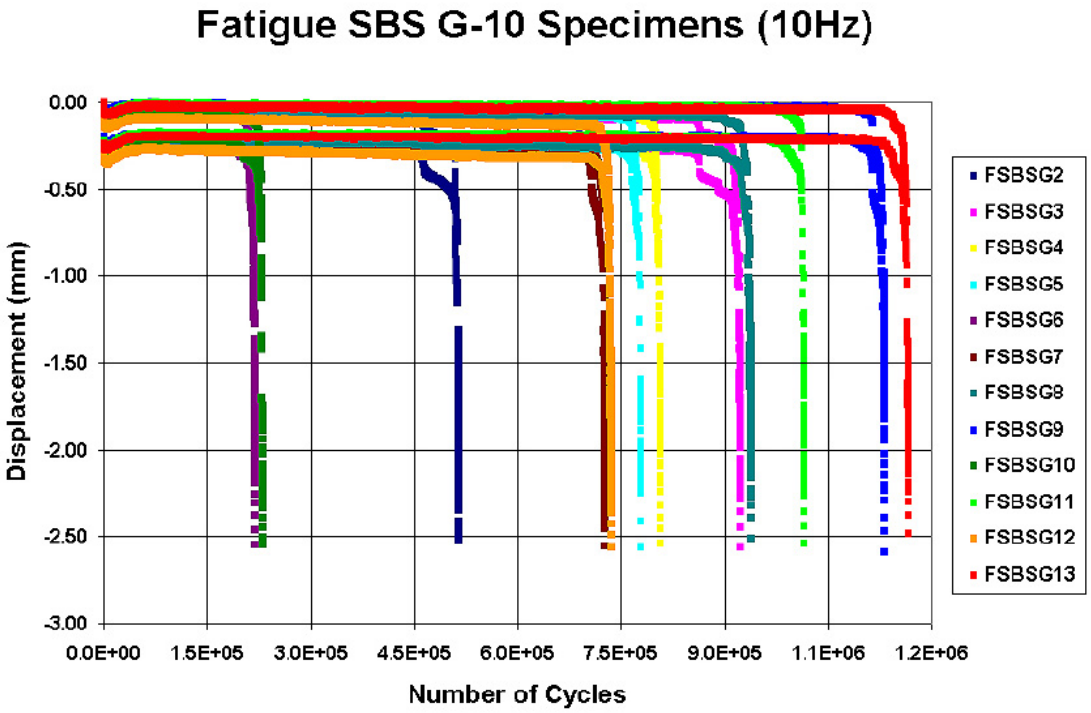

Figure 4.22: Fatigue three-point bending (short-beam shear) results for G-10 specimens.

The results of the fatigue three-point bending (short-beam shear) tests concluded that the embedded sensor specimens had an average fatigue life of 0.53 x 10^6 cycles with a coefficient of variation of 51.30%. Interlaminar failure typical of the embedded sensor specimens is depicted in the photographic result of Figure 4.23 with the complete results given in Figure 4.24.

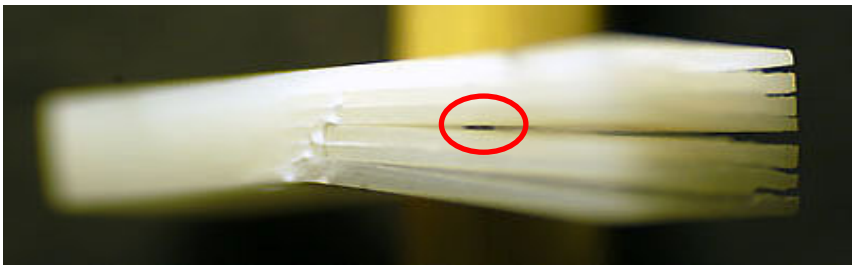

Figure 4.23: Typical interlaminar failure of embedded sensor specimen subjected to fatigue three-point bending (short-beam shear) loading.

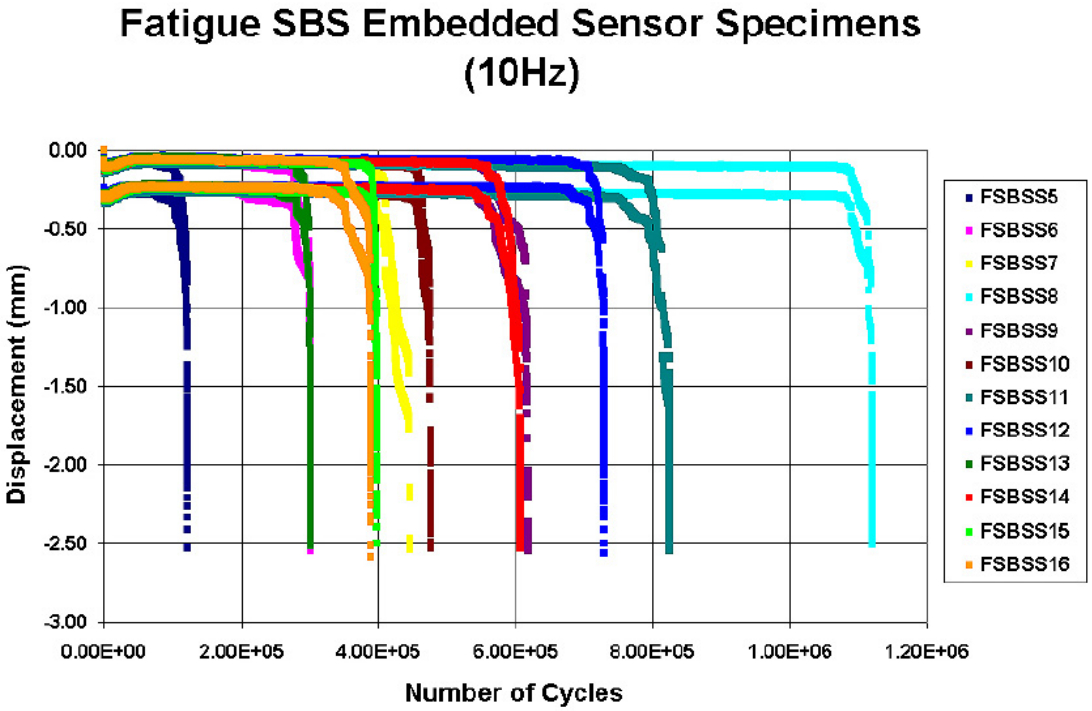

Figure 4.24: Fatigue three-point bending (short-beam shear) results for embedded sensor specimens.

The results of the fatigue three-point bending (short-beam shear) tests concluded that the punched sensor specimens had an average fatigue life of 1.44 x 10^6 cycles with a coefficient of variation of 56.89%. Interlaminar failure typical of the punched sensor specimens is depicted in the photographic result of Figure 4.25 with the complete results given in Figure 4.26.

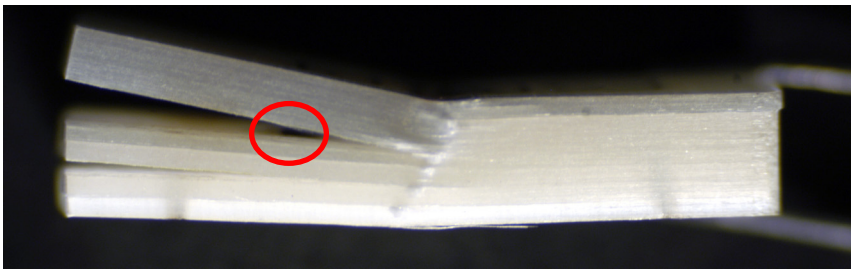

Figure 4.25: Typical interlaminar failure of punched sensor specimen subjected to fatigue three-point bending (short-beam shear) loading.

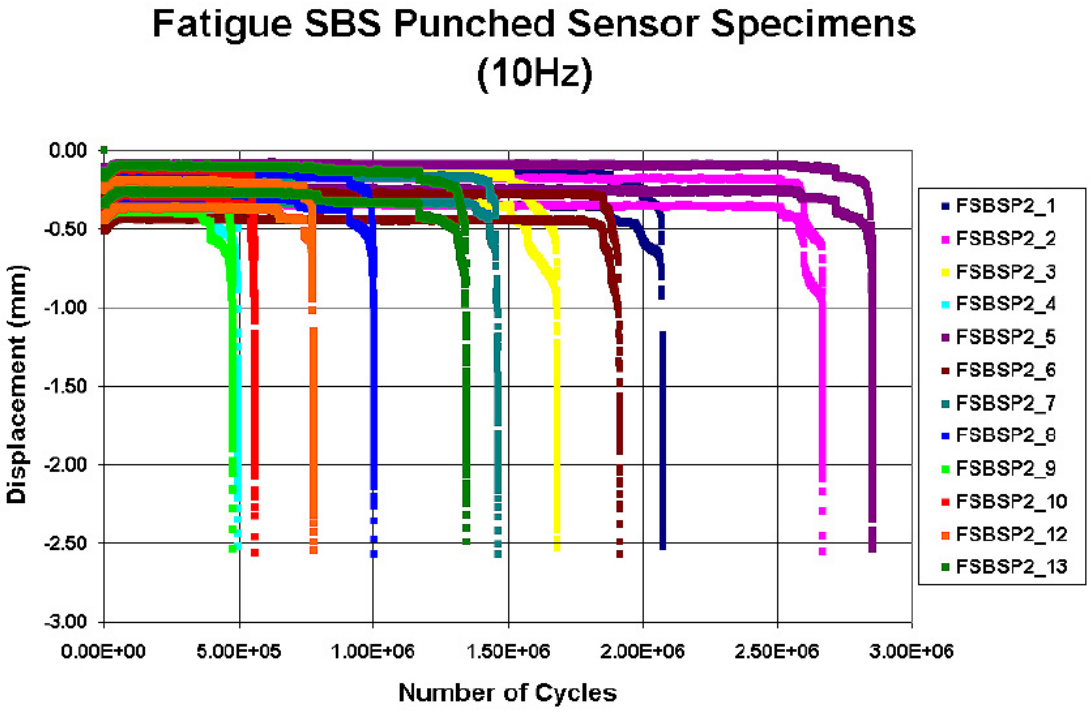

Figure 4.26: Fatigue three-point bending (short-beam shear) results for punched sensor specimens.

The results of the fatigue three-point bending (short-beam shear) tests concluded that the PVDF Ag-ink protective coating midplane specimens had an average fatigue life of 0.05 x 10^6 cycles with a coefficient of variation of 59.09%. Interlaminar failure typical of the PVDF Ag-ink protective coating midplane specimens is depicted in the photographic result of Figure 4.27 with the complete results given in Figure 4.28.

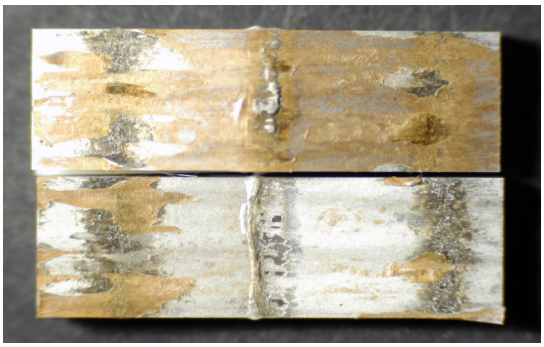

Figure 4.27: Typical interlaminar failure of PVDF Ag-ink protective coating midplane specimen subjected to fatigue three-point bending (short-beam shear) loading.

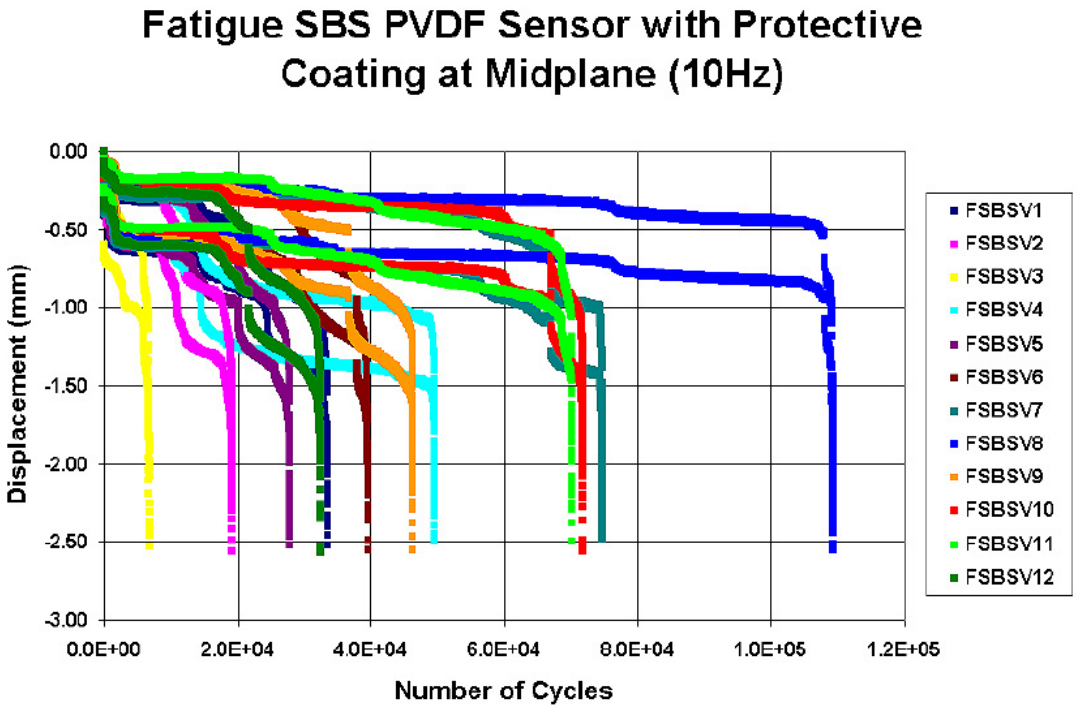

Figure 4.28: Fatigue three-point bending (short-beam shear) results for PVDF Ag-ink protective coating midplane specimens.

The results of the fatigue three-point bending (short-beam shear) tests concluded that the PVDF Ag-ink sandwich specimens had an average fatigue life of 1.06 x 10^6 cycles with a coefficient of variation of 48.41%. Interlaminar failure typical of the PVDF Ag-ink sandwich specimens is depicted in the photographic result of Figure 4.29 with the complete results given in Figure 4.30.

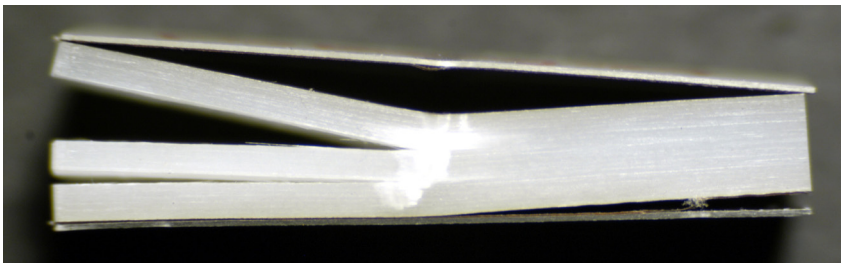

Figure 4.29: Typical interlaminar failure of PVDF Ag-ink sandwich specimen subjected to fatigue three-point bending (short-beam shear) loading.

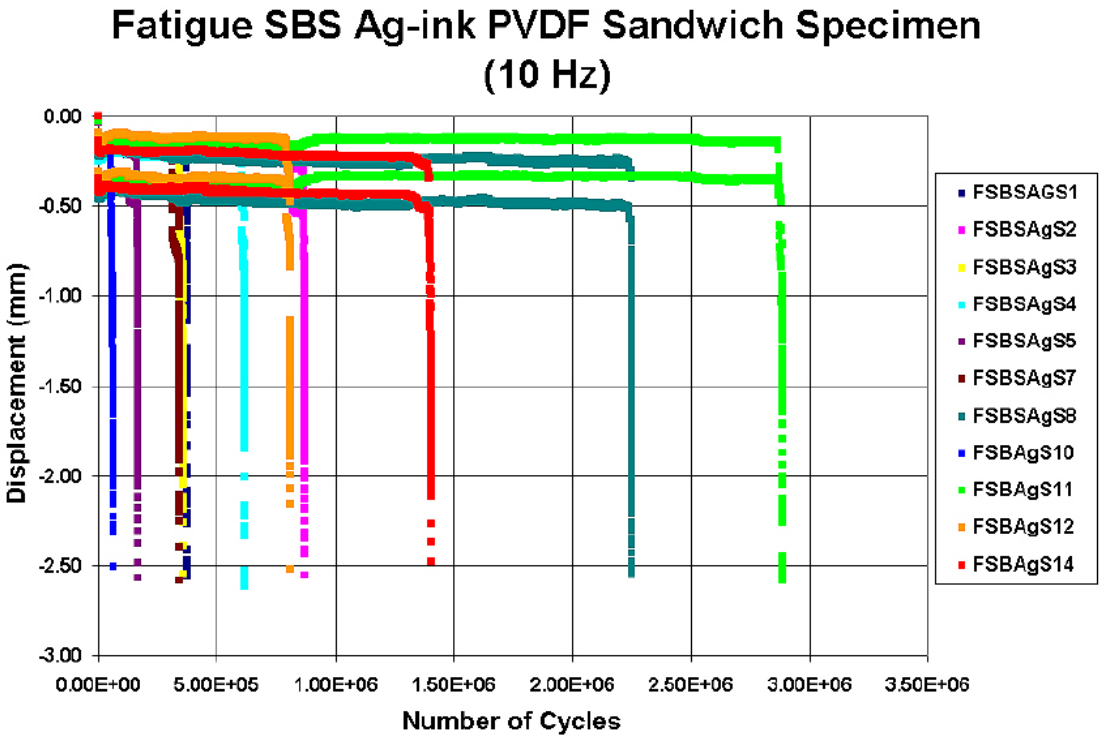

Figure 4.30: Fatigue three-point bending (short-beam shear) results for PVDF Ag-ink sandwich specimens.

The results of the fatigue three-point bending (short-beam shear) tests concluded that the PVDF Ni-Cu sandwich specimens had an average fatigue life of 1.18 x 10^6 cycles with a coefficient of variation of 40.48%. Interlaminar failure typical of the PVDF Ni-Cu sandwich specimens is depicted in the photographic result of Figure 4.31 with the complete results given in Figure 4.32.

Figure 4.31: Typical interlaminar failure of PVDF Ni-Cu sandwich specimen subjected to fatigue three-point bending (short-beam shear) loading.

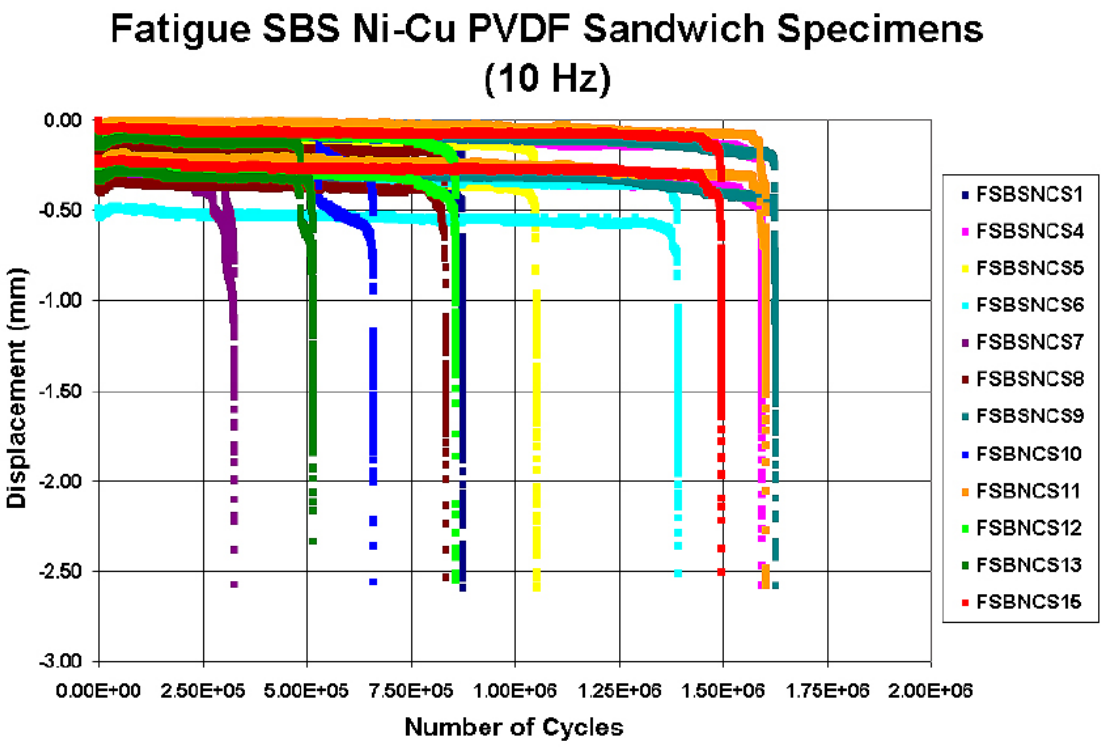

Figure 4.32: Fatigue three-point bending (short-beam shear) results for PVDF Ni-Cu sandwich specimens.

The results of the fatigue three-point bending (short-beam shear) tests concluded that the PVDF Ag-ink midplane specimens had an average fatigue life of 0.21 x 10^6 cycles with a coefficient of variation of 42.07%. Interlaminar failure typical of the PVDF Ag-ink midplane specimens is depicted in the photographic result of Figure 4.33 with the complete results given in Figure 4.34.

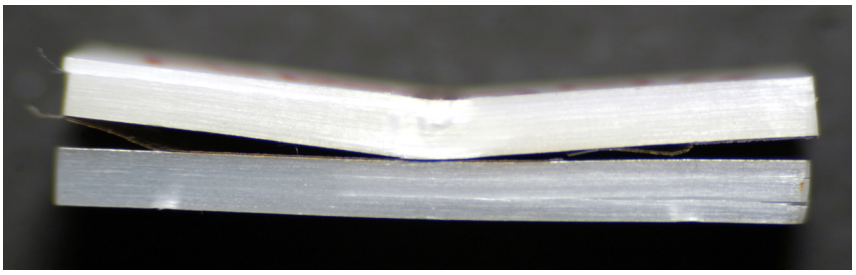

Figure 4.33: Typical interlaminar failure of PVDF Ag-ink midplane specimen subjected to fatigue three-point bending (short-beam shear) loading.

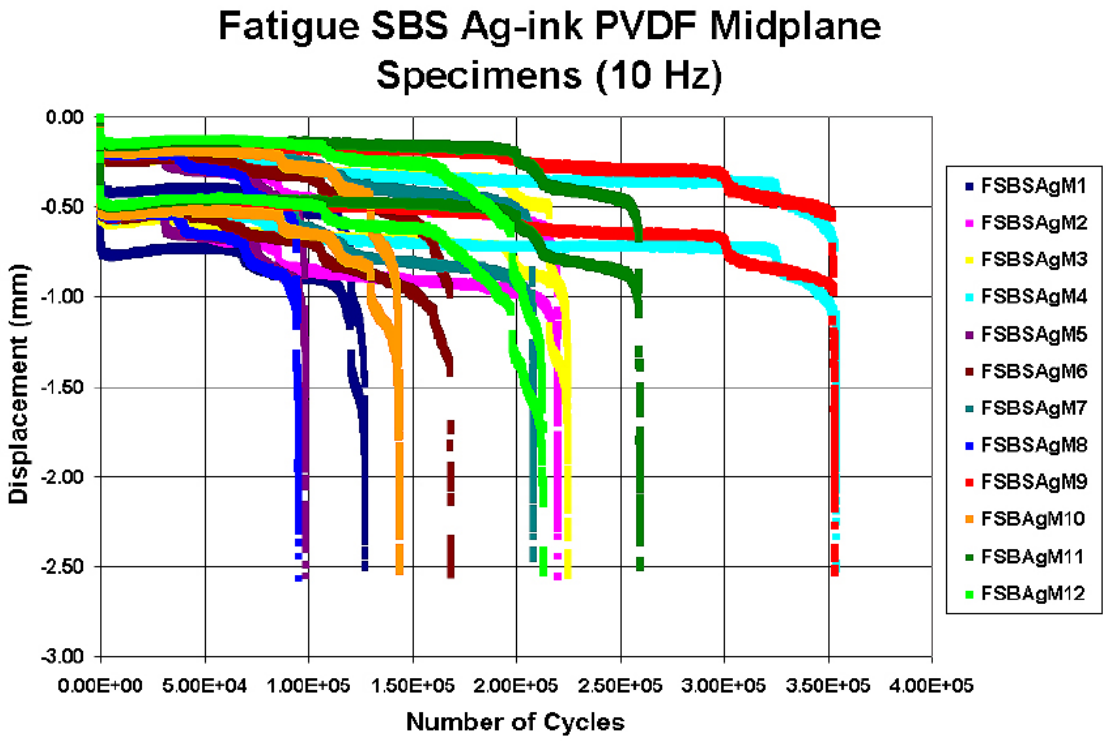

Figure 4.34: Fatigue three-point bending (short-beam shear) results for PVDF Ag-ink midplane specimens.

The results of the fatigue three-point bending (short-beam shear) tests concluded that the PVDF Ni-Cu midplane specimens had an average fatigue life of 0.56 x 10^6 cycles with a coefficient of variation of 53.99%. Interlaminar failure typical of the PVDF Ni-Cu midplane specimens is depicted in the photographic result of Figure 4.35 with the complete results given in Figure 4.36.

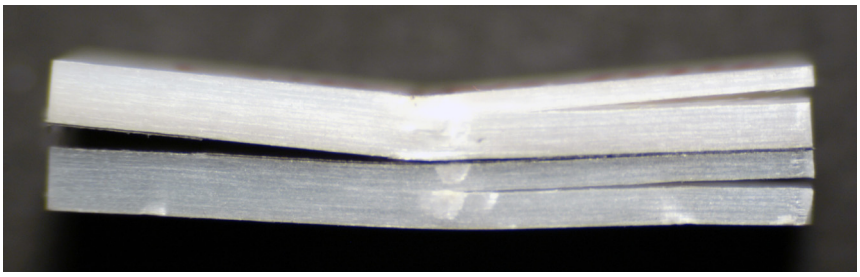

Figure 4.35: Typical interlaminar failure of PVDF Ni-Cu midplane specimen subjected to fatigue three-point bending (short-beam shear) loading.

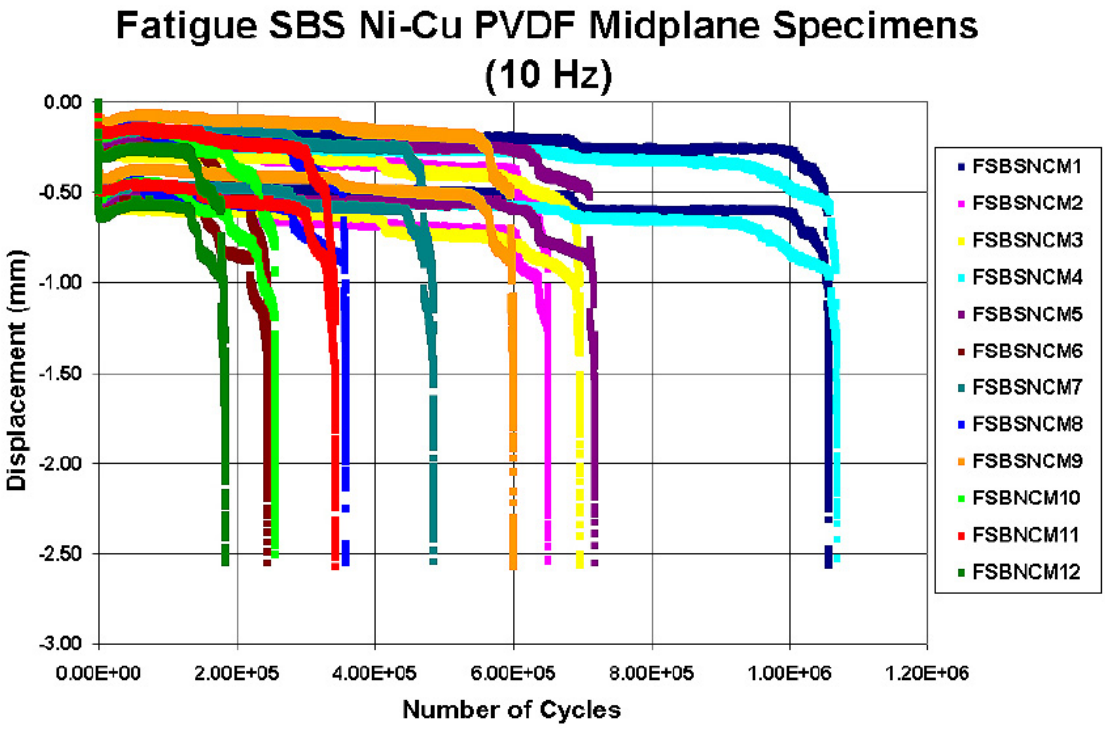

Figure 4.36: Fatigue three-point bending (short-beam shear) results for PVDF Ni-Cu midplane specimens.

The results of the fatigue three-point bending (short-beam shear) tests concluded that the PVDF Ag-ink representative area midplane specimens had an average fatigue life of 2.50 x 10^6 cycles with a coefficient of variation of 31.92%. Interlaminar failure typical of the PVDF Ag-ink representative area midplane specimens is depicted in the photographic result of Figure 4.37 with the complete results given in Figure 4.38.

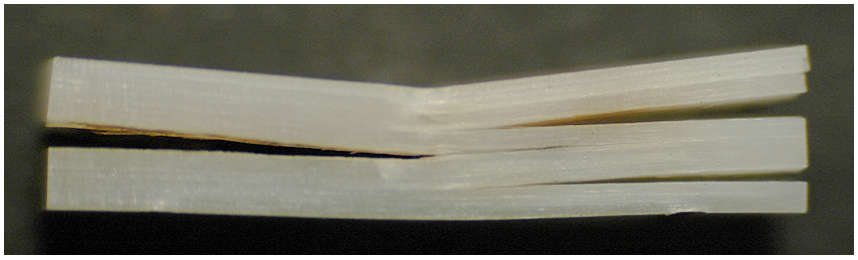

Figure 4.37: Typical interlaminar failure of PVDF Ag-ink representative area midplane specimen subjected to fatigue three-point bending (short-beam shear) loading.

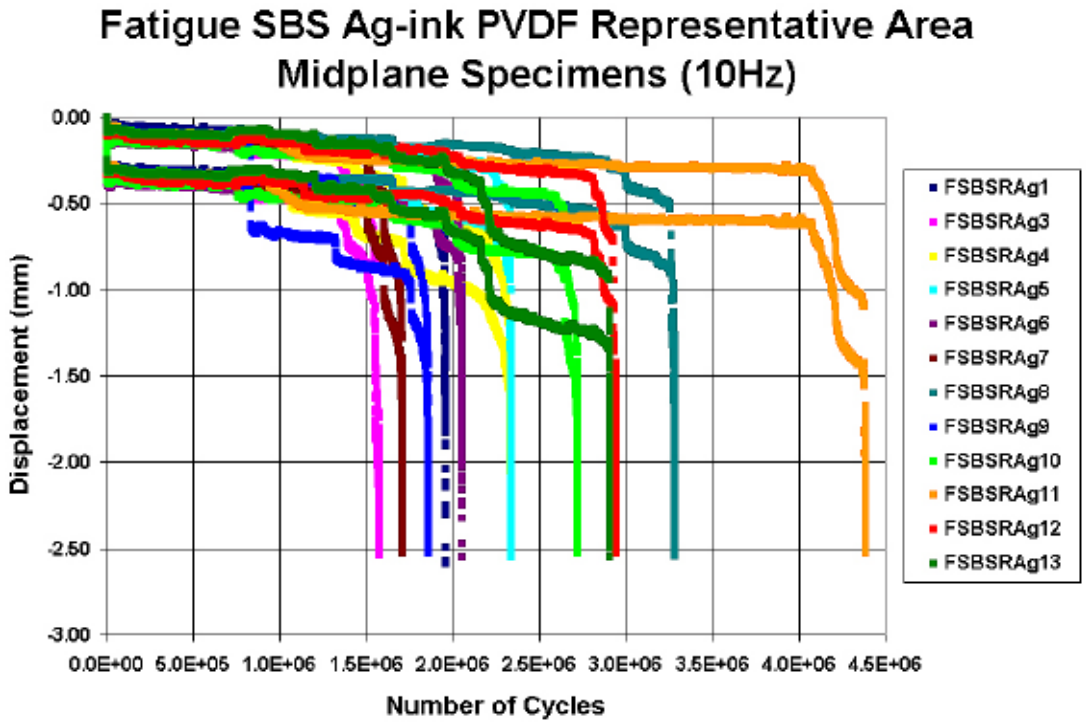

Figure 4.38: Fatigue three-point bending (short-beam shear) results for PVDF Ag-ink representative area midplane specimens.

The results of the fatigue three-point bending (short-beam shear) tests concluded that the PVDF Ni-Cu representative area midplane specimens had an average fatigue life of 1.98 x 10^6 cycles with a coefficient of variation of 61.44%. Interlaminar failure typical of the PVDF Ag-ink representative area midplane specimens is depicted in the photographic result of Figure 4.39 with the complete results given in Figure 4.40.

Figure 4.39: Typical interlaminar failure of PVDF Ni-Cu representative area midplane specimen subjected to fatigue three-point bending (short-beam shear) loading.

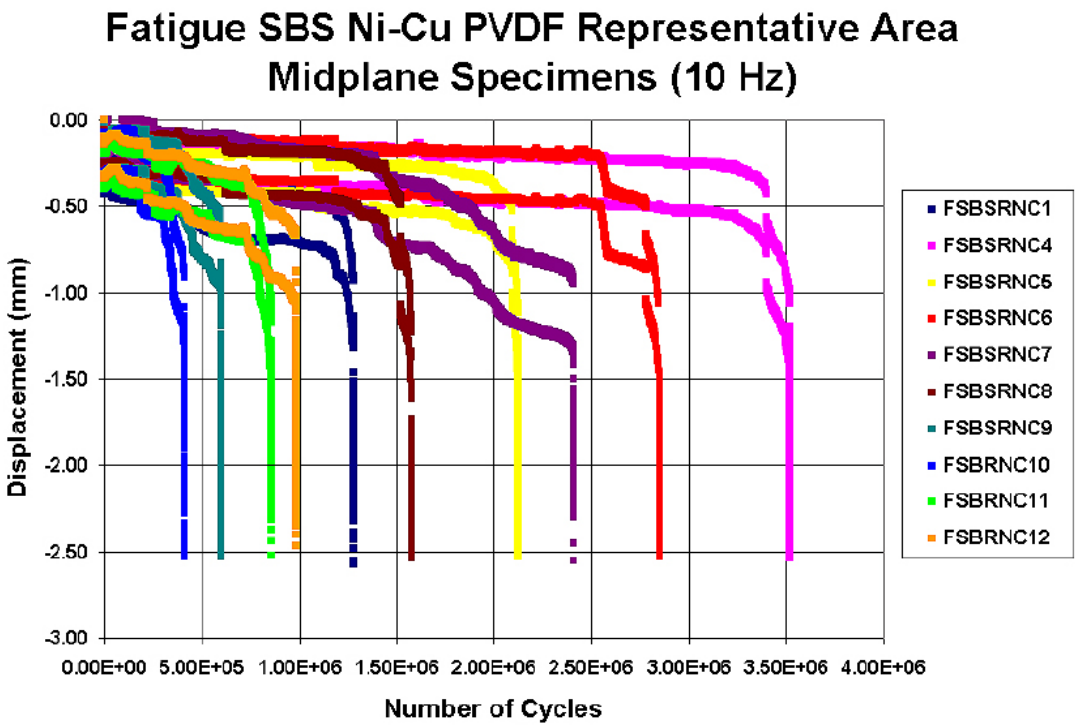

Figure 4.40: Fatigue three-point bending (short-beam shear) results for PVDF Ni-Cu representative area midplane specimens.

Table 4.15 provides a summary of the average fatigue lives of each specimen configuration along with the normalized fatigue life (as compared to that of the blank specimen configuration).

Table 4.15: Summary of fatigue three-point bending (short-beam shear) test results including average fatigue life and normalized fatigue life.

Specimen Configuration	Specimen Diagram	Average Fatigue Life	Normalized Average Fatigue Life
Blank specimen		1.71E+06	1.00
G-10 specimen		0.76E+06	0.45
Embedded sensor specimen	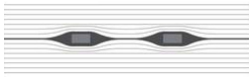	0.53E+06	0.31
Punched sensor specimen		1.44E+06	0.85
PVDF protective coating midplane specimen		4.84E+04	0.03
PVDF Ag-ink sandwich specimen		1.06E+06	0.62
PVDF Ni-Cu sandwich specimen		1.18E+06	0.69
PVDF Ag-ink midplane specimen		0.21E+06	0.12
PVDF Ni-Cu midplane specimen		0.56E+06	0.33
PVDF Ag-ink representative area midplane specimen		2.50E+06	1.46
PVDF Ni-Cu representative area midplane specimen		1.98E+06	1.16

Based upon the fatigue three-point bending (short-beam shear) test results, it is evident that the type of embedment and the method in which the sensor is integrated into the host composite material have profound effects on the fatigue life. The tests concluded that the introduction of the simulated microsensor in the embedded sensor configuration significantly decreased the average fatigue life. In fact, the resulting average fatigue life of embedded sensor specimens was less than half of the average fatigue life of the blank specimens. Through the use of precision punched prepreg in the punched sensor specimens, an average fatigue life of nearly 85% the life of the blank specimen was achieved. These results are further supported by the numerical studies performed by Mr. Yi Huang in which he determined the equivalent shear stress concentration factor. Based upon his work, it is evident that there is a correlation between the shear stress concentration factor and the fatigue life as shown in Table 4.16. The fatigue life is very sensitive to the local stress concentration introduced by the embedment.

Table 4.16: Effect of the shear stress concentration factor on the fatigue life.

	Equivalent Shear Stress Concentration factor	Normalized Fatigue life (experimental)
Blank Specimens	1.00	1.00
Punched Specimen	1.96	0.85
Embedded Specimens	3.20	0.31

Delamination along the bond site between the layer of G-10/FR4 Garolite and the prepreg could be due to the varying coefficients of thermal expansion of the

partially cured prepreg and the fully cured G-10/FR4 Garolite which can induce stresses along the bond site.

In the embedded sensor specimens, delamination at the midplane is evident as one of the two sensors embedded at the midplane becomes visible. The failure most likely initiated in the resin pocket adjacent to the embedded sensors, as this is the weakest region. The failure of the punched sensor specimen is likely to have been set in motion beginning with the resin pockets around the simulated microsensor. Although the primary motivation behind using precision punched prepreg was to eliminate the voids and resin pockets formed when the microsensor is simply placed between layers of prepreg, it is impossible to completely do so.

The introduction of the sensor into the composite creates a matrix rich region in the local area surrounding the sensor. With the matrix constituent being the weaker of the two phases, the region surrounding the sensor becomes a probable site of damage initiation. It is well known that when an optical fiber is embedded into a fiber reinforced composite, an eye shaped resin pocket usually forms due to the distortion of the neighboring fibers. Photographs (Figure 4.41) and micrographs (Figure 4.42) show that the same is true for rectangular shaped embedments when simply embedded between layers of prepreg.

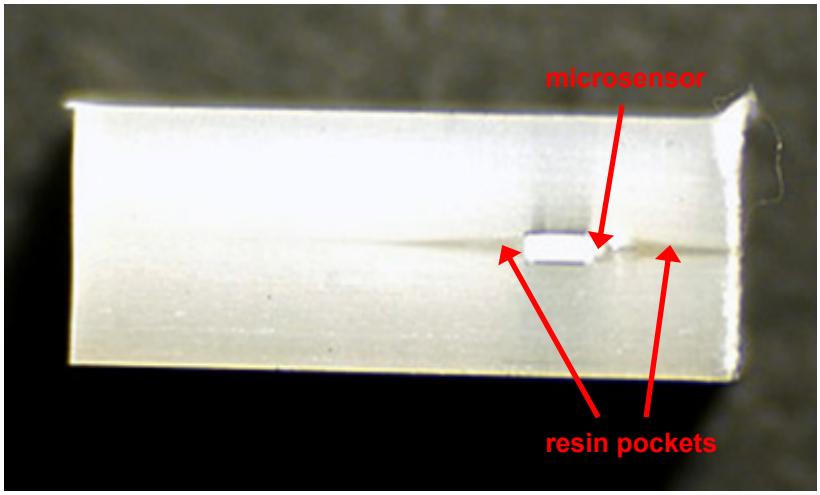

Figure 4.41: Resin pockets in three-point bending (short-beam shear) embedded sensor test specimen.

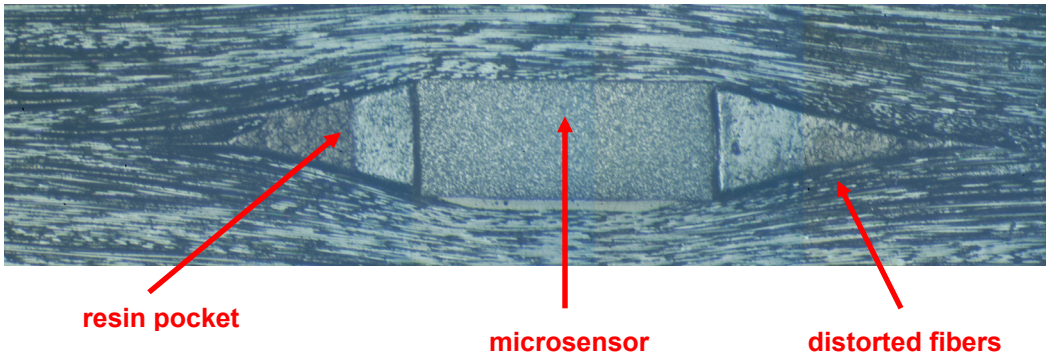

Figure 4.42: Resin pockets surrounding rectangular simulated microsensor.

The large eye shape resin pockets form due to the distortion of the neighboring fibers. This was the primary motivation behind creating precision punched cut-outs in the prepreg to accommodate the embedded sensor. Through the use of precision punched cut-outs, the fibers no longer are distorted as they maneuver themselves around the embedded sensor, instead, the fibers continue up until they reach the sensor

interface, thus eliminating the problematic fiber distortion and eye shape resin pocket. This is concisely exemplified in the micrographs shown below in Figures 4.43 a - e.

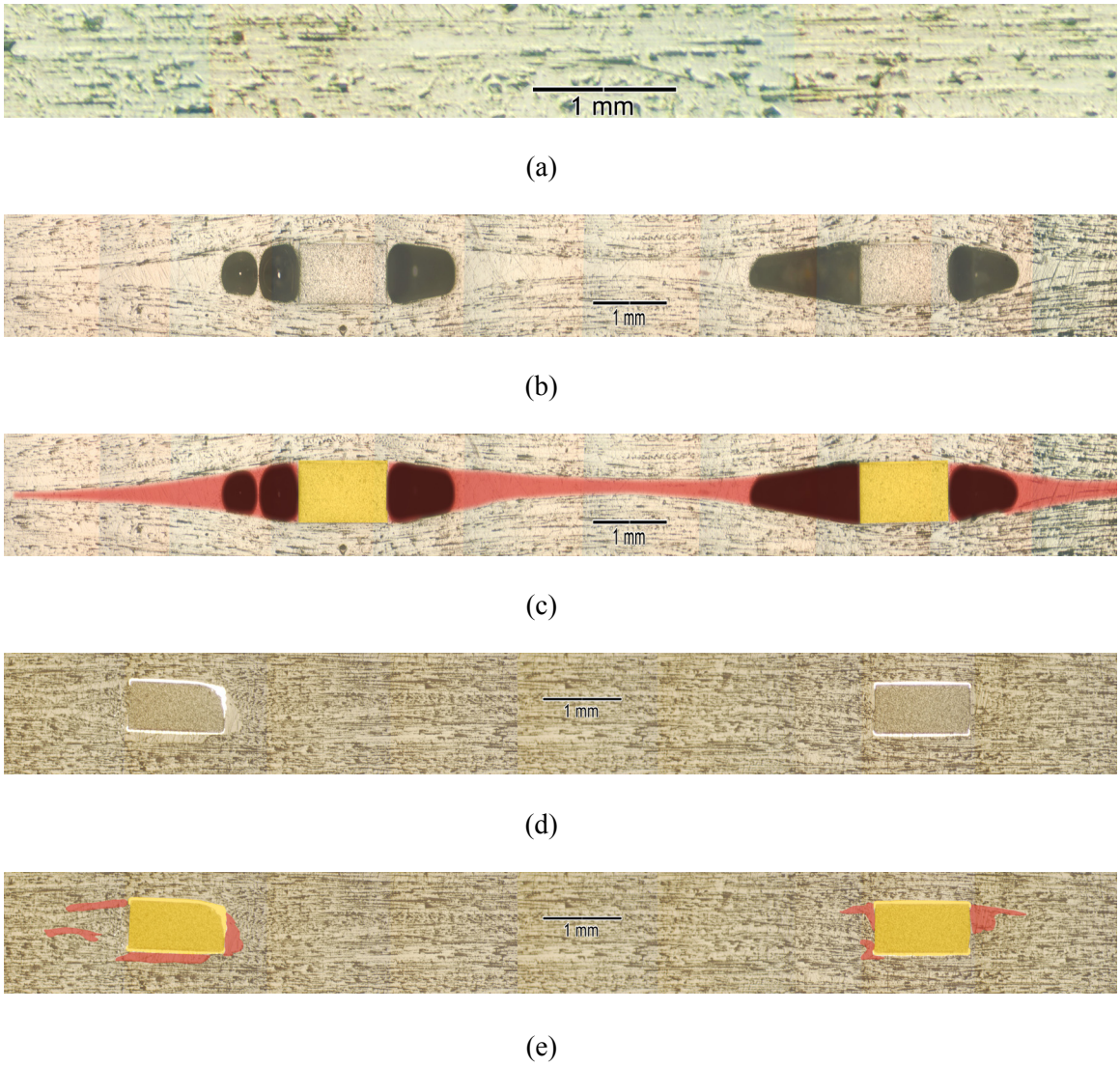

Figure 4.43: (a) Micrograph (125X) of blank specimen. (b) Micrograph (125X) of embedded sensor specimen. (c) Micrograph (125X) of embedded sensor specimen with resin pockets highlighted in red, voids highlighted in black, and sensors highlighted in gold. (d) Micrograph (125X) of punched sensor specimen. (e) Micrograph (125X) of punched sensor specimen with resin pockets highlighted in red, voids highlighted in black, and sensors highlighted in gold.

The initial introduction of the PVDF sensor in the form of the PVDF Ag-ink protective coating midplane specimens clearly demonstrated that there was a bonding issue between the screen printed acrylic protective coating and the epoxy of the host composite material. Once the protective coating was eliminated, the fatigue lives of the various PVDF configurations improved.

The PVDF sandwich configuration was briefly investigated, and though the configuration fared quite well, the study was still primarily interested in embedding at the midplane. The initial results from the PVDF (Ag-ink and NI-Cu) midplane specimens were lackluster. However, integrating an entire layer of PVDF at the midplane represents a worst case scenario. Once the PVDF was integrated using a more representative area of the material (12.7 mm by 6.35 mm), the fatigue lives increased dramatically.

Although the PVDF Ag-ink representative area midplane specimen achieved a higher average fatigue life as compared to the PVDF Ni-Cu representative area midplane specimen, the Ag-ink metallization had a tendency to migrate and short out circuits after being subjected to the composite processing procedure. Thus, the Ni-Cu metallization has been selected for use in the composite material in order to create an integrated embedded sensing network.

4.7 Summary

The results from the quasi-static three-point bending (short-beam shear) tests have been found to be highly repeatable for a given specimen geometry, material system, and stacking sequence. The tests produced very characteristic results. Furthermore, in the quasi-static loading regime, the tests indicated that the introduction of the simulated microsensors, G-10, and various PVDF sensors had a negligible effect on the average short beam shear strength, regardless of the configuration.

Fatigue three-point bending (short-beam shear) tests, which more accurately simulate real world or in-service loading conditions have been conducted. The results of the tests indicate that the type of embedment and the method in which the sensor is integrated into the host composite material have profound effects on the fatigue life.

The primary goal of this research is to ultimately extend the functionality of the composite material beyond that of simply load bearing by enabling *in situ* sensing without compromising the structural integrity of the host composite material. The PVDF Ni-Cu sensor has been selected for integration into the host glass/epoxy composite material based upon its test results.

It is important to note that the particular geometry of the short-beam shear test specimen is designed to lend itself to interlaminar shear failure upon three-point

bending loading. Thus, upon full-scale implementation even under three-point bending loading, this failure mode may not be the dominant failure mode.

Furthermore, for the three-point bending (short-beam shear) test specimens, all of the sensors that were embedded in the host composite material cover a rather large area relative to the overall size of the test specimen. Therefore, the results presented here again may not be indicative of those expected upon full-scale implementation.

4.8 Acknowledgement

I would like to thank Mr. Patrick Rye for assisting with the precision punching of the prepreg material. He was instrumental in coaxing uncooperative equipment apart and destroying as few precision bits as possible. I would also like to thank Mr. Patrick Rye for creating the computer program used to downsize the enormous data files so that they could be transferred from the computer running the TestStar program for proper analysis.

References

Adams, D. F. and E. Q. Lewis. 1994. Current Status of Composite Material Shear Test Methods. *SAMPE* **31** (6): 32-41.

Adams, D. F. and E. Q. Lewis. 1995. Experimental Study of Three and Four-Point Shear Test Specimen. *Journal of Composites Technology & Research* **17** (4): 341–349.

American Society for Testing and Materials. 2000. Standard Test Method for Short-Beam Strength of Polymer Matrix Composite Materials and Their Laminates. Designation D 2344/D 2344M–00.

American Society for Testing and Materials. 2000. Standard Test Method for Tensile Properties of Polymer Matrix Composite Materials. Designation D 3039/D 3039M–00.

American Society for Testing and Materials. 2001. Standard Test Method for In-Plane Shear Response of Polymer Matrix Composite Materials by Tensile Test of a ±45° Laminate. Designation D3518/D3518M-94.

American Society for Testing and Materials. 2002. Test Method for Ignition Loss of Cured Reinforced Resins. Designation D 2584-02.

Baker, A., S. Dutton, and D. Kelly. 2004. *Composite Materials for Aircraft Structures*. American Institute of Aeronautics and Astronautics, Inc., Reston, VA.

Chawla, K. K. 1987. *Composite Materials: Science and Engineering*. Springer-Verlag, New York.

Chen, A. S. and F. L. Matthews. 1994. Static and Cyclic Biaxial Bending of CFRP Panels. *Composites Science and Technology* **52**: 267-273.

Chow, W. T. and M. J. Graves. 1992. Stress analysis of a rectangular implant in laminated composites using 2-D and 3-D finite elements. *Proceedings of AIAA/AHS/ASME/ASCE/ASC 33rd Structures: Structural Dynamics and Materials Conference*, 848–861.

Crawley, E. F. and J. de Luis. 1987. Use of piezoelectric actuators as elements of intelligent structures. *Journal of AIAA* **25**: 1373–1385.

Daniel, I. M. 1993. Composite Materials. *Handbook on Experimental Mechanics: Second Edition*, ed. Albert S. Kobayashi. Society for Experimental Mechanics, Bethel, CT.

Gautschi, G. 2002. *Piezoelectric Sensorics*. Springer. New York.

Hansen, J. P. and A. J. Vizzini. 2000. Fatigue Response of a Host Structure with Interlaced Embedded Devices. *Journal of Intelligent Material Systems and Structures* **11**: 902–909.

Huang, Y., K. Loewke, K. Schaaf, and S. Nemat-Nasser. 2005. Localized SHM with Embedded Sensor Network. *Proceedings of the Fifth International Workshop on Structural Health Monitoring: Advancements and Challenges for Implementation*, 1554-1561.

Kaw, A. K. 2006. *Mechanics of Composite Materials*. Taylor and Francis Group, Boca Raton.

Kelly, A. 1986. *Strong Solids*, 3rd ed. Clarendon Press, Oxford.

Kim, K., M. Breslauer, and G.S. Springer. 1992. The Effect of Embedded Sensors on the Strength of Composite Laminates. *Journal of Reinforced Plastics and Composites* **11**: 949-958.

Lin, M. and F. Chang. 2002. The manufacture of composite structures with a built-in network of piezoceramics. *Composite Science and Technology* **62**: 919–939.

Mal, A. 2004. Structural health monitoring. *Mechanics* **33** (11–12): 6-16.

Mall, S. and J.M. Coleman. 1998. Monotonic and fatigue loading behavior of quasi-isotropic graphite/epoxy laminate embedded with piezoelectric sensor. *Smart Materials and Structures* **7**: 822–832.

Mallick, P. K. 1993. *Fiber-Reinforced Composites: Materials, Manufacturing, and Design*. Marcel Kekker, Inc., New York.

McFarland, Grant. 2006. *Microprocessor design: a practical guide from design planning to manufacturing*. McGraw-Hill, New York.

Measurement Specialities, Inc. 2006. *Piezo Film Sensors Technical Manual*. Hampton, VA.

National Transportation Safety Board. 2004. *In-Flight Separation of Vertical Stabilizer, American Airlines Flight 587, Airbus Industrie A300-605R, N14053, Belle Harbor, New York, November 12, 2001.* Aircraft Accident Report NTSB/AAR-04/04. Washington, DC.

Nemat-Nasser, S., S. C. Nemat-Nasser, T. A. Plaisted, A. Starr, and A. Vakil Amirkhizi. 2005. Multifunctional Materials in Y. Bar Cohen (ed.) *Biomimetics: Biologically Inspired Technologies*. CRC Press, Boca Raton, FL.

O'Brien, T. K., A. D. Chawan, R. Krueger, and I. L. Paris. 2002. Transverse tension fatigue life characterization through flexure testing of composite materials. *International Journal of Fatigue* **24**: 127-145.

Paepegem, W. V., K. De Geyter, P. Vanhooymissen, and J. Degrieck. 2004. Effect of friction on the hysteresis loops from three-point bending fatigue tests of fibre-reinforced composites. *Composite Structures* **72** (2): 212-217.

Paget, C. A. and K. Levin. 1999. Structural Integrity of Composites with Embedded Piezoelectric Ceramic Transducer. *Proceedings of SPIE Conference on Smart Structures and Integrated Systems* **3668**: 306–313.

Roudet, F., Y. Desplanques, and S. Degallaix. 2002. Fatigue of glass/epoxy composite in three-point-bending with predominant shearing. *International Journal of Fatigue* **24**: 327-337.

Rye, P., A. Starr, K. Schaaf, and S. Nemat-Nasser. 2005. Integration of Electronic Sensing in Composite Materials for Structural Health Monitoring. *Proceedings of the Fifth International Workshop on Structural Health Monitoring: Advancements and Challenges for Implementation*, 756–761.

Rye, P., K. Schaaf, A. Starr, and S. Nemat-Nasser. 2006. Self-Sensing Composites. *Proceedings of the 2006 SEM Annual Conf. & Expo. on Experimental & Applied Mechanics*.

Rye, P.M., Y. Huang, F. Ghezzo, K. Schaaf, and S. Nemat-Nasser. 2007. Distributed Sensing, Damage Detection, and Analysis in FRP Unidirectional Composites. *Proceedings of the 2007 SEM Annual Conf. & Expo. on Experimental & Applied Mechanics*.

Schaaf, K., B. Cook, F. Ghezzo, Y. Huang, P. Rye, J. Aller, K. Loewke, A. Starr, and S. Nemat-Nasser. 2005. Composite Materials with Integrated Embedded Sensor Networks. *Proceedings of the Second International Workshop on Advanced Smart Materials and Smart Structures Technology*, (ed.) C. Yun and B. F. Spencer. Techno Press, 79–88.

Schaaf, K., B. Cook, F. Ghezzo, A. Starr, and S. Nemat-Nasser. 2005. Mechanical Properties of Composite Materials with Integrated Embedded Sensor Networks. *Proceedings of Smart Structures/NDE Joint Conference: Sensors and Smart Structures Technologies for Civil, Mechanical and Aerospace Systems*, *SPIE's 12th Annual International Conference on Smart Structures and Materials* **5765**: 781–785.

Schaaf, K., P. Rye, F. Ghezzo, A. Starr, and S. Nemat-Nasser. 2006. Optimization of the mechanical properties of composite materials with integrated embedded sensor networks. *Proceedings of Smart Structures and Materials 2006: Sensors and Smart Structures Technologies for Civil, Mechanical, and Aerospace Systems, SPIE's 13th Annual International Conference on Smart Structures and Materials* **6174**: 617443–1–617443-5.

Schaaf, K., P. Rye and S. Nemat-Nasser. 2007. Optimization Studies of Self-sensing Composites. *Proceedings of Sensors and Smart Structures Technologies for Civil, Mechanical, and Aerospace Systems*, *SPIE's 14th Annual International Conference on Smart Structures and Materials* **6529**: 65292X1-65292X5.

Schaaf, K., P. Rye and S. Nemat-Nasser. 2007. Optimization of Sensor Introduction into Laminated Composites. *Proceedings of 2007 SEM Annual Conference and Exposition on Experimental and Applied Mechanics*.

Schwartz, M. M. 1984. *Composite Materials Handbook*. McGraw-Hill, New York.

Shindo, Y., R. Wang, and K. Horiguchi. 2001. Analytical and Experimental Studies of Short- Beam Interlaminar Shear Strength of G-10CR Glass-Cloth/Epoxy Laminates at Cryogenic Temperatures. *Journal of Engineering Materials and Technology* **123**: 112–118.

Shukla, D. R. and A. J. Vizzini. 1996. Interlacing for improved performance of laminates with embedded devices. *Smart Material and Structures* **5**: 225-229.

Sims, G. D. and D. G. Gladman. 1982. A framework for specifying the fatigue performance of glass fiber reinforced plastic. *NPL report DMA* **59**: 1-24.

Singh, D. A. and A. J. Vizzini. 1993. Structural integrity of composite laminates with interlaced piezoceramic actuators. *Proceedings of Smart Structures and Materials: SPIE's Conference on Smart Structures and Intelligent Systems*, ed. Nesbitt W. Hagood and Gareth J. Knowles, 473–484.

Sirkis, J. S., H. Singh, A. Dasgupta, and C. C. Chang. 1992. Experimental determination of damage and interaction strain fields near active and passive inclusions embedded in laminated composite materials. *Proceedings of ADPA/AIAA/ASMI/SPIE Active Materials and Adaptive Structures*, 536–566.

Varadan, V.K. and V.V. Varadan, 2000. Microsensors, microelectromechanical systems (MEMS), and electronics for smart structures and systems. *Smart Materials and Structures* **9**: 953–972.

Wallace, Bruce. 2008. Composites in demand for the aircraft industry. *Deseret News*. http://www.deseretnews.com/article/1,5143,695270738,00.html (accessed May 8, 2008).

Warkentin, J. and E. F. Crawley. 1991. Embedded electronics for intelligent structures. *Proceedings of AIAA/AHS/ASME/ASCE/ASC 32nd Structures, Structural Dynamics and Materials Conference*, 1322–1331.

Whitney, J. M. 1989. Experimental Characterization of Delamination Fracture. *Interlaminar Response of Composite Materials*, ed. N. J. Pagano. Elsevier, 161-182.

Zhou, G. and L. M. Sim. 2002. Damage detection and assessment in fibre-reinforced composite structures with embedded fibre optic sensors – review. *Smart Materials and Structures*. **11**: 925-939.